NUMERICAL AND EXPERIMENTAL STUDIES OF FLOWS IN OPEN-CHANNELS WITH GRAVEL AND VEGETATION ROUGHNESSES

ZENG CHENG

Ph.D.

The Hong Kong
Polytechnic University

2012

The Hong Kong Polytechnic University

Department of Civil and Structural Engineering

Numerical and Experimental Studies of Flows in Open-Channels with Gravel and Vegetation Roughnesses

ZENG Cheng

A thesis submitted in partial fulfillment

of the requirements for the

degree of Doctor of Philosophy

Dec 2011

Certificate of Originality

I hereby declare that this thesis is my own work and that, to the best of my knowledge and belief, it produces no material previously published or written, nor material that has been accepted for the award of any other degree or diploma, except where due acknowledgment has been made in the text.

(Signed)

(Name of student) ZENG Cheng

Abstract

Open-channels made up of simple geometry and free of obstructions are desirable for efficient water conveyance. Nowadays, large and flexible roughness elements, such as gravels and vegetation, are commonly deployed into artificial open-channels to stabilize the channel sectional shapes and to maintain the ecological balance there. Consequently, the hydrodynamic behaviour of flows in these channels will be significantly affected. The determination of the velocity and turbulence intensity profiles, as well as the hydraulic resistance, is of practical importance in the engineering design of these channels. This study aims to quantify the gravel and vegetation induced roughness effects on flows and mixings in open-channels using experimental and numerical methods. The whole study can be subdivided into the following four parts.

Firstly, a three-dimensional (3D) Reynolds Averaged Navier-Stokes (RANS) model with the Spalart-Allmaras (S-A) turbulence closure has been developed to simulate the fully developed open-channel flows with smooth surface and submerged vegetation canopy. By comparing to the well-documented laboratory measurements and direct numerical simulation (DNS) results, the S-A model was valid for simulating open-channel flows with low Reynolds number (Re_τ = 439) and higher Reynolds number (Re_τ = 2143) over smooth bed. Furthermore, as the turbulence kinetic energy (TKE) cannot be calculated explicitly in the S-A model, an empirical equation were proposed and used to estimate the TKE. The resulting profiles of mean velocity, shear stress and TKE agree well with the well-documented experimental

data. The drag force method (DFM) was used to simulate the resistance effect induced by submerged vegetation. This method is found to be able to faithfully reproduce the mean flow and turbulence structure in open-channel flows with rigid or flexible vegetation canopy.

Secondly, a Double Averaged Navier-Stokes equation (DANS) model has been developed for depth-limited open-channel flows over gravels. Within the gravels the flow is highly obstructed and the porosity is low, the use of the RANS equations may not be accurate enough. Three test cases are used to validate the model: (1) an open-channel flow over a densely packed gravel bed with small-scale uniform roughness (D/d_{50} ~ 13, d_{50} = median diameter of roughness elements, D = water depth); (2) open-channel flows over large-scale sparely distributed roughness elements (D/Δ = 2.3 and 8.7, Δ = roughness height) and (3) steep slope gravel-bed river flows with D/d_{50} = 7 ~ 25. Various methods of treatment of the gravel-induced resistance effect have been investigated. The results show that the wall function approach (WFA) is successful in simulating flows over small gravels but is not appropriate for large gravels since the vertical profile of the longitudinal velocity does not follow the logarithmic-linear relationship. The drag force method (DFM) performs better but the non-logarithmic velocity distribution generated by sparely distributed gravels cannot be simulated accurately. Noting that the turbulence length scale within the gravel layer is governed by the gravel size, the DANS model incorporating the DFM and a modified S-A turbulence closure is proposed. The turbulence length scale parameter in the S-A model is modified to address the change in the turbulence structure within the gravel layer. The computed velocity profiles agree well with the corresponding measured profiles in all cases. Particularly, the

model reproduces the S-shape velocity profile for sparsely distributed large size roughness elements. The DFM is robust and can be easily integrated into the existing numerical models.

Thirdly, laboratory measurements of the velocity profiles and flow resistances of open-channel flows over fixed gravel patches (GPs) under different bed slopes and flow rates were carried out. Two GPs with identical individual element size and different lengths (3.81m and 7.5m) were tested. The depth-limited uniform flow regime with relative submergence S_r (= D/k_s) ranging from 2.68 to 5.94 was produced by adjusting the tailgate weir. The velocity profiles were carefully measured by using both an ultra-sound velocity profiler (UVP) and an acoustic Doppler velocimeter (ADV). The two sets of profiles measured were found to be consistent and have high correlation. The conventional methods used to determine the zero-plane displacement and estimate the bed shear velocity were then reviewed and compared. The uncertainty of the shear velocities estimated with different methods appears to be greater for the case with shorter patch length than that with longer patch length. The measured double-averaged (DA) velocity profiles were found to fit well with the log law and defect law with a non-universal Karman constant κ. Under relatively small submergence, the κ-value decreases to 0.22 for the fitting the velocity profiles by the logarithmic flow resistance law. The values of the constant $\overline{Br}$ in the logarithmic law fall within the normal range between 3.25 and 6.25. The streamwise turbulence intensity distributions were found to agree well with the available experimental data in the intermediate region and wall region.

Finally, the hydrodynamics of flows over a finite length flexible vegetation patch

(VP) was investigated in the laboratory. Plastic strips were attached vertically onto the flume bed section (3.4 m long × 0.3 m wide) to simulate the flexible VP. Uniform real gravels were paved before and behind the VP to represent the natural river bed. The ADV technique is used for monitoring the 3D velocity above and within the VP at high-frequency sample rates The density effect of VP was analyzed by comparing the measured results for the high density (HD) patch (α = vegetative coefficient = 0.056 m^{-1}) and those for the low density (LD) patch (α = 0.028 m^{-1}). The VP, which retarded the flow within the canopy and accelerated the overlying flow, appeared to be swaying under different flow rates. As the elevation of occurrence of the maximum velocity gradient increases with the distance downstream from the leading edge, the position of the maximum shear stress rises with distance from the channel bottom to the time-averaged deflected height of the VP. Correspondingly, the turbulence structure changes from the boundary-layer type to the mixing-layer type and the peak TKE occurs at the top of the trailing edge, similar to those observed in the flows with rigid VP. However, comparing to the case with rigid VP, the high-level turbulence region within the adjustment region occurred at a farther downstream distance from the leading edge for the case with flexible VP, as the high frequency vibration of the strips dissipates part of the TKE. In the fully-developed region the increasing canopy density leads to the increasing degree of inflection in the mean velocity profile. The existence of the Kelvin-Helmholtz (K-H) vortices within the shear layer is confirmed by both the flow visualization and the quadrant analysis. The flow evolution within the VP was successfully replicated by a 3D RANS model incorporating the DFM and the S-A turbulence closure.

In summary, the present research contributes to the knowledge and understanding of

open-channel flows with gravel and vegetation roughnesses. It reveals the mean flow and turbulence structure in the fully developed flows with gravels or submerged flexible vegetation as well as the flow evolution across the finite vegetation patch. The findings are supported by both laboratory measurements and numerical modelling results, and can be useful for engineering applications.

Acknowledgments

First of all, I would like to express my sincere gratitude to my supervisor, Professor C.W. Li, for his helpful suggestions, valuable guidance and incredible patience during my research and thesis work. This thesis would never reach to this point without his enlightening discussions and brilliant advice.

Particular thanks are expressed to the other three examiners of my PhD defense, Prof. Onyx W. H. Wai, Prof. Chiu On NG and Prof. Bingliang LIN, for their critical and constructive comments.

I am also grateful to the Hong Kong Polytechnic University for giving me the opportunity to study here and for providing me with the financial support. Many thanks are owed to Mr. K.H. Leung, the technician of the Hydraulic Laboratory, for his assistance in preparing the experimental setup and valuable help throughout the experiments.

I would like to thank my wife, Dr. J. Zhou, for her constant love and support throughout my doctoral study. Words can never express how much it has meant to me.

Finally, I would like to pay special thanks to my parents for their encouragement and support from home during these years.

Table of Contents

List of Figures

List of Tables

List of Photos

List of Symbols

Alphabetical Symbols

A_p	=	solidity ratio;
Br	=	numerical constant in log-law;
b_s	=	characteristics width of roughness elements, m;
b_v	=	width of stem, m;
C	=	parameter of velocity distribution;
C_d	=	drag coefficient;
C_h	=	Chézy resistance coefficient;
c_n	=	resistance factor ($= n/k_s^{1/6}$);
c_r	=	parameter of MWD that control the linearly distribution in interfacial sublayer;
C_s	=	shielding factor;
D	=	water depth measured from the reference level h_0, m;
d	=	thickness of the interfacial sublayer, m;
d_{50}	=	median diameter (diameter of bed particles for which 50% are finer), m;
d_{84}	=	diameter of bed particles for which 84% are finer, m;
d_{90}	=	diameter of bed particles for which 90% are finer, m;
f	=	Darcy-Weisbach friction factor;
Fr	=	Froude number;
f_{rk}	=	drag force parameter reflecting the resistance effect of the bed

		particles in DFM (= $C_d C_s b_s N/(1-A_p)$), m^{-1};
g	=	gravitational acceleration, m/s^2;
h	=	water depth measured from the bottom, m;
h_0	=	reference level (the level where the mean velocity is zero), m;
h_1	=	displacement of the zero-velocity plane below the top of the roughness elements, m;
$\overline{h_d}$	=	averaged deflected height (for flexible stem experiments), m;
h_p	=	penetration depth, m;
h_v	=	undeflected canopy height (for rigid stem experiments), m;
I	=	streamwise turbulence intensity (= u_{rms}/u^*);
k	=	Kinetic energy of turbulent fluctuations per unit mass, m^2/s^2;
k_r	=	thickness of the roughness layer (for small-scale roughness condition), m;
k_s	=	equivalent (Nikuradse) sand roughness (roughness length sacle);
k_s^+	=	dimensionless roughness height (= $k_s \cdot u^*/\nu$);
L_x	=	plant space in streamwise direction, m;
L_y	=	plant space in spanwise direction, m;
L_v	=	length of VP, m;
N	=	number density of gravel bed, m^{-2};
n	=	Manning resistance coefficient;
Q	=	flow rate, l/s;
Q_i	=	Event associated with quadrant i (where i = 1 – 4);
Re	=	Reynolds number;
Re_τ	=	Reynolds number (= $D \cdot u^*/\nu$);

R_h	=	hydraulic radius, m;
R^2	=	square of correlation coefficient;
S_0	=	bed slope;
U	=	depth averaged velocity, m/s;
$\bar{U}$	=	cross-sectional averaged velocity, m/s;
U_c	=	maximum point velocity observed over a velocity profile, m/s;
u, v, w	=	instantaneous velocity components in x, y, z directions, m/s;
$\bar{u}, \bar{v}, \bar{w}$	=	time-averaged velocity components in x, y, z directions, m/s;
u', v', w'	=	fluctuating velocity components in x, y, z directions, m/s;
$\langle\bar{u}\rangle, \langle\bar{v}\rangle, \langle\bar{w}\rangle$	=	double-averaged (in time and spatial domains) velocity components in x, y, z directions, m/s;
$u_{rms}, v_{rms}, w_{rms}$	=	root-mean-squared velocity fluctuations in x, y, z directions;
u^*	=	bed-shear velocity, m/s;
u^*_c	=	bed-shear velocity computed using Clause's method, m/s;
u^*_e	=	bed-shear velocity computed using energy gradient method, m/s;
u^*_r	=	bed-shear velocity computed using Reynolds stress method, m/s;
$-\overline{u'w'}$	=	Reynolds shear stress per unit mass, m^2/s^2;
S_r	=	relative submergence (= D/k_s);
W	=	channel width, m;
x, y, z	=	rectangular Cartesian coordinates, m;
z'	=	vertical distance from the bottom, m.

Greek Symbols

α	=	plant density, m^{-1};
δ	=	distance from the reference level to the point where velocity reach the maximum value, m;
δ_e	=	penetration scale, m;
κ	=	Karman constant;
v_m	=	kinematic molecular viscosity, m^2/s;
v_t	=	kinematic eddy viscosity, m^2/s;
ρ	=	water density, kg/m^3;
ϕ	=	porosity.

Abbreviations

One-Dimensional	1D
Two-Dimensional	2D
Three-Dimensional	3D
ADV	acoustic Doppler velocimetry
CFD	computational fluid dynamics
CGSTAB	conjugate gradient squared stabilized
DA	double-averaged
DANS	double averaged Navier-Stokes
DFM	drag force method
DNS	direct numerical simulation
GP	gravel patch
HD	high density
K-H	Kelvin-Helmholtz

PC	personal computer
PDF	probability density function
PIV	particle-image velocimetry
PTV	particle tracking velocimetry
LES	large eddy simulation
LD	low density
LDA	laser Doppler anemometer
LP	long patch
RANS	Reynolds averaged Navier-Stokes
RSM	Reynolds stress model
S-A	Spalart-Allmaras
SNR	signal-to-noise ratio
SP	short patch
TKE	turbulence kinetic energy
UVP	ultrasonic velocity profiler
VP	vegetation patch
WFA	wall function approach

Chapter 1.

Introduction and Overview

1.1. Introduction

1.1.1. General Background

Open channels, which refer to the natural or manmade conveyance structures with open tops, are efficient to convey flows for industrial and drainage purposes. Natural open channels include all watercourses that exist naturally on Earth, such as brooks, streams, rivers and estuaries. Manmade open channels are exemplified by drainage ditches, irrigation canals, aqueducts, flood diversion channels, *etc*. The most important characteristic distinguishes open-channel flow from closed conduit flow is that open-channel flow has a free surface in contact with air. Due to the existence of free surface, the open-channel flow structures are more complex. Neglecting the surface tension, the relevant forces causing and resisting motion and the inertia must form a momentum balance such that the free surface is a streamline along which the pressure is constant and equal to the atmospheric pressure.

Another important characteristic of open-channel flow is the extreme variability in the bed roughness. Turbulent flows and the associated transport processes in open channels are strongly influenced by the roughness elements on the channel bed. For natural rivers, the composition of the bed roughness is very complex. The roughness elements

include sand, gravel, rock, aquatic vegetation, *etc*. The characteristics of the elements, such as the shape, density and heterogeneity, can vary from site to site significantly. In man-made open channels, gravels and boulders are often deployed onto the bottom to prevent erosion. Recently, there is also a trend to plant vegetation within man-made open channels to maintain the balance of the whole ecosystem.

An undesirable effect of theses roughness elements is that the flow capacities of these channels will be significantly reduced due to the increase in resistances. The engineering design of drainage ditches as well as the river restoration both requires the knowledge of the resistance induced by bed roughness elements on the water flows. Therefore, many researchers have investigated flow resistance or friction laws for flows over fixed rough beds and over complicated bed configurations. Another effect is that the presence of bed roughness (particularly the large roughness) in an open-channel flow can alter the channel morphology and consequently change the velocity distribution, turbulence structure and coherent motion of the flow. These changes, in turn, can strongly influence the sediment transportation, erosion processes as well as the livings of organisms. Therefore a better understanding of this effect will be greatly advantageous to the river restoration and drainage/irrigation design.

Although the hydrodynamics of rough-bed flows has been studied extensively for the last two decades, there are still many unsolved problems awaiting clarification. For instance, the roughness effect on mean flow and turbulence structure is unclear for open-channel flows with small relative submergence (ratio between mean water depth and roughness height, D/k_s). Secondly, there is still a great deal of uncertainty in the accuracy of the representation of various flow and turbulence boundary conditions at

the bottoms of natural rivers, particularly in the presence of bed forms, and large bed roughness elements. The generation of turbulence and friction by bed roughness requires further study in order to understand flows over natural surfaces. In addition, the numerical simulation of rough-bed flows also received considerable research attention. Several methods used to represent the roughness effect have emerged recently. However, the present state of knowledge indicates that the accuracy of quantifying the roughness effect in turbulent open-channel flows is insufficient as compared to that achieved in modelling turbulent flows over smooth beds.

1.1.2. Objectives

The aim of this thesis is to contribute to the knowledge and understanding of depth-limited open-channel flows over gravel patches (GPs) and submerged vegetation patches (VPs) and to quantify the gravel and vegetation induced roughness effects on mean flow and turbulence structure using experimental and numerical methods. The specific objectives are:

1. To develop a three-dimensional (3D) Reynolds-averaged Navier-Stokes (RANS) model with the Spalart-Allmaras (S-A) turbulence closure to simulate fully developed open-channel flows over smooth beds and submerged vegetation canopies.
2. To develop a double-averaged Navier-Stokes (DANS) model incorporating the drag force method (DFM) and a modified S-A turbulence model to simulate the gravel-bed open-channel flows.
3. To understand the hydrodynamics of depth-limited open-channel flow over GP through laboratory experiments.
4. To conduct laboratory experiments of depth-limited open-channel flow over

finite flexible VP, and to assess the applicability of the developed 3D RANS model in modelling the flow evolution across the leading edge of VP.

1.2. Overview of thesis

This thesis consists of 7 chapters. Apart from the first introduction chapter, the remaining 6 chapters are organized as follows:

- Chapter 2 reviews the studies on open-channel flows with gravel and vegetation roughnesses. The results obtained from laboratory experiments and numerical simulations reported in the literatures are separately introduced.
- Chapter 3 presents the development of a 3D RANS model and its applications in modelling the open-channel flows with smooth and rough surface.
- In Chapter 4, a DANS model with modified S-A model is developed to simulate the gravel-bed open-channel flows and predicts the non-logarithmic velocity distribution.
- Chapter 5 describes the experiments for depth-limited open-channel flows over GP and presents the results. A sensitivity analysis of the drag force parameter (f_{rk}) is also included based on the flume measurements.
- Chapter 6 describes the experiments for the depth-limited open-channel flows with finite flexible VP and presents the results. In addition, the 3D RANS model developed in Chapter 3 are also used to replicate the flume experiments.
- Chapter 7 finally gives the conclusions on the results of the experimental and numerical works. It also points out the unsolved problems and makes some

recommendations for future work to pursue.

Chapter 2.

Literature Review

2.1. Introduction

In this chapter, we review the relevant concepts as well as the previous works on open-channel flows with gravel and vegetation roughnesses. The literatures related to some specific topics will be quoted separately in the subsequent chapters.

2.2. Review on the basic theories

2.2.1. Gravel-bed flows

2.2.1.1. Representative roughness height

In natural gravel-bed rivers, the bed roughness elements are mixtures of sediment of different sizes. Thus the representative roughness height is very difficult to be accurately estimated. Based on the previous investigations, the equivalent or Nikuradse's grain roughness, k_s, is often taken as the representative roughness height. However, there is much uncertainty on how to define k_s. The k_s is commonly assumed to be equal to the median diameter (d_{50}) for practical engineering applications. This assumption works reasonably well in more well graded sand bed rivers, where the size d_{50} could be considered to be a good representative of the roughness elements. However, this issue is more complicated for a natural river in

which the grain size typically has a much wider distribution, and the roughness elements may consist of sands, gravels, or cobbles. In this situation, the d_{50} is often too small to quantify the roughness effects.

For more accurate representation of the non-uniform bed roughness effect, k_s is generally assumed directly proportional to a characteristic grain diameter as follow:

$$k_s = C_x d_{xx} \tag{2-1}$$

where C_x is a constant corresponding to a characteristic grain diameter d_{xx}, and xx denotes the percentage of roughness elements with diameter smaller than d_{xx}. Equation (2-1) is empirical and different values of C_x and d_{xx} have been proposed. The proposed roughness length scale k_s could even exceed the maximum particle size present on the bed (Kamphuis 1974; Bray 1980; Gessler 1990). Van Rijn (1982) summarized the available literature and suggested a range of values from $k_s = d_{90}$ to $k_s = 10d_{90}$. It is generally assumed for gravel-bed rivers k_s is equal to $6.8d_{50}$ or $3.5d_{84}$ (Hey 1979; Bray 1980). The large range of the reported values of k_s in field measurements is not surprising as the bed roughness scale not only depends on the grain roughness, but also on the size of the bed forms (the aggregation of sediment grains), the bed load (rolling or saltating near-bed sediment layer), the lateral velocity gradients and the varying conditions immediately upstream. Consequently, many researchers believe that k_s cannot be estimated by a single grain size (Bray 1982; Hey and Thorne 1986; Kirchner *et al.* 1990; Robert 1990; Carling *et al.* 1992). Nikora (1998) and Smart *et al*. (2002) argues that the roughness properties of gravel-bed rivers can be described by three characteristic linear scales and k_s is a function of statistical properties of the roughness elements in the longitudinal, transverse and

vertical direction.

2.2.1.2. Flow regimes classification

In the presence of surface roughness, the turbulence structure near the surface depends on the viscous length scale ν/u^* (ν_m = kinematic molecular viscosity, u^* = wall shear velocity), and the roughness length scale k_s. The ratio of the roughness to the viscous length scale yields a single non-dimensional quantity as follow:

$$k_s^+ = \frac{u^* \cdot k_s}{\nu} \tag{2-2}$$

Base on this non-dimensional parameter, the turbulent rough-bed channel flows can be classified into three regimes:

1. Hydraulically-smooth ($k_s^+ < 5$) – where the bed roughness elements are completely submerged within the viscous sublayer and barely disturb the flow.
2. Transitionally-rough ($5 < k_s^+ \leq 70$) – where the bed roughness elements are only partially submerged within the viscous layer and both roughness effects and viscous effects are significant.
3. Fully-rough ($k_s^+ > 70$) – where the bed roughness elements disrupt the viscous and buffer layers and the velocity distribution becomes independent of the molecular viscosity.

Another classification of rough-bed flows is based on the ratio of water depth D to the roughness length scale k_s (Nikora *et al.* 2001):

1. Flow over partially inundated rough bed: $D/k_s < 1$
2. Flow with small relative submergence: $1 \leq D/k_s < 2 \sim 5$

3. Flow with large relative submergence: $D/k_s >> 1$

In terms of flow behaviors, Nikora *et al*. (2001) also subdivides the rough-bed flow into four types based on the characteristics of velocity distribution. These four kinds of flows are listed as follows:

- Type Ⅰ, with a roughness layer, a well-developed logarithmic (log) layer and an outer layer.
- Type Ⅱ, with a roughness layer and an outer layer.
- Type Ⅲ, in which the roughness layer occupies the entire water depth.
- Type Ⅳ, in which the roughness elements protrude through the free surface.

It is difficult to relate the relative submergence ratio (D/k_s) to the above flow types due to the fact that the flow also depends on other geometrical characteristics of roughness elements. For example, flow Type Ⅰ may occur at small relative submergence with streamlined roughness elements which produce a thin roughness layer and still allow the fully development of the log layer.

2.2.1.3. Zero-plane displacement

For fully turbulent flows over smooth boundaries, the zero level of the velocity profile, $z' = 0$, should be set at the solid boundary. However, for gravel-bed flows most of the researchers (Kamphuis 1974; Bayazit 1976; Nikora *et al.* 2002) hold the view that the actual reference level h_0, called the "hypothetical bed" (i.e., the level where the mean velocity is zero), lies between $z' = 0$ and $z' = k_r$, where k_r is the thickness of the roughness layer (as shown in Figure 2.1). In laboratories it is easy to define h_0, while in the field it is easier to define h_1, the displacement of the

zero-velocity plane below the top of the roughness elements. Although the determination of h_1 has been addressed in a number of studies, its value is still uncertain in practical applications. For example, several researchers have experimentally found that the values for h_1 could varied between $0.2k_s$ (Kironoto and Graf 1994) and $0.3k_s$ (Rodriguez and Garcia 2008) for typical gravel beds.

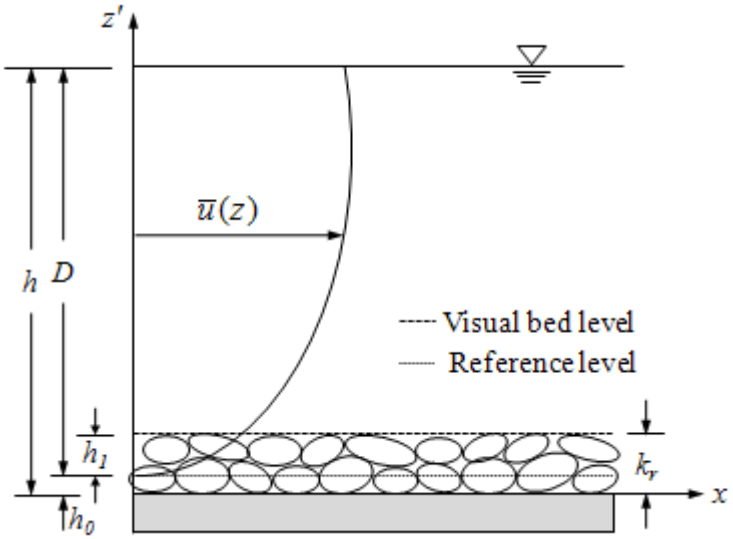

Figure 2.1. Typical velocity distribution in gravel-bed flows

The methods for determining h_0 from velocity measurements or roughness geometry have been developed for a long time. However, most of the theoretical and experimental developments were restricted to the atmospheric flows over rough surfaces such as buildings or forested areas (Monin and Yaglom 1971; Jackson 1981; Raupach *et al.* 1991). In aquatic environment this issue also has been also widely recognized among researchers dealing with rough-bed flows (e.g., Bayazit 1983). The existing methods have been well documented in Nikora *et al*. (2002). The most widely used method in hydraulics is the "Best-fit approach". According to the

method, the bed origin is defined as a level, which provides the best data fit for the near-bed logarithmic velocity distribution. This method can be further optimized by using the least square method and the correlation coefficient (or some other statistical measures) as a criterion. This method, although simple and appealing, can be only applied to the flows over small-scale roughness in which the logarithmic velocity distribution is valid in the inner region.

2.2.2. Submerged canopy flows

2.2.2.1. Flow regimes classification

It is well-known that the aquatic canopies can be classified as submerged or emergent depending on whether they occupy partly or fully the flow depth. Nepf and Vivoni (2000) further classified submerged canopy flows (as shown in Figure 2.2) into two types, depending on the depth ratio, defined by D/h_v, where D is the total flow depth and h_v is the canopy height. When $D/h_v > 5$ to 10, unconfined canopy flow occurs which is analogous to flow over a rough boundary. When $1 < D/h_v < 5$ to 10, the flow is classified as depth-limited canopy flow. The terrestrial canopy flow is all unconfined as the canopy height is small comparing to the atmospheric layer. The unconfined canopy regime is also observed in some deeply submerged flows, e.g. with seagrass meadows. However, for most aquatic vegetation flows the depth ratio is not large. Thus the submerged canopy flows in aquatic environment, generally speaking, is depth-limited.

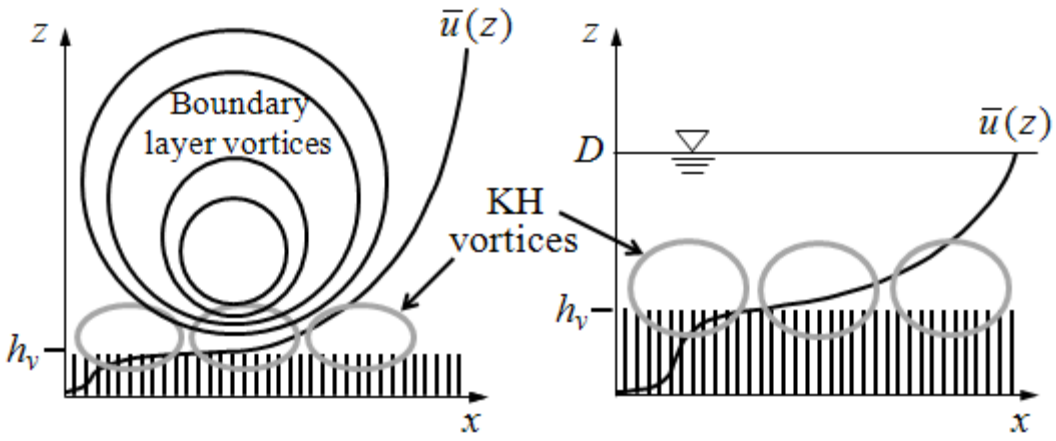

(a) Terrestrial canopy flow: unconfined

(b) Submerged aquatic canopy flow: depth-limited

Figure 2.2. Two flow regimes of submerged canopy flow (after Nepf and Ghisalberti 2008)

Much is already known about unconfined canopy flow through the studies on flows with terrestrial canopies, which is reviewed in Raupach *et al*. (1996). A key feature of the terrestrial canopy flow is the development of a strong shear layer at the top of the canopy with a flow structure similar to a free shear layer. Turbulence produced within this layer defines the scale of active turbulence within and just above the canopy. Typically, the shear length scale, L_s, is of the order of the canopy height. Turbulence produced within the wakes of vegetation stems become secondary, contributing approximately 10% of the in-canopy turbulence (Raupach and Shaw 1982). The flow within the canopy is driven only by the vertical turbulent transport of momentum from the overlying flow, with negligible contribution from pressure gradient (Raupach *et al.* 1991).

The detailed comparison between the terrestrial canopy flow and the aquatic canopy flow can be found in Nepf *et al*. (2007b). Different from the terrestrial canopy flow,

the flow in aquatic canopy flow is driven by the combination of turbulent stress generated by the overflow and by potential gradients associated with the hydrostatic pressure gradient and bed slope. The shear length scale L_s is also found to be dependent on the depth ratio in the aquatic environment. L_s is constant and of the order of the canopy height for $D/h_v > 2$, and is diminished for $D/h_v < 2$ (Nepf and Vivoni 2000). Nepf and Vivoni (2000) further inferred that wake turbulence is generally more important in aquatic than in terrestrial systems, even for large depths of submergence. Its contribution may never decline to the terrestrial limit of 10%.

The plant density can be described by the vegetative coefficient α (m^{-1}) which is defined as:

$$\alpha = \frac{projected\ area\ of\ \ plant}{total\ volume} = \frac{b_v}{s \cdot l} \tag{2-3}$$

where b_v is the width of the stem; s and l are the lengths of the control volume. Figure 2.3 shows the definition of these three parameters for circular section rod and rectangular rod. According to Nepf *et al*. (2007a), the parameter $C_d \alpha h_v$ indicates whether the canopy is dense ($C_d \alpha h_v > 0.1$) or sparse ($C_d \alpha h_v < 0.1$), where C_d is the drag coefficient and h_v is the canopy height.

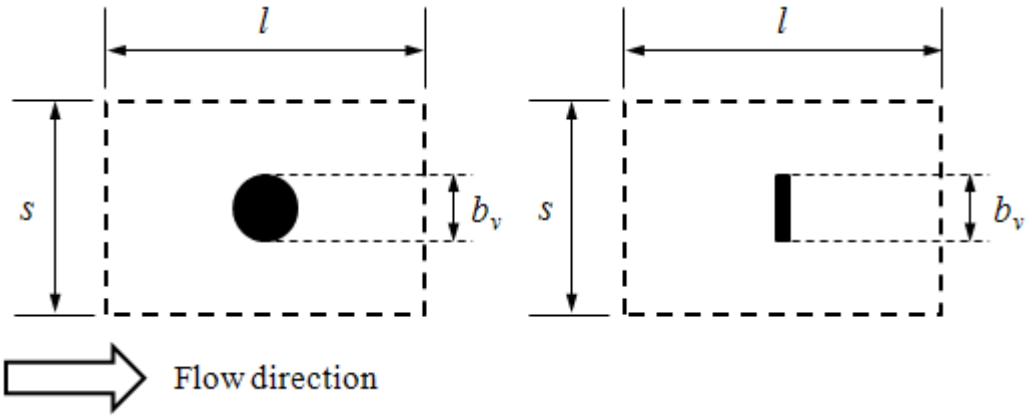

Figure 2.3. Definition of vegetative coefficient α

2.2.2.2. Flow structure within depth-limited canopy flows

Figure 2.4 shows the typical velocity profile within depth-limited canopy flows. In the presence of a submerged canopy, the whole flow region is divided into the following three sublayers:

1. Pressure-driven layer: ($0 \leq z \leq h_p$)
2. Mixing-layer: ($h_p \leq z \leq h_{log}$)
3. Logarithmic layer: ($h_{log} \leq z \leq D$)

Sufficiently far above the canopy, the velocity profile is logarithmic. However, the existence of this layer requires equilibrium turbulence, i.e., the dissipation and production are locally in balance (Nepf and Ghisalberti 2008). For very shallow submergence, $D/h_v \leq 1.5$, the logarithmic profile is not observed above the canopy (e.g., Nepf and Vivoni 2000). At the top of the canopy the discontinuity in drag generates a mixing-layer across the canopy-water interface. Within this layer, due to momentum absorption by the canopy elements, there exists an inflection point near the vegetation top which triggers the Kelvin-Helmholtz (K-H) instability. As a result, the coherent vortices developed at the canopy-water interface dominate the streamwise momentum and scalar transfer between overlying and canopy layers, making bottom friction much less important than the interfacial shear due to stem drag. Particularly within dense canopies, the vortices cannot penetrate completely to the bed. This, consequently, separates the canopy into two layers. The upper layer (termed as "Stress-driven layer") is predominantly driven by turbulent stress, which penetrates downward into the canopy over a distance δ_e (as shown in Figure 2.4). The lower layer (termed as "Pressure-driven layer") is driven by potential gradients due

to bed or pressure gradients. Nepf *et al*. (2007a) suggested that penetration scale δ_e is inversely proportional to the drag length scale of the canopy $((aC_d)^{-1}$ and can be given as:

$$\delta_e \approx 0.25(aC_d)^{-1} \tag{2-4}$$

The lower level of mixing-layer can also be determined by penetration depth h_p, at which the Reynolds stress $-\overline{u'w'}$ has decayed to 10% of its maximum value (Nepf and Vivoni 2000).

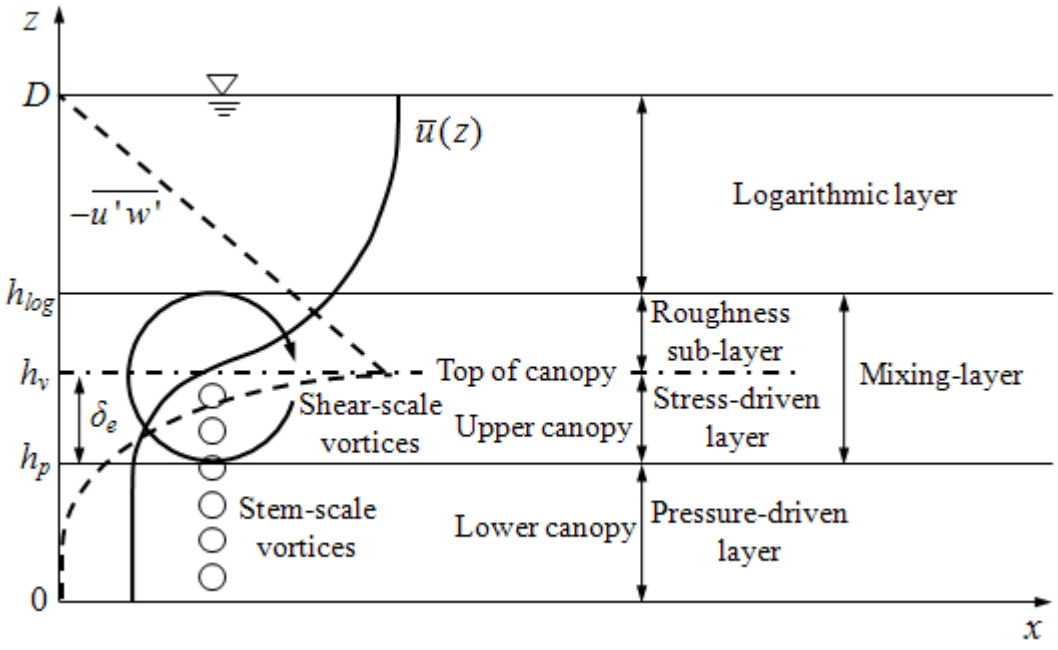

Figure 2.4. Velocity profile in and above a submerged canopy (after Nepf and Ghisalberti 2008)

Figure 2.4 also plots the typical distribution of the Reynolds stress ($-\overline{u'w'}$) within the depth-limited canopy flows. It can be seen from the figure that the peak value occurs at the canopy height and then decreases linearly above the canopy to a value

of zero at the water surface. Of particular significance is the sharp decrease in the Reynolds stress within the canopy, which is caused by the drag due to vegetation elements. In other words, the momentum transfer from the overlying layer toward the bed is obstructed by vegetation elements.

2.2.2.3. Coherent motion of flexible canopies

Most of the natural canopies are flexible and move in response to the mean and turbulent flows. Kouwen and Unny (1973) classified these motions into three types, i.e., (1) erect, (2) waving and (3) prone, and distinguished the erect and waving types (as rough boundary) from the prone type (as smooth boundary) by a critical friction velocity which is found to be a function of the vegetation density and the flexural rigidity. Later, Okamoto and Nezu (2009) considered the erect type and the waving type as the gently *Swaying* (deflected but no organized waving) and the *Monami* (organized waving) respectively.

Although the *Swaying* and *Monami* are both induced by the K-H vortices within the mixng-layer, these two type of motions lead to an evident difference in the flow structure of submerged canopy flows (Okamoto and Nezu 2009). The velocity gradient near the canopy height is larger for *Monami* than that for *Swaying* canopy, suggesting that the inflection-point instability and the associated organized motions occur more significantly for *Monami* than those for *Swaying* canopy. The Reynolds stress distribution has a rounder peak structure in *Monami* canopy flow than that in *Swaying* canopy flow. In addition, much higher space-time correlations among the vegetation elements are observed for *Monami* than those for *Swaying* canopy.

2.3. Review on experimental studies

The open-channel flows over gravel bed or submerged canopy have been extensively studied for a long time. There are numerous experimental and numerical studies reported. Some of the important works are reviewed hereinafter.

2.3.1. Experimental studies of gravel-bed flows

Kirkgoz (1989) carried out a number of experiments of flows over a uniformly rough surface with averaged roughness height varied from 1 to 12 mm, Froude number in a range from 0.075 to 0.43, and Reynolds number between about 20,000 and 100,000. Velocity profiles were collected by using a laser-doppler anemometer (LDA). He suggested that the shift of the zero reference level, which represents the fictitious viscous sublayer on a "rough" wall, decrease with increasing Reynolds number, but does not seem to be affected by the roughness height. The velocity profiles, without assuming a value for k_s different from the bed roughness height, were found to follow the following equation for $100 < zu^*/\nu < 400$:

$$\frac{\bar{u}}{u^*} = \frac{1}{\kappa}\left(\frac{z \cdot u^*}{\nu}\right) - 0.8 \qquad (2\text{-}5)$$

where κ is the Karman constant (= 0.41).

Ferro and Giordano (1991) performed an experimental investigation to study the effect of the concentration of coarse roughness elements on the friction factor. They found that the semilogarithmic equation gives the best fit to the experimental data and the use of d_{84} or d_{90} as the characteristic diameter implicitly includes the effect of

the particle concentration. The semilogarithmic resistance equation can be given as follows:

$$\frac{C_h}{\sqrt{g}} = b_0 + b_1 \log\left(\frac{D}{d_{xx}}\right) \tag{2-6}$$

where C_h = Chézy coefficient; g = acceleration due to gravity; b_0, b_1 = numeric constant. In the further study, Ferro (1999) suggested that b_0 depends on the median size ratio (ratio between the median diameter of coarser particles and the median diameter of the bed layer particles) and the boulder concentration. He explained the differences between the experimentally determined friction factor ($C_h/\sqrt{g}$) and the calculated values in terms of the ratio between the Shields parameter and its critical value.

Robert *et al.* (1992) provided the first experimental data set on the effects of roughness transitions on depth-limited flows. Flow measurements along roughness transitions from smooth to rough beds were collected in a flume using artificial roughness features as well as in a natural gravel bed river. Both sets of experiments (flume and field) show similar effects: flow deceleration at the bed downstream from the roughness transition, sharp increases of the velocity gradient and roughness length and increase in turbulence intensity.

Wang *et al*. (1993) conducted systematic measurements of longitudinal turbulence intensity in a laboratory gravel-bed flume with one-dimensional LDA. The bottom of the flume was roughened with gravels of uniform or non-uniform sizes. It was found that the distribution of streamwise turbulence intensity I (= u_{rms}/u^*) depends greatly

on the relative submergence D/k_s. For $D/k_s \leq 1.0$, I could be taken as a constant for the entire water depth. With the increase of D/k_s, the influence of the roughness elements on turbulence intensity decreases and the distribution of I gradually approaches that in the smooth bed case. The turbulence intensity distribution feature was also found to be independent on the uniformity of the bed roughness.

Ferro and Baiamonte (1994) carried out velocity measurements in a laboratory flume with a non-uniform gravel bed. The velocity profiles were collected for four different bed shapes, characterized from different concentrations of coarser elements, and for conditions of small- and large-scale roughness. It was found that the shape of velocity profile (S-shape or log-shape) was affected by the depth/sediment ratio D/d_{50}, the aspect ratio W/D, and the concentration of the gravel bed. They also compared the velocity profiles with the same Froude number and aspect ratio in order to identify the effect of the concentration. The comparison indicated that with small aspect ratio the number of coarser elements does not affect the velocity profile. For cases with high aspect ratio the velocity decreased when the concentration of coarser elements increased.

Kironoto and Graf (1994; 1995) experimentally investigated the turbulence structure of uniform and non-uniform open-channel flows over rough plate and gravel bed. For uniform flows, within the inner region, the velocity distribution follows the logarithmic law:

$$\frac{\bar{u}}{u*} = \frac{1}{\kappa} \ln\left(\frac{z}{k_s}\right) + Br \tag{2-7}$$

where Br is a numerical constant of integration with the suggested value of 8.47 ±

0.9 (Kironoto and Graf 1994) for uniform flow with densely packed, small-scale gravel bed.

In the outer region, the velocity distribution follows the Coles law:

$$\frac{U_c - \bar{u}}{u*} = -\frac{1}{\kappa}\ln\left(\frac{z}{\delta}\right) + \frac{2\Pi}{\kappa}\cos^2\left(\frac{\pi z}{2\delta}\right) \tag{2-8}$$

where U_c is the maximum point velocity in the mean velocity profile, and δ is defined as the distance between the reference level and the point where $\bar{u} = U_c$; Π is Cole's wake parameter and found to be equal to 0.09 based on the flume observations. The energy spectra display well the inertial sub-range characteristics. For non-uniform flows, the logarithmic law is also valid in the inner region. In the outer region, the measurements follow the Cole's law of the wake, for which the Π-value depends on the pressure-gradient parameter. The energy spectra for non-uniform flow are essentially the same as for uniform flow.

Dittrich and Koll (1997) also used one-dimensional LDA to measure the streamwise velocity components in gravel-bed flows. They reported that, for flows with low relative submergence, the value of the von Karman constant for the "best-fit" velocity profile following the logarithmic distribution is 0.18, departing significantly from the normal value (κ = 0.41). They argued that the reduction in the value of κ indicated some uncertainties in the applicability of logarithmic law to flows with large relative roughness.

Mignot *et al*. (2008) performed an experimental investigation focused on the characteristics of near bed turbulence in a fully rough, uniform open-channel flow

with a gravel bed. The flow characteristics are measured using a 3D-ADVP (Acoustic Doppler Velocity Profiler). From the experimental data analysis it appears that the double-averaged turbulence production, turbulence transport, and dissipation terms have their maximum values away from the reference plane, and occurred near the roughness crests.

Hardy *et al*. (2009; 2010) carried out flume experiments in which flows over gravel beds are quantified through the application of digital particle imaging velocimetry (PIV), which allows the study of the downstream and vertical components of velocity over the entire flow field. Their measuring results indicated that coherent flow structures over gravels owe their origin to bed-generated turbulence and that large-scale outer layer structures are the results of flow-topography interactions in the near-bed region associated with wake flapping. Particularly, as the effective protrusion decreases, the scale of these coherent flow structures also decreases.

2.3.2. Experimental studies of submerged canopy flows

Ikeda and Kanazawa (1996) captured the instantaneous two-dimensional (2D) and three-dimensional (3D) flow fields by using a 2D LDA and PIV. The measurements reveal that organized vortices are generated intermittently above the canopy. The side view of the vortex shows an elliptical shape, and the part of the 3D structure above the canopy consists of a pair of vortices inclined downward toward the front. The wavy motion of flexible vegetation is induced by the movement of such organized vortices. The average period of vortex generation can be explained in terms of linear stability analysis.

Wu *et al*. (1999) experimentally investigated the variation of the vegetative roughness coefficient with the water depth. Rubberized horsehair mattress material was used to simulate the vegetative roughness on the watercourses. Test results reveal that the roughness coefficient tends to increase at low depths but then decrease to an asymptotic constant as the water depth rises for fully submerged conditions. They developed a simplified model based on force equilibrium to evaluate the drag coefficient of vegetation.

Nepf and Vivoni (2000) conducted turbulence measurements in submerged vegetated open-channel flows using both LDA and acoustic Doppler velocimetry (ADV). They highlighted the effect of water depth on turbulence structure, and pointed out that the generation of wake turbulence due to vegetation stems is strongly associated with the depth of submergence (D/h_v). They firstly subdivided the flow field of the aquatic canopy flows into two regions, namely vertical exchange zone and longitudinal exchange zone.

Carollo *et al*. (2002) performed flume experiments to investigate the effect of vegetation concentration and the depth/vegetation height ratio on the velocity profiles of flexible canopy flows. They found that the location of the logarithmic zone is influenced by the depth/vegetation height ratio, but no relevant influence of the stem concentration was observed. However, the stem concentration affects the shape of the velocity profile. With decreasing stem concentration, the flow velocities inside the vegetation increase and the velocities above the canopy decrease. They also deduced a theoretical velocity profile using the classical Prantl's mixing length

turbulence model with a new expression for the mixing length.

Stephan and Gutknecht (2002) investigated three species of flexible aquatic vegetation under submerged conditions in a laboratory flume. Velocity measurements above the submerged canopy were conducted to determine the relationship between the hydraulic roughness and the deflected plant height. The deflected canopy height was used as the geometric roughness parameter, whereas the equivalent sand roughness based on the universal logarithmic law modified by Nikuradse was used as hydraulic roughness parameter. The absolute values of the equivalent roughness, the deflected plant height, and the zero plane displacement of the logarithmic law were all close.

Jarvela (2002) carried out laboratory investigations on flow resistance of natural grasses, sedges and willows. He reported that the Darcy-Weisbach friction factor f was dependent mostly on (1) the relative roughness in the case of grasses; (2) the flow velocity in the case of willows and sedges/grasses combined; and (3) the flow depth in the case of leafless willow on bare bottom soil. The friction factor of the case with leaves on willows could double or even triple the friction factor of the case without leaves. For the leafless willows, f appeared to increase with depth almost linearly and independent of velocity.

Wilson *et al*. (2003) conducted an experimental study to explore the effect of two forms of flexible vegetation on the turbulence structure within the canopy layer and the overlying water layer. They observed that the additional surface area of the fronds significantly increases the momentum absorbing area of the plant which leads to a

decrease in the mean primary velocities within the canopy layer and for a proportion of the overlying layer. Accordingly, the shear-generated turbulence is reduced due to the inhibition of momentum exchange by the frond surface area. The addition of the plant foliage at the top of the stems inhibits the turbulent mixing between the canopy layer and the overlying layer, and shifts the Reynolds stress peak to a level above the canopy height.

Poggi *et al*. (2004b) performed turbulence measurements in submerged canopy flows with rigid vegetation elements (cylinder rods) by using LDA. They developed a phenomenological model, in which the whole flow-depth region was divided into three layers. The first is the lower layer in which the Karman-vortex-street is generated due to vegetation stems; the second is the middle layer in which the K-H waves are generated by the inflection instability and the third is the upper layer which is similar to the boundary layer. By assuming different profiles of the mixing length in these three layers, the analytical velocity profiles can be computed and are in good agreement with the experimental results.

Ghisalberti and Nepf (2006) carried out flume measurements with rigid and flexible model vegetation to study the structure of coherent vortices and vertical transport in shallow vegetated shear flows. They found that the oscillation of moving vegetations, so-called "*Monami*", has significant effects on the large-scale coherent structure, i.e., sweeps and ejections, and pointed out that the momentum transfer within both rigid and flexible canopies is dominated by sweeps.

Okamoto and Nezu (2009) conducted simultaneous measurements of turbulence and

vegetation motion by using a combination of PIV and particle tracking velocimetry (PTV) in open-channel flows with flexible vegetation. They observed a periodical property of sweep and ejection motions near the vegetation canopies. These coherent motions govern the momentum transfer significantly for *Monami* canopy. The spectral analysis also revealed that the *Momani* frequency of vegetation is in good agreement with the peak frequency of the velocity spectrum for the *Monami* canopy.

Yang and Choi (2009) performed flume experiments on depth-limited open-channel flow with submerged vegetation. The main purpose was to investigate the impact of stem flexibility on the mean flow and turbulence structures. The instantaneous components of the streamwise and vertical velocities were measured by using 2D LDA. It was found that the stem flexibility hardly affects the mean flow but increases the peak value of the Reynolds stress. In addition, the stem flexibility respectively decreases and increases the streamwise component of the turbulence intensity within the canopy layer and the overlying layer.

2.4. Review on numerical studies

2.4.1. Numerical studies of gravel-bed flows

Computational fluid dynamics (CFD) or 3D numerical models have been widely used to simulate open-channel flows with simple geometries. The results also have been confirmed to be reliable by comparing to the data obtained under controlled laboratory conditions. However, the application of CFD models to natural rivers has not been so successful due to the complex geometry and topography. Generally speaking, there are

two traditional approaches to deal with the roughness elements. In the first approach a very fine grid is used to resolve the boundary of roughness elements. The disadvantage of this method is that the number of grid cells can be excessive for practical application. In the second approach the wall function is used to determine the hydraulic quantities in the boundary-adjacent cells, e.g., Nicholas and Smith (1999) and Wu (2004). This approach has been proven to be an accurate and economic method for dealing with flows over small-scale roughness elements as the roughness effect can be modeled within each grid cell. However, because this method requires the velocity distribution to be logarithmic in the near-bed region, it is not capable to accurately predict the S-shape velocity profiles resulting from flows over large-scale roughness elements. To settle the problem of complex irregular boundary geometry, several methods emerge recently. Olsen and Stokseth (1995) suggested a porosity treatment to model the large-scale roughness effect. This method allows smooth interactions between areas with small and large-scale roughness. The porosity of each cell is determined by empirical formulas for water flows through sand. Lane *et al*. (2004) combined this porosity treatment with a high-resolution digital elevation method and validated the numerical model for the case of flows over rough gravel beds. Nicholas (2001) proposed a random bed elevation model coupled with the wall function to simulate the supra-grid and sub-grid scale roughness components respectively. This model is capable to simulate the displacement of peak turbulent kinetic energy values above the bed resulting from the velocity shear. However, the random elevation model is mesh-dependent and the results obtained are sensitive to the horizontal and vertical mesh resolution.

The resisting effects of natural bed roughness can also be simulated by CFD models

utilizing the drag force method (DFM). In this method the gravel-induced resistance is represented by a drag force term which depends on the roughness geometry (size, shape, distribution, *etc*.) and the flow velocity. Although this method has been commonly used to simulate flows over vegetation canopies (e.g., Fischer-Antze *et al.* 2001; Lopez and Garcia 2001; Su and Li 2002), its application in gravel-bed open-channel flows has not been widely reported. Cui *et al*. (2003b) described a force field model to simulate turbulence flow over a surface with arbitrary roughness elements. The roughness was decomposed into resolved and subgrid-scale components by a fine Cartesian grid system. The force field used to represent the resolved roughness component was determined through the Large Eddy Simulation (LES) solution process without empiricism. The subgrid-scale roughness was modeled by a random drag force distribution in which a drag coefficient was required to be specified. The model was successfully applied in the calculations of a duct flow over wavy wall with superimposed fine-grain roughness. Wiberg and Smith (1991) developed a modified mixing-length model to simulate spatially averaged velocity profiles for flows over poorly sorted beds. The drag forces associated with different grain sizes were computed and aggregated as a sink term in the momentum equations. The computed velocity profiles agreed with those obtained from field measurements in coarse gravel-bedded rivers by Marchand *et al*. (1984). Carney *et al*. (2006) used FLUENT with the RNG (Re-Normalization Group) k-ε turbulence closure and treated the bed roughness layer as a porous medium. A constant drag coefficient was used and the results compared favorably with the field data. Nicholas (2005) developed a drag force model in which the drag coefficients are based on bed topography profiles to represent the bed roughness. The methodology appears to be sensitive to both the hydraulic conditions and grid resolution.

2.4.2. Numerical studies of submerged canopy flows

Numerical modelling of submerged canopy flows has received much attention in the last few decades, especially for cases in the atmospheric environment. For atmospheric canopy flows, advances in modelling technology are well reviewed in Finnigan (2000) and Finnigan *et al* (2009). Thus only the numerical studies of aquatic canopy flows are reviewed hereinafter.

Many RANS methods for simulating the fully developed submerged canopy flows have been reported. Shimizu and Tsujimoto (1994) developed a modified k-ε turbulence closure model, introducing drag-related sink terms into the momentum as well as into the k- (turbulent kinetic energy) and ε- (dissipation) transport equations. They adjusted the drag coefficient C_d between 1.0 and 1.5 to achieve a good fit with between the computed results and the measured velocity and Reynolds stress profiles by Tsujimoto *et al*. (1992). As C_d was not specified a priori their model can be considered incomplete. Lopez and Garcia (1997) numerically replicated the physical experiments (Dunn *et al.* 1996) and calibrated the drag induced parameters of the k-ε model. As their model is complete with a constant C_d (= 1.13), the reported calibrated results were less accurate comparing to those of Shimizu *et al* (1944). The adoption of universal values for the weighting coefficients (C_{fk} = 1.0 and $C_{f\varepsilon}$ = 1.33) may lead to the overestimation of the streamwise turbulence intensity. More recently, Lopez and Garcia (2001) tested the accuracies of two turbulence closure schemes (k-ε and the k-ω) by computing the mean flow and turbulence structure of submerged canopy flows. No significant difference in numerical performance was found between these two models. They further claimed that the inconsistencies in the values of the

weighting coefficient are due to the spatial and temporal averaging technique used within the simulation to account for the heterogeneous nature of the velocity and turbulence intensity fields. To avoid the recalibration of the turbulence model, Fischer-Antze *et al*. (2001) developed a similar drag force method but only introduced sink terms into the momentum equations and made no modification to the *k*-ε model. The turbulence closure adopted the standard values for the weighting coefficients and the value of C_d equal to unity. The model was implemented to reproduce flows through rigid and emergent vegetation in simple-section and compound-section channel arrangements and good agreement between the computed results and the experimental data was reported. Neary (2003) developed a numerical model which using a near-wall *k*-ω turbulence closure for 1D fully developed canopy flows. Based on extensive validation, he found that reasonable predictions of streamwise velocity and Reynolds stress profiles could be obtained by using universal values for all coefficients, but the calculated energy gradients were inaccurate. The amendatory values for C_{fk} and $C_{f\omega}$ were suggested to improve the predictions of streamwise turbulence intensity. Li and Zeng (2009) applied a 3D model utilizing the DFM and the one-equation S-A turbulence closure to simulate vegetated flows in channel junctions. The model was complete with constant drag coefficient (C_d = 1.13). The model successfully replicated the experimental cases of Dunn *et al*. (1996).

With the rapid development of computing hardware, high order anisotropic model (i.e., Reynolds stress model) was introduced to simulate the submerged canopy flows. To the author's knowledge, Naot *et al*. (1996a; 1996b) were the first to use the Reynolds stress model (RSM) to simulate the flow through rigid submerged

vegetation elements. They also used the DFM but additionally accounted for the effect of sheltering, i.e., the upstream rods obstructing the flow and reducing the drag force on the downstream rods. Furthermore, they related two vegetative weighting coefficients to a characteristic length scale that can be estimated from the configuration and geometry of the vegetative elements. Choi and Kang (2006) developed an RSM for the numerical simulation of a partly-vegetated flow. Comparisons between the computed results and the experimental data indicated that the RSM predicts turbulence structures such as turbulence intensity and Reynolds stress components reasonably well. Particularly, the evaluation of secondary current patterns and mean flow structure were obtained with the RSM.

Recently, the use of large eddy simulation (LES) and even hybrid LES/RANS modelling to simulate the submerged canopy flows has been emerged. Su and Li (2002) proposed an LES model and considered the vegetation as an internal source of resistant force and turbulence energy. The satisfactory agreement between the numerical results and the experimental data was reported. At the interface between the vegetated and non-vegetated regions, they successfully replicated the organized vortex which grows in size and then transported downstream. Li and Yu (2010) developed a hybrid LES/RANS model for effective simulation of vegetated open-channel flow. The model employed the S-A turbulence closure in the RANS region and the Smagorinsky sub-grid scale turbulence closure in the LES region. They investigated various boundary treatments to efficiently couple the RANS and LES model. With proper boundary treatments, the hybrid model is found to perform better in predicting the turbulence quantities (e.g., turbulence intensity and Reynolds stress) than the RANS model.

2.5. Summary

In the previous section of this chapter, the basic concepts and theories for the open-channel flows with gravel bed and submerged canopy have been reviewed. Some of the widely used methods and formulas were summarized. The existing experimental and numerical studies were also briefly reviewed.

For the numerical studies, in spite of extensive research efforts, the change of the turbulence length scale within the interfacial sublayer is still unknown. In addition, the existing literature indicates that the Double Averaged Navier-Stokes (DANS) approach is still a challenge to modeler. Therefore, in the present study, it is necessary to deepen the understanding on these two issues.

For the experimental studies, although numerous laboratory and field measurements have been reported, the double averaged (DA) experiments data is still limited. And the gravel-bed open-channel flow with small submergence also needs to be further investigated.

Chapter 3.

RANS Modelling of Open-Channel Flows

3.1. Introduction

With the rapid development of modern computational techniques and numerical solution methodologies over the last few decades, CFD has emerged to be an alternative to physical modelling in hydraulic engineering, with its advantages of lower cost and greater flexibility. CFD models that solve the Navier-Stokes (N-S) equations can provide us not only the high-resolution data of the flow field, but also the guidelines for engineering projects such as flood control, channel design, erosion control and channel restorations. Although the 3D CFD models have been widely used in hydraulic engineering simulation, the prediction of turbulent flows is still a continuing challenge. Three methods are available for this problem: direct numerical simulation (DNS), large-eddy simulation (LES), and the solution of the Reynolds-averaged Navier-Stokes (RANS) equations with turbulence models. DNS and LES can provide invaluable information about the details of the flow field, and are expected to be more accurate than RANS solutions in 3D, nonequilibrium flows. However, to take the advantages provided by DNS or LES one needs access to high-performance computing facilities as well as highly resolved initial and boundary conditions, which are currently unavailable for many real-life engineering

or ecological applications. Thus, the RANS-based numerical modelling has become the most popular tool in solving practical problems of fluvial hydraulics.

Applications involving the simple channel geometries (e.g., backward-facing steps, ducts, confluences and compound channels) have been verified rigorously with measurements collected under controlled laboratory conditions. Most of these simulations were concerned with the smooth bed (e.g. Pezzinga 1994; Williams and Baker 1997). Some of them were conducted with regular bed forms, such as fixed dunes (Dimas *et al.* 2008) and ribs (Cui *et al.* 2003a). Recently, several researchers have demonstrated the utility of using CFD in open-channels with natural roughness, such as gravels and vegetation (e.g. Nicholas 2005; Carney *et al.* 2006; Wilson *et al.* 2006). The roughness models function at several levels, including equivalent (Nikuradse) sand roughness, mixing-length modification, wall-function approach, and changes to wall boundary condition. These approaches, which were reviewed by Patel (1998), have been used in RANS models with some success. In the present simulations, we focus on the drag force method (DFM) in which an extra term, the drag force, is introduced into the momentum equations to represent the resistance effect of bed roughness.

In this chapter, a 3D RANS model with Spalart-Allmaras (S-A) turbulence closure is utilized and tested against laboratory experiments of fully developed turbulent flows with smooth bed and submerged vegetation. This model was initially developed by Lin and Li (2002) and further extended by Li and Yan (2007), Li and Zeng (2009). This chapter is organized as follows: the governing equations, turbulence model and numerical methods adopted are firstly introduced. The numerical model is

subsequently tested with two well-documented laboratory experiments, namely, open-channel flows with smooth bed and submerged vegetation. As the turbulence kinetic energy (TKE) cannot be calculated explicitly in the S-A model, an empirical equation was proposed, tested and used to estimate the TKE in smooth-surface open-channel flows.

3.2. Numerical methodology

3.2.1. Reynolds averaging

Turbulent flow is the commonest type of flow in open channels. It consists of motions with a wide spectrum of length scales ranging from millimeters to the flow depth. Moreover, the random and short-term fluctuations of flow properties (e.g., velocity and density) govern the energy dissipation rate, the transport of matter and the processes of dispersion or mixing. The most common way of describing turbulence is the statistical approach which was introduced by Reynolds (1895). In the approach, the instantaneous turbulent flow velocities can be decomposed into mean and fluctuating parts. The averaged value of a variable is the mean and the fluctuating part is an unknown. There are several methods of taking the average: (1) time average which would suit for a turbulent flow which is steady in time or is of a low degree of unsteadiness in time; (2) spatial average where the flow is uniform in all directions and the turbulence is homogeneous and (3) ensemble average which is the most commonly used as it suits for all flows that are unsteady.

In the present study, based on the first method of Reynolds decomposition, the

instantaneous velocity u_i and the kinematic pressure p can be decomposed into time-averaged mean and fluctuating parts as follows:

$$u_i = \overline{u}_i + u_i', \quad p = \overline{p} + p' \tag{3-1}$$

where the overbar denotes the time-averaged mean and the prime denotes the fluctuating part. The mean of a mean is equivalent to itself while the mean of a fluctuation is zero.

3.2.2. Governing equations and turbulence closure

The fundamental parameters required to describe an open-channel flow are the pressure and the velocity of the flow. If the fluid is water the flow can be assumed to be Newtonian and incompressible, these two parameters are solely governed by the constitutional Navier-Stokes equations which are based on the basic physical principles of conservation of mass and momentum. The Navier-Stokes equations for Newtonian and incompressible fluids can be formulated as follows:

Continuity equation:

$$\frac{\partial u_i}{\partial x_i} = 0 \quad (i=1,2,3) \tag{3-2}$$

Momentum equations:

$$\frac{\partial u_i}{\partial t} + u_j \frac{\partial u_i}{\partial x_j} = \nu_m \frac{\partial^2 u_i}{\partial x_j \partial x_j} - \frac{1}{\rho}\frac{\partial p}{\partial x_i} + g_i \quad (i=1,2,3) \tag{3-3}$$

where x_i (= x, y, z) are the coordinates in longitudinal, transverse and vertical directions, respectively; u_i (= u, v, w) are the instantaneous velocity components in x, y and z directions, respectively; t = time; ρ = density of fluid; p = dynamic pressure; ν_m = kinematic molecular viscosity; g_i (= g_x, g_y, g_z) are the components of the gravitational acceleration.

The Reynolds-averaged form of the N-S equations for an incompressible and turbulent open-channel flow can be obtained by introducing the Reynolds decomposition (Equation 3-1) and averaging Equations 3-2 and 3-3. They can be written as follows:

Continuity equation:

$$\frac{\partial \overline{u}_i}{\partial x_i} = 0 \quad (i = 1,2,3) \tag{3-4}$$

Momentum equations:

$$\frac{\partial \overline{u}_i}{\partial t} + u_j \frac{\partial \overline{u}_i}{\partial x_j} = \frac{\partial}{\partial x_j}\left[\nu_m \left(\frac{\partial \overline{u}_i}{\partial x_j} + \frac{\partial \overline{u}_j}{\partial x_i} \right) - \overline{u_i' u_j'} \right] - \frac{1}{\rho}\frac{\partial \overline{p}}{\partial x_i} - \frac{1}{\rho} F_i + g_i \quad (i, j = 1,2,3) \tag{3-5}$$

The additional terms F_i (= F_x, F_y, F_z = 0) represent the resistance force components per unit volume induced by vegetation in *x*, *y*, *z* directions, respectively. Some sort of spatial averaging has been done in arriving at these terms.

The resistance effect of vegetation is modelled by the drag force method (DFM). In this method, the resistance force due to vegetation is determined by the quadratic friction law. Consider a single stem (see Figure 3.1), the force f_i per unit depth is given by

$$f_i = \frac{1}{2} \rho C_d b_v u_i \sqrt{u_j u_j} \quad (i = 1,2;\ j = 1,2,3) \tag{3-6}$$

where C_d = drag coefficient of stem; b_v = width of stem. The drag force is due to the wake formation downstream of the stem. The average force per unit volume within the vegetation domain is obtained by

$$F_i = N f_i = \frac{1}{2} \rho f_{rk} u_i \sqrt{u_j u_j} \quad (i = 1,2;\ j = 1,2,3) \tag{3-7}$$

where N = number density (number of stems per unit area, in m^{-2}) and $f_{rk} = C_d b_v N$ =

$C_d \cdot \alpha$. Previous experimental studies (Dunn *et al.* 1996) have showed that the value of C_d of circular cylinder rods in open channels is not constant in the vertical; the value reaches a maximum at distances close to one third of canopy height with a mean value close to $C_d = 1.13 \pm 0.15$.

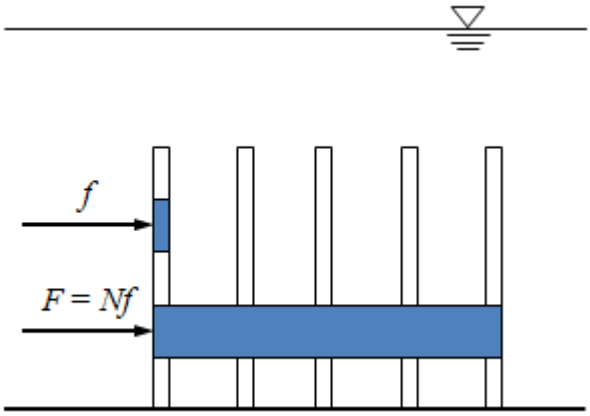

Figure 3.1. Drag force induced by flow through vegetation

The Reynolds averaging gives rise to the velocity correlations $\overline{u_i' u_j'}$ which come from the non-linearities of the N-S equations and govern the interaction between the mean flow and the fluctuating motion. They can be interpreted as apparent stresses $\rho\overline{u_i' u_j'}$ which form the Reynolds stress tensor. This tensor is symmetric and thus has six independent components. As the system of Equation (3-4 and 3-5) involves more unknowns than equations, it requires a turbulence model to close the problem. A variety of turbulence models have been proposed and reported in the literatures, which, depending on the general approach adopted to model the Reynolds stress terms, can be classified as isotropic eddy viscosity models, non-linear eddy-viscosity models and Reynolds-stress models. Most turbulence models used for numerical modelling of

open-channel flows are based on the so-called 'Boussinesq approximation' which was suggested by Boussinesq in 1877. It relates the Reynolds stress (τ_{ij}) to the mean strain-rate tensor, S_{ij} ($=\frac{1}{2}\left(\frac{\partial \overline{u}_i}{\partial x_j}+\frac{\partial \overline{u}_j}{\partial x_i}\right)$), through the equation:

$$\frac{\tau_{ij}}{\rho}=-\overline{u_i'u_j'}=\nu_t\left(\frac{\partial u_i}{\partial x_j}+\frac{\partial u_j}{\partial x_i}\right)-\frac{2}{3}k\delta_{ij} \tag{3-8}$$

where k ($=\frac{1}{2}\overline{u_i'u_i'}$) is the TKE (per unit mass) that may be incorporated into the pressure term in the numerical scheme, and δ_{ij} is the Kronecker delta and ν_t is the kinematic eddy viscosity. The eddy viscosity ν_t herein is a scalar and hence is the same for all stress components, i,e., the eddy viscosity is isotropic.

In the present study the eddy viscosity ν_t is specified by the S-A turbulence model which is a relatively recent and simpler isotropic eddy-viscosity model. The S-A model is a one-equation statistical turbulence model (Spalart and Allmaras 1994). This model involves the solution of a new eddy viscosity variable $\tilde{\nu}$ and includes eight closure coefficients and three closure functions. The governing equations are as follows.

$$\nu_t=\tilde{\nu}f_{\nu 1} \tag{3-9}$$

$$\frac{\partial \tilde{\nu}}{\partial t}+u_j\frac{\partial \tilde{\nu}}{\partial x_j}=c_{b1}\tilde{S}_\nu\tilde{\nu}+\frac{1}{\sigma}\left\{\frac{\partial}{\partial x_k}\left[\left(\tilde{\nu}+\nu_m\right)\left(\frac{\partial \tilde{\nu}}{\partial x_k}\right)\right]+c_{b2}\left(\frac{\partial \tilde{\nu}}{\partial x_k}\frac{\partial \tilde{\nu}}{\partial x_k}\right)\right\}-c_{w1}f_w\left(\frac{\tilde{\nu}}{L}\right)^2 \tag{3-10}$$

where: $f_{\nu 1}=\frac{\chi^3}{\chi^3+c_{\nu 1}^3}$, $f_{\nu 2}=1-\frac{\chi}{1+\chi f_{\nu 1}}$, $f_w=g\left[\frac{1+c_{w3}^6}{g^6+c_{w3}^6}\right]^{1/6}$, $\tilde{S}_\nu=S_\nu+\frac{\tilde{\nu}}{\kappa^2L^2}f_{\nu 2}$,

$S_\nu=\sqrt{\omega_j\omega_j}$, $\chi=\frac{\tilde{\nu}}{\nu_m}$, $g=r+c_{w2}\left(r^6-r\right)$, $r=\frac{\tilde{\nu}}{\tilde{S}_\nu\kappa^2L^2}$, $c_{b1}=0.1355$, $c_{b2}=0.622$,

$c_{v1} = 7.1,\ \sigma = 2/3,\ c_{w1} = \frac{c_{b1}}{\kappa^2} + \frac{1 + c_{b2}}{\sigma},\ c_{w2} = 0.3,\ c_{w3} = 2$. L is a turbulence length scale equal to the normal distance to the nearest wall. S_F is an additional source term due to vegetation.

The left-hand side of Equation 3-10 represents local and convective changes of transport variable $\tilde{\nu}$; On the right hand side of Equation 3-10, the first term represents the production of turbulent energy and hence eddy viscosity due to vorticity, the second term represents the diffusion of turbulent energy, and the last term represents the destruction of turbulent energy. The new variable $\tilde{\nu}$ was introduced to account for transitional flow behavior. The values of the model coefficients have been determined through the model calibration against experimental data of mixing layer flows, wake flows and wall-bounded flows. The S-A model is simpler than the commonly used *k*-*ε* or *k*-*ω* model and it has been successfully applied in the modelling of certain free-shear flow, wall-bounded flow and separated flow problems (Breuer *et al.* 2003). This model is complete for practical applications as the turbulence scales are automatically defined, i.e., no adjustable closure coefficient is involved.

The S-A model has been developed mainly for aerodynamic flows. This model is basically a transport equation for the eddy viscosity, and is quite popular because of its reasonable results for a wide range of flow problems and its numerical properties. This model has given good results for transonic turbulent flow in complex industrial configuration and for slightly separated flow in over-expanded nozzles. This model is developed under the so-called ‘Boussinesq hypothesis’. The main limitation of the

S-A model includes: (1) it is an isotropic model which cannot be used to reproduce the anisotropic phenomenon, such as the velocity dip and secondary current; (2) the turbulence kinetic energy cannot be explicitly solved in the S-A model; (3) the S-A model is not well suited to applications involving jet-like free-shear regions.

3.2.3. Numerical methods

3.2.3.1. σ-coordinate transformation

As the most commonly used coordinate system, the Cartesian coordinates is not quite suitable to represent irregular bottom. Furthermore, with the Cartesian coordinate, the computed free surface could normally cross the computational cell arbitrarily. This leads to the difficulty of applying the pressure boundary condition precisely on the free surface and may eventually affect the accuracy of velocity computation nearby. However, the σ-coordinate transformation, which was firstly introduced by Phillips (1957), can overcome these problems. The σ coordinates have been widely used in computational models for oceanography, meteorology and other such Earth science fields with a focus on fluid dynamics. It basically maps the varying vertical coordinate in the physical domain to a uniform transformed space where σ spans from 0 to 1 (as shown in Figure 3.2). In this study, assuming the free surface is a single function of the horizontal plane, a slightly modified σ-coordinate developed by Lin and Li (2002) is introduced as follows,

$$\tau = t \qquad \xi^1 = x \qquad \xi^2 = y \qquad \xi^3 = \sigma = \frac{z + h^*}{D} = \frac{z + h^*}{h + \eta} \qquad (3\text{-}11)$$

where (x, y, z, t) are space and time coordinates in Cartesian coordinate system; (ξ^1, ξ^2, ξ^3, τ) the space and time coordinates in the σ coordinate system; D (= h^* + η) is

the total water depth, h^* is the depth measured from $z = 0$, η is the surface elevation.

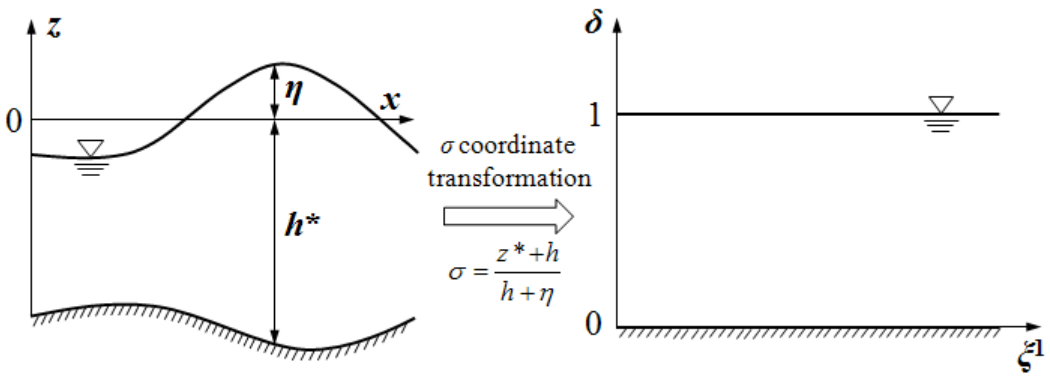

Figure 3.2. Illustration of σ-coordinate transformation

By applying Equation 3-11 to Equations 3-4, 3-5 and 3-10, the governing equations in the new coordinate (ξ^1, ξ^2, ξ^3, τ) can be obtained as follows:

$$\frac{\partial \overline{u}_i}{\partial \xi^k}\frac{\partial \xi^k}{\partial x_i} = 0 \tag{3-12}$$

$$\begin{aligned}&\frac{\partial \overline{u}_i}{\partial \tau} + \frac{\partial \overline{u}_i}{\partial \xi^k}\frac{\partial \xi^k}{\partial t} + u_j\frac{\partial \overline{u}_i}{\partial \xi^k}\frac{\partial \xi^k}{\partial x_j}\\ &= \nu\frac{\partial \xi^k}{\partial x_j}\frac{\partial}{\partial \xi^k}\left(\frac{\partial \overline{u}_i}{\partial \xi^m}\frac{\partial \xi^m}{\partial x_j}\right) + \frac{\partial \tau_{ij}}{\partial \xi^k}\frac{\partial \xi^k}{\partial x_j} - \frac{1}{\rho}\frac{\partial \overline{p}}{\partial \xi^k}\frac{\partial \xi^k}{\partial x_i} - \frac{1}{\rho}F_i + g_i\end{aligned} \tag{3-13}$$

$$\begin{aligned}&\frac{\partial \nu}{\partial \tau} + \frac{\partial \nu}{\partial \xi^k}\frac{\partial \xi^k}{\partial t} + u_j\frac{\partial \nu}{\partial \xi^k}\frac{\partial \xi^k}{\partial x_j}\\ &= c_{b1}\tilde{S}_\nu\nu + \frac{1}{\sigma}\left\{\frac{\partial \xi^k}{\partial x_j}\frac{\partial}{\partial \xi^k}\left[\frac{\partial \nu}{\partial \xi^m}\frac{\partial \xi^m}{\partial x_j}\right]\right.\\ &\left. + c_{b2}\left(\frac{\partial \nu}{\partial \xi^m}\frac{\partial \xi^m}{\partial x_j}\right)\left(\frac{\partial \nu}{\partial \xi^m}\frac{\partial \xi^m}{\partial x_j}\right)\right\} - c_{w1}f_w\left(\frac{\nu}{d}\right)^2\end{aligned} \tag{3-14}$$

In particular,

$$\frac{\partial \xi^3}{\partial t} = \frac{\partial \sigma}{\partial t} = -\frac{\sigma}{D}\frac{\partial D}{\partial \tau} \tag{3-15}$$

$$\frac{\partial \xi^3}{\partial x_1} = \frac{\partial \sigma}{\partial x} = \frac{1}{D}\frac{\partial h^*}{\partial \xi^1} - \frac{\sigma}{D}\frac{\partial D}{\partial \xi^1} \tag{3-16}$$

$$\frac{\partial \xi^3}{\partial x_2} = \frac{\partial \sigma}{\partial y} = \frac{1}{D}\frac{\partial h^*}{\partial \xi^2} - \frac{\sigma}{D}\frac{\partial D}{\partial \xi^2} \tag{3-17}$$

$$\frac{\partial \xi^3}{\partial x_3} = \frac{\partial \sigma}{\partial z} = \frac{1}{D} \tag{3-18}$$

In the new coordinate system, the Reynolds stresses can be calculated as follows,

$$\tau_{11} = 2\nu_t\left(\frac{\partial \overline{u}}{\partial \xi^1} + \frac{\partial \overline{u}}{\partial \sigma}\frac{\partial \sigma}{\partial x}\right) \qquad \tau_{12} = \tau_{21} = \nu_t\left(\frac{\partial \overline{u}}{\partial \xi^2} + \frac{\partial \overline{u}}{\partial \sigma}\frac{\partial \sigma}{\partial y} + \frac{\partial \overline{v}}{\partial \xi^1} + \frac{\partial \overline{v}}{\partial \sigma}\frac{\partial \sigma}{\partial x}\right)$$

$$\tau_{22} = 2\nu_t\left(\frac{\partial \overline{v}}{\partial \xi^2} + \frac{\partial \overline{v}}{\partial \sigma}\frac{\partial \sigma}{\partial y}\right) \qquad \tau_{13} = \tau_{31} = \nu_t\left(\frac{\partial \overline{u}}{\partial \sigma}\frac{\partial \sigma}{\partial z} + \frac{\partial \overline{w}}{\partial \xi^1} + \frac{\partial \overline{w}}{\partial \sigma}\frac{\partial \sigma}{\partial x}\right) \tag{3-19}$$

$$\tau_{33} = 2\nu_t\left(\frac{\partial \overline{w}}{\partial \sigma}\frac{\partial \sigma}{\partial z}\right) \qquad \tau_{23} = \tau_{32} = \nu_t\left(\frac{\partial \overline{v}}{\partial \sigma}\frac{\partial \sigma}{\partial z} + \frac{\partial \overline{w}}{\partial \xi^2} + \frac{\partial \overline{w}}{\partial \sigma}\frac{\partial \sigma}{\partial y}\right)$$

3.2.3.2. Split operator method

A split operator method is used in the solution of the governing equations. At each time interval, the momentum equations are split into three steps: advection, diffusion and pressure propagation. The momentum equations can be written in the following forms:

$$\frac{\partial \overline{u}_i}{\partial \tau} = A(\overline{u}_i) + D(\overline{u}_i) + P(\overline{p}) \tag{3-20}$$

where *A* denotes the advection operators, *D* denotes the diffusion operators and *P* denotes the pressure gradient and body force operators.

In the advection step, the equations to be solved are listed as follows:

$$\frac{(\bar{u}_i)^{n+1/3}-(\bar{u}_i)^n}{\Delta\tau}=A(\bar{u}_i)^n=-\left(\frac{\partial\bar{u}_i}{\partial\xi^k}\frac{\partial\xi^k}{\partial t}-u_j\frac{\partial\bar{u}_i}{\partial\xi^k}\frac{\partial\xi^k}{\partial x_j}\right)^n \tag{3-21}$$

where $\Delta\tau$ is the time step size, and the superscript n+1/3 represents the first intermediate step among these three steps. Similar symbols are also used in the following equations.

The method of characteristics is used to solve the above equation. Assuming the spatial variation of a function (e.g., velocity component) can be decomposed into a series of Fourier wave components, the schemes in this class of method produce an accurate solution for the advection of waves. In particular the phase accuracy is very high and the amplitude damping is quite small (Leonard 1979). Under a uniform grid the combination of the quadratic backwards characteristics method and the Lax-Wendroff method gives the Minimax characteristics method (Li 1990). Lin and Li (2002) has successfully implemented this method on non-uniform grids. The Minimax characteristics method is also adopted here.

The diffusion process is solved after the advection is completed. In the diffusion step, the following equation is to be solved:

$$\frac{(\bar{u}_i)^{n+2/3}-(\bar{u}_i)^{n+1/3}}{\Delta\tau}=D(\bar{u}_i)^{n+1/3}=\left(\nu\frac{\partial\xi^k}{\partial x_j}\frac{\partial}{\partial\xi^k}\left(\frac{\partial\bar{u}_i}{\partial\xi^m}\frac{\partial\xi^m}{\partial x_j}\right)+\frac{\partial\tau_{ij}}{\partial\xi^k}\frac{\partial\xi^k}{\partial x_j}\right)^{n+1/3} \tag{3-22}$$

In the pressure propagation step, the equation to be solved is listed as follow:

$$\frac{(\bar{u}_i)^{n+1}-(\bar{u}_i)^{n+2/3}}{\Delta\tau}=P(\bar{p})^{n+1}=\left(-\frac{1}{\rho}\frac{\partial\bar{p}}{\partial\xi^k}\frac{\partial\xi^k}{\partial x_i}\right)^{n+1}-\frac{1}{\rho}F_i+g_i \tag{3-23}$$

The central difference scheme in space is used to discretize the Equations 3-22 and 3-23. For continuity requirement, the Equation 3-23 is substituted into the continuity equation to give the Poisson pressure equation.

The eddy viscosity equation 3-14 is split into two steps: advection and diffusion with source. The same procedures for the solution of the momentum equations are used in the solution of the eddy viscosity equation, i.e., the Minimax characteristics method and the central difference scheme are adopted in the advection step and diffusion step, respectively.

3.2.3.3. CGSTAB method

The Poisson pressure equation obtained after the σ-coordinate transformation and aforementioned discretization can be written in the following general form:

$$Aq = b \tag{3-24}$$

where A is a sparse matrix which contains information of mesh system, free surface, bottom geometry and boundary conditions; q is the vector of to-be-solved pressure ($\overline{p}^{n+1}$); b is the known vector which contains information of sources and boundary conditions.

In order to solve the Equation 3-24, the so-called conjugate gradient squared stabilized (CGSTAB) method was utilized in the present simulations. This method was first proposed by Van den Vorst and Sonneveld (1990) and further modified by Van der Vorst (1992). It can be applied to non-symmetric matrices and to both structured and unstructured meshes. Comparing to the classical Gauss-Seidel method,

this method was confirmed to be able to significantly shorten the computational time under the same convergence criterion.

3.2.4. Boundary conditions

Various types of boundary conditions have been implemented in the model. And the boundary conditions are applied at each split step. The free surface is an interface of water and air, at which both the dynamic and kinematic conditions should be satisfied. Neglecting the surface tension and the wind stress on the free surface, the dynamic condition can be given as follow:

$$p = 0, \quad \frac{\partial u_i}{\partial \sigma} = 0 \tag{3-25}$$

Assuming the surface is smooth and no overturning occurs, the kinematic condition can be given as follows:

$$\frac{\partial \eta}{\partial t} = \overline{w} - \overline{u}\frac{\partial \eta}{\partial x} - \overline{v}\frac{\partial \eta}{\partial y} \tag{3-26}$$

The equation is an advection equation, which can be solved by the method of characteristics. In the present model the backward characteristics method with quadratic interpolation polynomial is used.

Based on the no-slip boundary condition, particle velocities in all directions need to be zero on a bottom or solid wall. This treatment, however, is accurate only when fairly fine meshes are used to revolve the bottom boundary layer. Alternatively, the zero gradient boundary condition (e.g., $\partial \overline{u}/\partial \sigma = 0$) can be used to estimate velocity gradients at the first interior node, which will be subsequently used in the advection

calculation. Meanwhile, the log-law wall function is used to calculate the wall shear stress that will be used in diffusion step. The latter method can produce reasonable results when relatively coarse meshes are adopted.

The wall function applied in zero gradient boundary condition is given as follow:

$$\frac{\bar{u}}{u*} = \frac{1}{\kappa}\ln\left(E \cdot z^{+}\right) \tag{3-27}$$

where $u*$ is the shear velocity and E is the logarithmic law constant. For hydraulically-smooth boundaries, a value of E = 9.0 is recommended, and for hydraulically–rough boundaries, the following formula suggested by Naot and Emrani (1982) is used to estimate E:

$$E = \frac{9}{1+\left(\frac{0.3 \cdot k_s^{+}}{1+20/k_s^{+}}\right)} \tag{3-28}$$

where k_s^{+} is the dimensionless roughness height (= $k_s u*/\nu$).

To obtain the value of $u*$ an iteration is made, once the distance z and the fluid velocity $\bar{u}$ have been chosen. The wall function can be rewritten as:

$$u* = \frac{\bar{u}\kappa}{\ln\left(\frac{Ezu*}{\nu}\right)} \tag{3-29}$$

The iteration can be made subsequently by successive approximations, yielding the value of $u*$, the use of the Newton Raphson's method has been of utility to greatly accelerate the convergence.

At the inflow boundary, the inflow rate with a predetermined velocity distribution is

specified and the gradient of the water surface elevation is assumed to be zero. At the outflow boundary, the water surface elevation is specified and the velocity gradients are assumed to be zero.

3.3. Case studies

3.3.1. Open-channel flows over smooth surface

The 3D RANS model is initially tested by replicating the laboratory experiments of a fully developed open-channel flow over smooth bed, which were conducted by Nezu and Rodi (1986). The experiments were carried out in a tilting flume of rectangular cross-section. The flume is 20 m long, 0.6 m wide and 0.65 m high. Two of the experimental conditions were selected (as shown in Table 3.1). It can seen that the flows in these two cases are fully turbulent according to the Reynolds number Re (= $4DU/\nu$) and subcritical according to the Froude number Fr ($=U/\sqrt{(gD)}$). While Case 1 belong to the low-Reynolds number situation (say for $Re_\tau < 500$, $Re_\tau = D \cdot u^*/\nu$), the Case 2 is at the much higher Reynolds number ($Re_\tau = 2143$).

Table 3.1. Flow parameters for the simulations (experiments by Nezu and Rodi 1986)

Case	D [cm]	$S_0 \times 10^{-4}$	Q [l/s]	W/D	Fr	Re	Re_τ
Case 1	10.1	< 1.0	4.6	5.9	0.077	2.3×10^4	439
Case 2	7.7	12.5	27.4	7.8	0.680	14.5×10^4	2,143

In the computation the domain is of length 15 m and width 0.6 m. The mean height is equal to the water depths which are listed in Table 3.1 for these two cases. The uniform meshes were used in the streamwise and spanwise directions while a rectilinear grid with refinement at the near bottom region was employed in the vertical direction. The grid numbers were $151 \times 21 \times 41$ in streamwise, spanwise and vertical directions for Case 1 and $151 \times 21 \times 39$ for Case 2. The time step is 0.001 s. The grids and the time step were found to be sufficiently small to obtain grid convergent results. In order to obtain the mean velocity within the viscous sublayer, the no-slip boundary condition was applied on the bottom. The zero gradient boundary condition was applied on the side walls.

The computed vertical velocity profiles after a steady state are shown in Figure 3.3 and Figure 3.4, together with the corresponding experimental data (Nezu and Rodi 1986) and reported DNS results by Hoyes and Jimenez (2006) and del Alamo and Jimenez (2003). The profiles are shown in semi-logarithmic scale with $u^+ = \bar{u}/u*$ and $z^+ = z \cdot u*/\nu$. It can be seen from these figures that the computed profiles agree well with the experimental data and the DNS results for both low-Reynolds-number case (Case 1) and high-Reynolds-number case (Case 2). The computed velocity profile for Case 1 (Figure 3.3) indicates the low-Reynolds number effect compared to the computed velocity profile for Case 2 (Figure 3.4). For one thing, the simulation for Case 1 has a shorter log layer; for another, the apparent log law in Case 1 has a larger intercept than in the higher Reynolds number flows (Case 2).

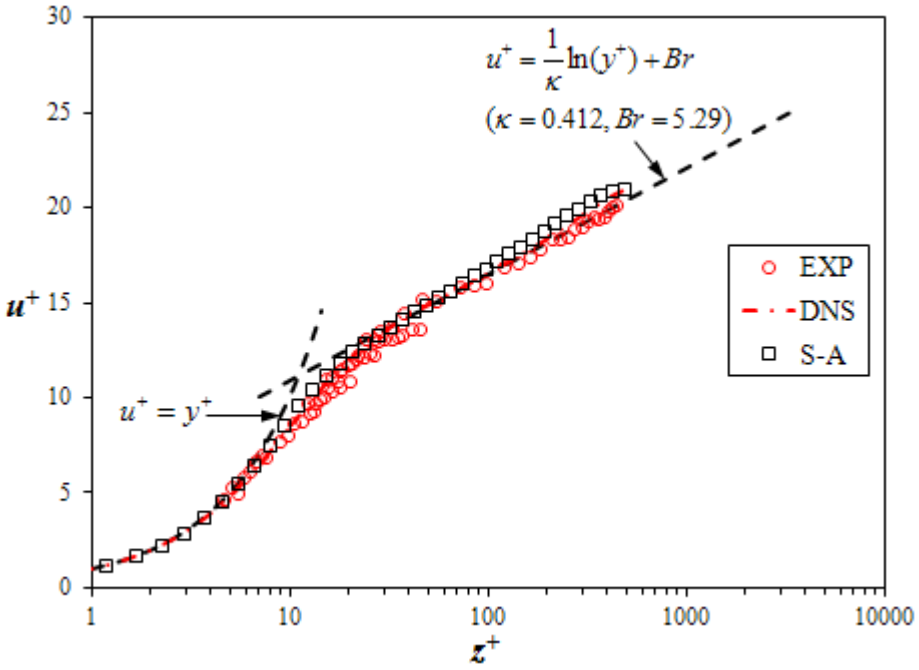

Figure 3.3. Profile of mean streamwise velocity for Case 1

(experiments by Nezu and Rodi 1986)

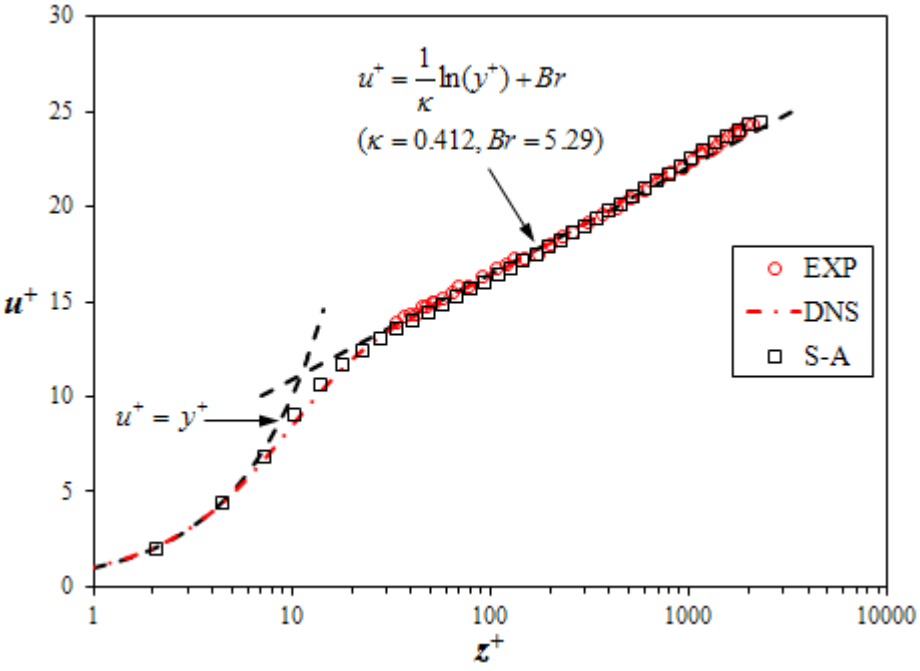

Figure 3.4. Profile of mean streamwise velocity for Case 2

(experiments by Nezu and Rodi 1986)

The comparison between the measured and computed eddy viscosity for Case 1 and Case 2 are shown in Figure 3.5. The agreement is fairly good which indicates that the transport equation for eddy viscosity (Equation 3-10) performs well for the open-channel flows over smooth surface.

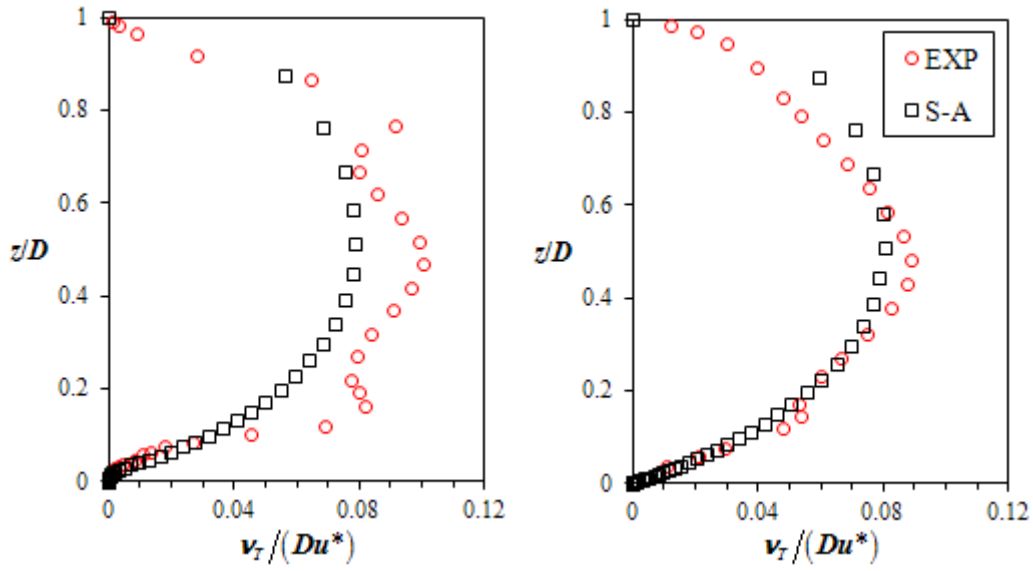

Case 1 inTable 3.1 Case 2 in Table 3.1

Figure 3.5. Profiles of eddy viscosity (experiments by Nezu and Rodi 1986)

The velocity fluctuation correlation component $-\overline{u'w'}$ can be derived from the computed mean velocity profile and the eddy viscosity using Equation 3-8. Figure 3.6 compares computed $-\overline{u'w'}$ with the flume measurements of Nezu and Rodi (1986) and the corresponding DNS results (del Alamo and Jimenez 2003; Hoyas and Jimenez 2006). It can be seen that the agreement is excellent. The maximum value of Reynolds stress occurs in the near-wall region. The Reynolds stress varies linearly from the maximum value to zero at the free surface.

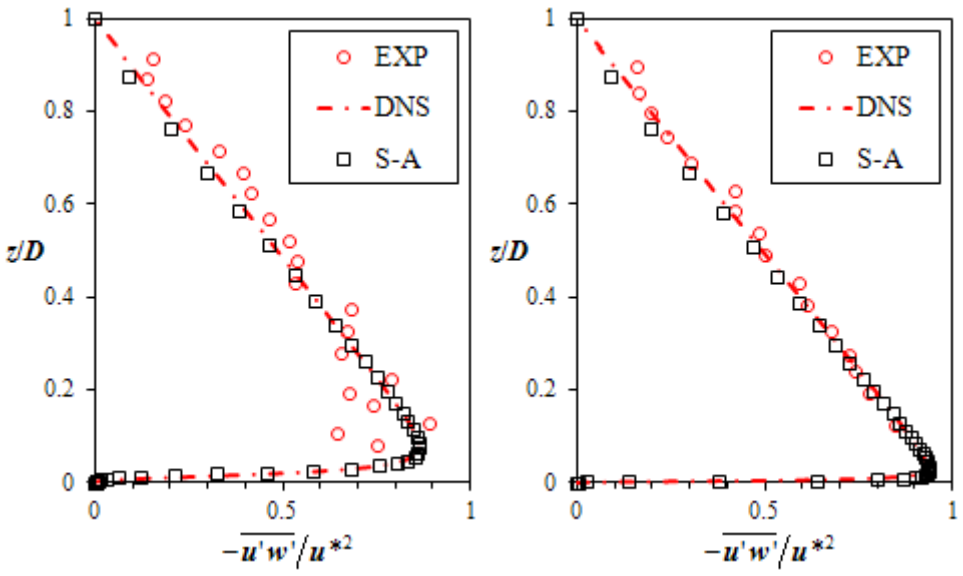

Case 1 inTable 3.1 Case 2 in Table 3.1

Figure 3.6. Profiles of Reynolds stress (experiments by Nezu and Rodi 1986)

Since the turbulence kinetic energy (TKE) cannot be explicitly solved in the S-A model, the TKE has to be calculated empirically. For isotropic turbulence, the TKE (per unit mass) can be obtained from the following equation (Rung *et al.* 2003):

$$k = \frac{\sqrt{2S_{ij}S_{ij}}}{\sqrt{c_\mu}} \tag{3-30}$$

where S_{ij} is the mean-strain-rate tensors ($=\frac{1}{2}\left(\frac{\partial \overline{u}_i}{\partial x_j}+\frac{\partial \overline{u}_j}{\partial x_i}\right)$); c_μ is a numerical constant (= 0.09).

Previous studies (Nezu and Nakagawa 1993) have revealed that the turbulence in the open-channel flows is anisotropic because of the side-wall effect. The side-wall effect eventually result in the redistribution of turbulence intensities $\overline{u'}$, $\overline{v'}$ and $\overline{w'}$. Due to the damping effect of the side walls in open-channel flows, *k*, which is

defined in the following equation, is reduced.

$$k \equiv \frac{1}{2}\left(\overline{u'^2} + \overline{v'^2} + \overline{w'^2}\right) = \frac{1}{2}\overline{u_i' u_i'} \tag{3-31}$$

All three components of turbulence intensity were firstly studied by Nakagawa *et al*. (1975) and were found to be in the following proportion for open-channel flows:

$$\overline{u'} : \overline{v'} : \overline{w'} = 1 : 0.55 : 0.71 \tag{3-32}$$

Consequently, for an identical case there exists a constant reduction coefficient *Cr* for the TKE between the isotropic turbulence condition and the anisotropic turbulence condition. This coefficient can be deduced from Equation 3-31 and Equation 3-32 as follow:

$$Cr = \frac{1^2 + 0.55^2 + 0.71^2}{1^2 + 1^2 + 1^2} = 0.6022 \approx 0.6 \tag{3-33}$$

By taking $Cr = 0.6$, k can be calculated for the open-channel flows as follow:

$$k = Cr \frac{\sqrt{2 S_{ij} S_{ij}}}{\sqrt{c_\mu}} \tag{3-34}$$

Based on extensive experimental measurements Nezu and Nakagawa (1993) found that the vertical distribution of k for open-channel flows follows the empirical equation:

$$k / u_*^2 = 4.78 \exp\left(-2z/D\right) \tag{3-35}$$

Figure 3.7 shows the computed results of k by using the Equation 3-34, together with

the corresponding DNS results and the Equation 3-35. Although the computed results were under-predicted in the near-wall region and near-water-surface region, they were in great agreement with DNS results and experimental data in the intermediate region for both Case 1 and Case 2. The fairly good agreement indicates that the Equation 3-34 performs well for the empirically estimation of TKE for open-channel flows over smooth surface.

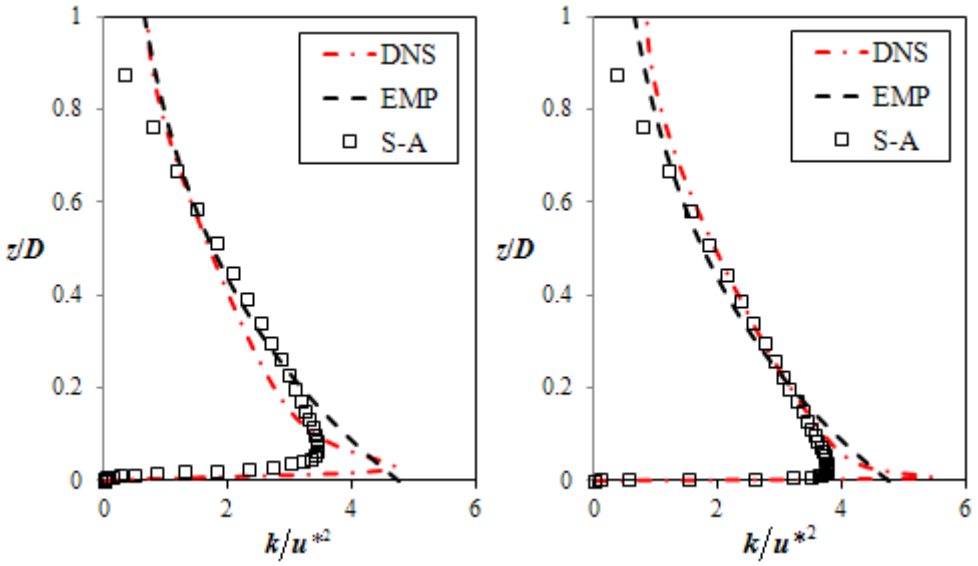

Case 1 inTable 3.1 Case 2 in Table 3.1

Figure 3.7. Profiles of TKE (experiments by Nezu and Rodi 1986)

3.3.2. Open-channel flows over submerged vegetation

The 3D RANS model is subsequently tested by replicating the flume experiments of fully developed vegetative open-channel flows, which were conducted by Dunn *et al.* (1996). The experiments were conducted under uniform conditions in a 19.5 m long, 0.91 m wide and 0.61 m deep tilting flume. Vegetation was simulated by rigid wooden cylinders and flexible plastic commercial drinking straws, and arranged in a

staggered pattern with variable density. A SonTek acoustic Doppler velocimeter (ADV) was used to measure the three velocity components instantaneously at a section at least 1.5 m downstream of the first row of cylinders to ensure the establishment of a fully developed flow condition. Two cases with the primary flow parameters listed in Table 3.2 were chosen for the model test. It can be seen from this table that the primary flow parameters for these two cases are almost identical, with the same bed slope, flow rate and vegetative coefficient. The essential difference between these two cases is the stem flexibility, with rigid vegetation for Case 1 and flexible vegetation for Case 2. While the wooden cylinders did not deflect for Case 1, the flexible cylinders were found not only deflected under the flow of water, but also vibrated and swayed in both vertical and transverse directions. Thus the canopy height is the undeflected canopy height h_v = 0.1175 m for Case 1 and the averaged deflected height $\overline{h_d}$ = 0.152 m for Case 2.

Table 3.2. Flow parameters for the simulations (experiments by Dunn *et al.* 1996)

Case	D [m]	S_0	Q [l/s]	α	f_{rk} [m^{-1}]	Cylinder Flexibility
Case 1	0.335	0.0036	179	1.09	1.23	rigid
Case 2	0.368	0.0036	179	1.09	1.23	flexible

The computational domain is of length 15 m, width 0.91 m. The mean height is equal to the water depths which have been included in Table 3.2. The uniform meshes were adapted in the streamwise, spanwise and vertical directions. The mesh size of 151 × 21 × 41 was selected for these two cases. The time step was 0.0015 s. The computations were performed with C_d = 1.13 which was the mean value suggested by Dunn *et al.*(1996) and confirmed to be valid for both rigid cylinder-type and

flexible film-type stems (Yang and Choi 2009). The zero gradient boundary condition was applied to the bottom and the side walls.

Figure 3.8 shows the computed vertical velocity profiles after a steady state have been reached. Four sets of vertical profiles, which were measured at various locations within the cylinders, also plotted for comparison. It can be seen that the computed profile is in close agreement with the experimental data for both rigid cylinder case (Case 1) and the flexible cylinder case (Case 2). The vegetation resistance produces a velocity defect at the vegetation region and the continuity requirement redirects the flow to the region above the vegetation. The velocity profiles, therefore, departs from the logarithmic distribution for open-channel flows.

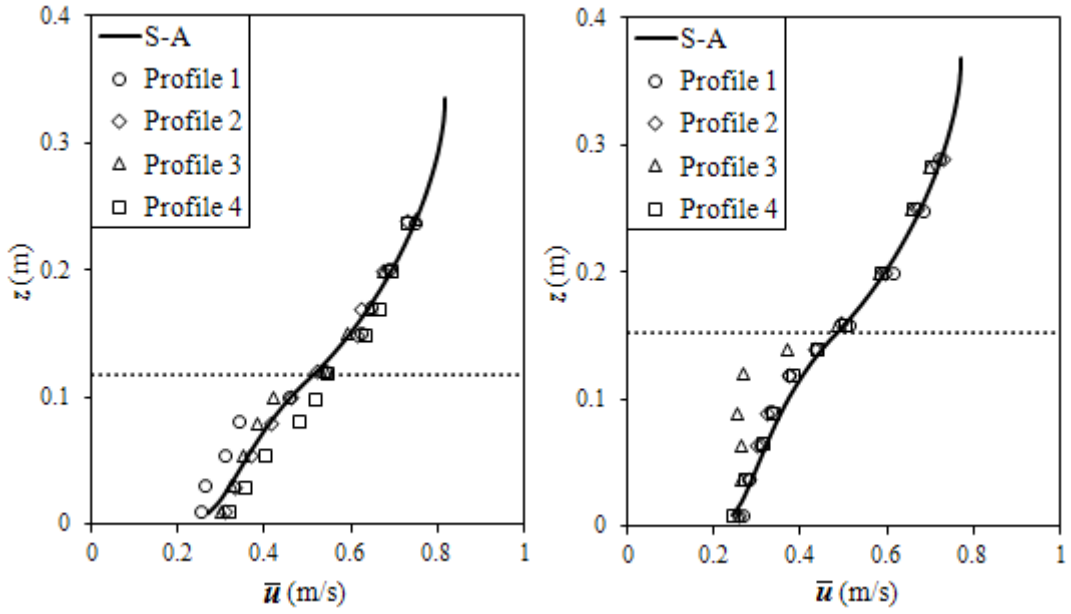

Case 1 in Table 3.2 Case 2 in Table 3.2

Figure 3.8. Profiles of mean streamwise velocity (experiments by Dunn *et al.* 1996)

(The dot line denotes the canopy height)

Figure 3.9 shows the comparison of velocity fluctuation correlation component $-\overline{u'w'}$ between the computed profiles and the experimental measurements. A fairly good agreement between experimental values and model predictions is observed for flow within the vegetation canopy. The computed values, however, were found to be greater than the experimental measurements above the simulated canopy. This phenomenon is typical of free surface flows (Nezu and Nakagawa 1993) and can be explained by the action of secondary currents. The secondary currents are caused by the side-wall effect and cannot be reproduced by the isotropic turbulence model. This effect appears to be more evident with a smaller width-to-depth ratio (aspect ratio) in flume experiments. It can be also concluded from Figure 3.8 and Figure 3.9 that the DFM performs well for simulating the resistance effect of rigid and flexible cylinder canopy.

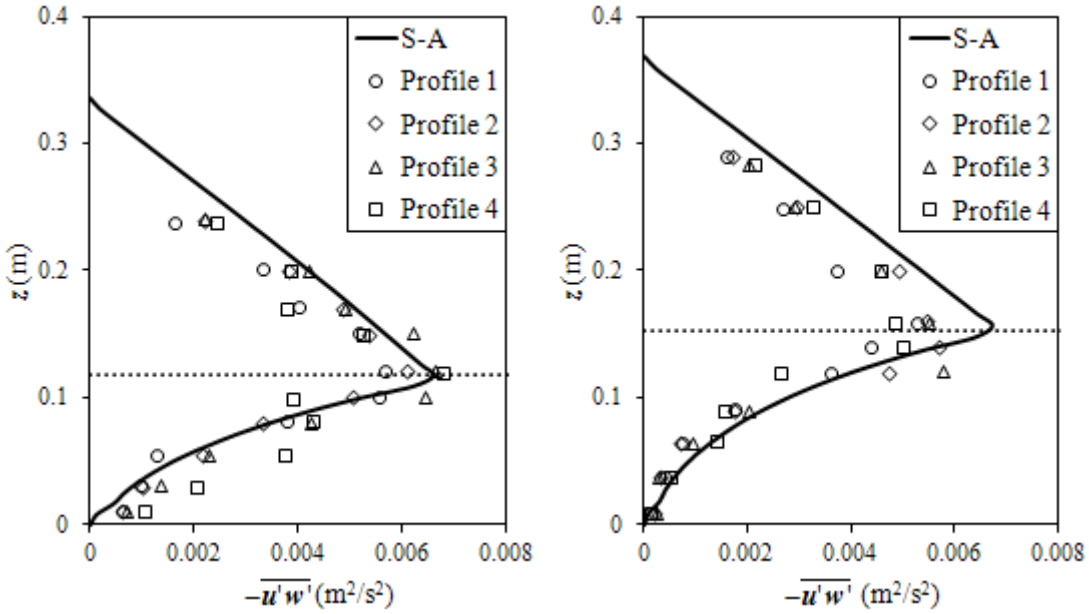

Case 1 in Table 3.2 Case 2 in Table 3.2

Figure 3.9. Profiles of Reynolds stress (experiments by Dunn *et al.* 1996)

(The dot line denotes the canopy height)

3.4. Conclusions

Numerical model is a cost-effective tool for solving engineering problems involving open-channel flows. In this chapter, a 3D RANS model is described and used for simulating open-channel flows. The popular S-A one-equation model, which has been widely used in the aeronautical applications, was adopted for the turbulence closure. The governing equations, S-A model and the adapted numerical solution algorithm are described in detail. The numerical model was validated with two cases: open-channel flow with smooth surface (Nezu and Rodi 1986), and open-channel flow with submerged vegetation canopy (Dunn *et al.* 1996). The good agreement with the experimental data confirms the applicability of the S-A model in the modelling of open-channel water flow. The DFM performed well in simulating the flow resistance induced by rigid or flexible vegetation canopy.

Chapter 4.

Numerical Modelling of Flows over Gravel Beds

4.1. Introduction

The roughness elements in gravel-bed open-channel flows vary in size and shape from site to site. Depending on the depth sediment ratio D/d_{50}, where D = water depth and d_{xx} refers to the element diameter of which xx% by weight of the elements have smaller diameters, the bed surface condition can be subdivided into two categories. One is small-scale roughness for which D is much larger than d_{50} and the other is large-scale roughness for which D is of the same order as d_{50}. For the condition of small-scale roughness, it is conventional to consider the flow as a perturbed boundary layer flow. As shown in Figure 4.1, two different flow regions can be identified in the vertical direction: the inner (or near-wall) region and the outer (or near-water-surface) region. In the inner region, the logarithmic velocity distribution is valid (Kirkgoz and Ardiclioglu 1997). For the condition of large-scale roughness, if d_{50} is comparable to D (say $D/d_{50} < 2.0$), the flow can be assumed to be a mixing layer flow (Katul *et al.* 2002). The flow velocity profile may be of S-shape (Figure 4.2) with near-surface velocities much larger than near-bed velocities (Ferro and Baiamonte 1994). This velocity field of this particular profile can also be subdivided into two zones: (1) a lower zone, located within the roughness layer, in which flow velocities are substantially reduced

by resistant effects of the gravels; (2) an upper zone, located above the roughness layer, in which a quasi-smooth flows with higher velocities occurs. According to Bathust (1988), two situations are suitable for the development of the S-shape profile. One is that the bed slope should be above 1% and the depth sediment ratio D/d_{84} should be within the range of 1 to 4. The other is that the roughness elements should have evident non-uniform size distribution to allow the development of the lower zone flow. The criterion differentiating the small-scale and large-scale roughness is not clear-cut, and depends on the shape, concentration and arrangement of the roughness elements. According to the field measurements of two shallow gravel-rivers by Franca and Lemmin (2009), the S-shape velocity profiles were a consequence of local protrusions on the riverbed and exist concurrently with log-shape profiles in the same river cross section. In the near-bed region the time-averaged velocities will not follow the logarithmic law because the roughness geometry introduces too many length scales which influence velocity statistics. Nikora *et al.* (2004) further subdivided the roughness layer into a form-induced sublayer and an interfacial sublayer. The velocity distribution within the interfacial sublayer can be exponential, linear or constant, depending on the roughness geometry and flow condition.

RANS models may not be accurate enough to simulate the flow within the gravel layer if the degree of porosity is low. The flow there will be obstructed significantly by the gravels and will be highly heterogeneous. In this situation the Double Averaged Navier-Stokes (DANS) approach will be more appropriate. This chapter describes the development of a DANS model, which includes the drag term, the form-induced stress term, the porosity and the turbulence closure terms, to simulate the roughness effects induced by the complex surface topography in gravel-bed

open-channel flows. The velocity profiles in the whole flow region, including the interfacial sublayer, form-induced layer and logarithmic layer are covered. The gravel-induced resistance effect is simulated by a drag force method (DFM) and the turbulence is parameterized by using the S-A model with a modification of the turbulence length scale in the interfacial sublayer. The performance of the proposed model was evaluated by extensive tests against available laboratory and field measurements. All tests gave great correspondence between the computed and measured velocity profiles.

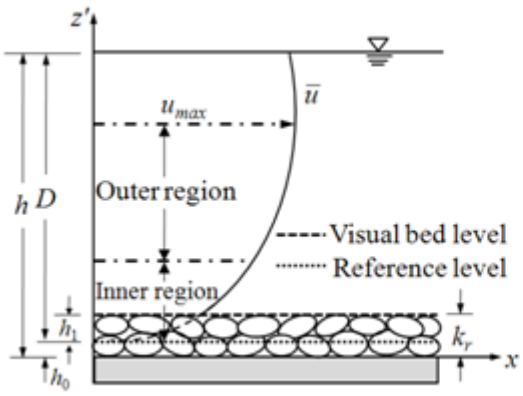

Figure 4.1. Velocity distribution over small-scale roughness elements

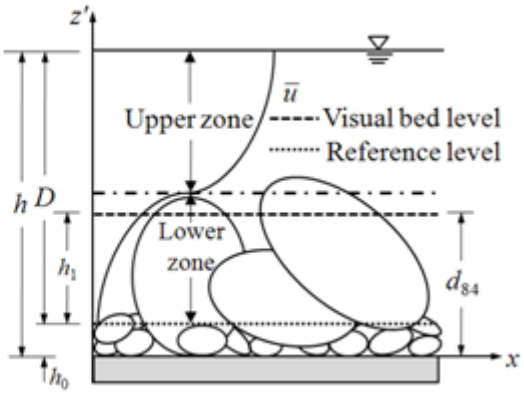

Figure 4.2. Velocity distribution over large-scale roughness elements

4.2. DANS model

Generally it is not economical to numerically simulate flows over rough-beds with large gravels using the traditional Reynolds Averaged Navier Stokes equations (RANS) approach or the Large Eddy Simulation (LES) approach since in these two approaches a very fine grid system is required to resolve the topography and the shapes of gravels.

A more practical and rigorous approach is to conduct temporal and spatial averaging of the governing equations and derive the DANS equations (Nikora *et al.* 2007a). In this chapter this set of equations are used in the development of a numerical model. For uniform flow the governing equations become one-dimensional. The continuity equation is given by:

$$\frac{\partial \langle \bar{u} \rangle}{\partial x} = 0 \tag{4-1}$$

The double-averaged (DA) momentum equation in the streamwise direction is given by:

$$\frac{\partial \langle \bar{u} \rangle}{\partial t} + \langle \bar{v} \rangle \frac{\partial \langle \bar{u} \rangle}{\partial y} + \langle \bar{w} \rangle \frac{\partial \langle \bar{u} \rangle}{\partial z} = \frac{1}{\phi} \frac{\partial}{\partial z} \left[\phi \tau_{xz} \right] + g_x - \frac{1}{\rho} \frac{F_x}{\phi} \tag{4-2}$$

where

$$\tau_{xz} = \left\langle \nu \frac{\partial \bar{u}}{\partial z} \right\rangle - \left\langle \overline{u'w'} \right\rangle - \langle \tilde{u}\tilde{w} \rangle \tag{4-3}$$

and x = streamwise ordinate; y = transverse ordinate; z = vertical ordinate with datum set at h_1 below the roughness element surface; ($\langle \bar{u} \rangle, \langle \bar{v} \rangle, \langle \bar{w} \rangle$) = DA velocity component in x, y, z directions; t = time; ρ = fluid density; ϕ = porosity; F_x = streamwise resistance force per unit volume induced by roughness elements; $g_x = gS_0$ = streamwise component of the gravitational acceleration and S_0 = bed slope. Comparing to the conventional time-averaged RANS equations, a new additional term (dispersive or form-induced stress, $= -\langle \tilde{u}\tilde{w} \rangle$) is introduced into the momentum equation due to spatial variations in time-averaged fields. This term represents the momentum flux induced by the spatial heterogeneity of the time-averaged flow. For the completely porous region above the roughness layer where $\phi = 1$, F_x = 0 and $-\langle \tilde{u}\tilde{w} \rangle = 0$, the DANS equation (Equation 4-2) takes the same form as the x-momentum RANS

equation. Recent studies have indicated that the form-induced stress is largely dependent on the roughness arrangement, physical geometry and flow conditions (Nikora *et al.* 2007b; Aberle *et al.* 2008; Manes *et al.* 2008). The experiments on open-channel flows over rods and artificial dunes have revealed that the magnitude of the form-induced stress increases significantly with increasing roughness spacing. The form-induced stress can be assumed negligible for flows with densely distributed small-scale roughness and contribute up to 30% of the total measured shear stress within the roughness layer for flows with sparely distributed large-scale roughness. However, it seems that no model equation has been developed to parameterize these stresses (Nikora *et al.* 2007b; Rameshwaran *et al.* 2011)

There are two possible approaches to pursue. The first is to make an analogy with the technique of LES by assuming that the form-induced stress term $-\langle \tilde{u}\tilde{w} \rangle$ is similar to the subgrid scale stress term. The form-induced stress term can then be parameterized by a sub-layer scale eddy viscosity model as follow:

$$-\langle \tilde{u}\tilde{w} \rangle = \tau_{xz}^{sgs} = \nu_s \frac{\partial \bar{u}}{\partial z} \tag{4-4}$$

where ν_s is the sub-layer scale eddy viscosity which can be calculated as follow:

$$\nu_s = \left(c_s \bar{\Delta}\right)^2 \left|\frac{\partial \bar{u}}{\partial z}\right| \tag{4-5}$$

where c_s is an empirical coefficient, $\bar{\Delta}$ is a length scale which can be taken as the characteristic grain diameters (viz, d_{50}, d_{84} or d_{90}). This model can produce a peak stress around the interface between the gravel layer and the water body above since the gradient of the velocity there is the largest. If c_s is real, the process is dissipative and will produce a reduction in the velocity and a redistribution of the total Reynolds

shear stress within the gravel layer. This is true in many cases. However, Nikora *et al*. (2007b) showed that the process can be anti-diffusive, which means that c_s can be imaginary. It is not very clear at the present moment how to determine the appropriate value of c_s.

The second approach is to absorb the stress into the drag force density term (the last term in Equation 4-2) and to calibrate the drag force (as shown in Equation 4-6). This method is simpler and is adopted in the present study. The shortcoming of this method is that the exact distribution of the form-induced stress is unknown.

$$-\frac{\partial}{\partial z}\left[\phi\langle\tilde{u}\tilde{w}\rangle\right]-\frac{1}{\rho}F_x=-\frac{1}{\rho}F_x' \tag{4-6}$$

Assuming secondary currents are unimportant, and using the eddy viscosity concept, equation 4-2 can be simplified to

$$\frac{\partial\langle\bar{u}\rangle}{\partial t}=\frac{1}{\phi}\frac{\partial}{\partial z}\left[\phi(\nu_m+\nu_t)\frac{\partial\langle\bar{u}\rangle}{\partial z}\right]+g_x-\frac{1}{\rho}\frac{F_x}{\phi} \tag{4-7}$$

where ν_m = kinematic molecular viscosity; ν_t = kinematic eddy viscosity. The eddy viscosity ν_t is specified by the Spalart-Allmaras (S-A) turbulence model. Since the formulation of this model has been detailed introduced in Chapter 3, it will not included herein for simplicity.

In the modelling of open-channel flows, the turbulence length scale L is a crucial parameter for turbulence models under mixing length hypothesis which demand damping terms to correct the near-wall behavior. By using modified S-A model to simulate rough wall boundary layers, Lee and Paynter (1996) shifted the distance d by

the value R $(=0.9(\nu/u*)\left[\sqrt{k_s^+}-k_s^+\exp\left(-k_s^+/6\right)\right])$ toward the wall and calculated the eddy viscosity based on the effective distance from wall L_{eff} ($L_{\text{eff}} = L + R$). Aupoix and Spalart (2003) suggested the offset $R = \exp(-8.5\kappa)k_s \approx 0.03k_s$. The modification to the S-A model increased the eddy viscosity close to the rough wall. The corresponding effect can be considered as a shift of the near-wall velocity profile towards the wall leading to an increase of the skin friction. These modified S-A models performed well in simulations of open-channel flows over small roughness elements, such as sand grain paper and wire meshes (Aupoix and Spalart 2003). However, its implementation into natural rivers with large roughness elements (e.g. gravels and pebble clusters) has not yet been reported.

For flow over smooth surface, close to the wall the turbulence length scale is proportional to the distance between the point of interest and the solid wall and the vertical profile of the longitudinal velocity follows the logarithmic-linear relationship (the logarithmic layer). For flow over rough surface, in additional to the logarithmic layer, a roughness layer exists in which the flow is significantly affected by the roughness elements. Just above the crests of the roughness elements flow separation occurs and vortices are formed and washed downstream. The coherent structures exist as the roughness elements tend to block the large boundary-layer eddies. The roughness elements resist the flow and produce a form drag, as well as wake turbulences behind the elements. A range of turbulence length scales exists and the energy dominant turbulence eddies have a length scale proportional to the roughness element size. In the turbulence model the turbulence length scale thus is required to be modified to reflect these processes.

In the present study the gravel induced turbulence is simulated by using the S-A model. A modification of the effective wall distance (a turbulence length scale), L_{eff}, is made in accordance with the roughness length scale k_s. The turbulence length scale L_{eff} is assumed constant within the interfacial sublayer and remains unchanged (equal to the vertical distance between the point of interest and the zero reference level) in the rest of the flow region (as shown in Figure 4.2). The interfacial sublayer is taken to be the thickness of the gravel layer between the crest of the roughness elements and the zero reference level, which is around $0.5d_{50}$. This modelling option is called the modified wall distance model (MWD). The expressions for the effective distance are listed below:

$$\begin{aligned} L_{eff} &= z && \text{when } z < \alpha d_0 \\ L_{eff} &= c_r \times d_0 && \text{when } z < d_0 \\ L_{eff} &= z && \text{when } z > d_0 \end{aligned} \qquad (4\text{-}8)$$

where α is a parameter controlling the thickness of the boundary layer adjacent to the bed, taken to be within the range of 0.05 to 0.1; d_0 is the thickness of the interfacial sublayer; c_r is a parameter that controls the velocity distribution in the interfacial sublayer. For comparison, the original model with $L = z$ is also included and called the standard wall distance model (SWD). The schematic diagrams of the SWD and MWD are shown in Figure 4.3 and Figure 4.4, respectively.

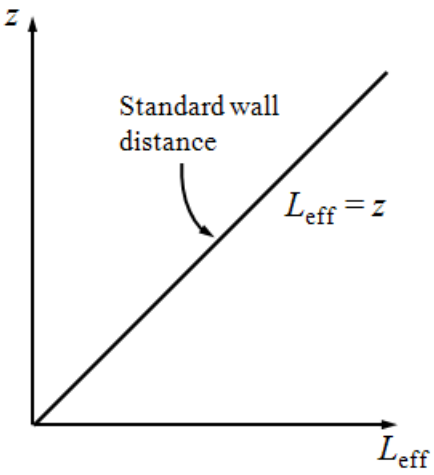

Figure 4.3. Original standard wall distance model (SWD)

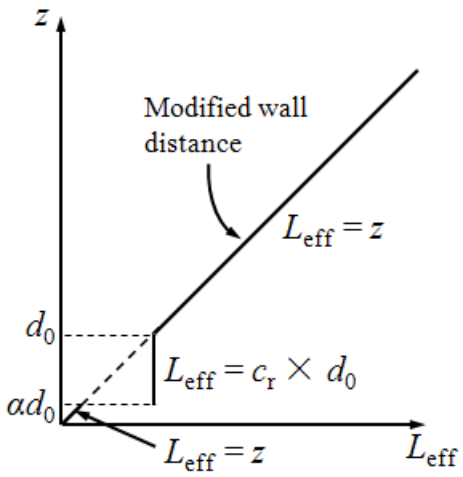

Figure 4.4. Modified wall distance model (MWD).

The wall function approach (WFA) is traditionally employed to model rough-bed induced resistance. The law of the wall (log-law) is assumed valid in the inner region for the small-scale roughness condition, which can be described by the following equation:

$$\frac{\langle \bar{u} \rangle}{u*} = \frac{1}{\kappa} \ln\left(\frac{z}{k_s}\right) + Br \tag{4-9}$$

where $\langle \bar{u} \rangle (z)$ is the DA streamwise velocity at a distance z measured from the reference level; $u*$ is the bed-shear velocity; κ is Karman constant (= 0.41 for small-scale roughness conditions); k_s is the equivalent (Nikuradse) sand roughness and is often chosen as the roughness length scale to quantify the roughness effects; $Br \sim 8.5$ is a numerical constant of which the exact value depends on the nature of the wall surface. Numerically it is a semi-slip boundary condition in which the wall boundary shear stress determined by Equation 4-9 is equated to the viscous shear stress at the wall.

However, the WFA is not entirely satisfactory in the numerical modelling of the gravel-induced roughness effect. It assumes the vertical profile of the longitudinal velocity profile follows the logarithmic-linear relationship and the turbulence length scale is proportional to the distance of the point of interest to the impermeable solid wall. For flows over gravels the velocity profiles do not follow the logarithmic-linear relationship and the assumption used by WFA thus is not valid. The results is that the empirical coefficient k_s and Br will not be constant (Kironoto and Graf 1994). Gaudio *et al.* (2010) suggested that κ is not universal in flows with either a low relative submergence (S_r) or with bed-load and suspended-load transport. Also the value of k_s can be large, which generates unrealistic negative velocity in the near-wall region. From Equation 4-9 it can be observed that the velocity becomes negative at $z < 0.03k_s$ for $Br = 8.5$. To avoid the generation of the negative velocity a coarse grid can be used but then the numerical solution will be sensitive to the point above the surface where the wall function is applied.

In DFM, the modelling of resistance force induced by a gravel bed is based on the quadratic friction law. The average force per unit volume within the drag force layer can be obtained by:

$$\frac{F_x}{\phi} = \frac{1}{2\phi}\rho C_d C_s b_s N \langle \overline{u}_1 \rangle^2 = \frac{1}{2\phi}\rho f_{rk} \langle \overline{u}_1 \rangle^2 \tag{4-10}$$

Therefore,

$$f_{rk} = C_d C_s b_s N \tag{4-11}$$

where N = number density (number of gravels per unit area, in $1/m^2$); b_s = effective projected width of the roughness element; C_d = drag coefficient corresponding to a single roughness element; C_s = shielding factor arising from the other roughness

elements in proximity; f_{rk} = drag force parameter reflecting the effects of shape, size and density of the roughness elements and the size of the wake generated by the flow conditions; $\langle \bar{u}_1 \rangle$ = resultant DA velocity within the roughness layer. The thickness of the region in which F_x is introduced is set equal to h_1 (see Figure 4.1 and Figure 4.2). The composite term C_dC_s is commonly defined as the bulk drag coefficient. The value of C_dC_s for spheres is approximately constant and equal to 0.45 in the Reynolds number range of 10^3 to 10^5 (Coleman 1967). In fact some previous works (e.g. Wiberg and Smith, 1991; Carney et al., 2006) have not addressed these factors.

The central finite difference scheme in space and forward difference in time is used to generate a system of algebraic equations to approximate the governing equations. The solution of the algebraic equations gives an approximate solution of the governing equations. To reduce the discretization error due to the difference between the exact solution of the governing equations and the exact solution of the system of algebraic equations obtained by the discretization process, a grid refinement study is carried out in the following section.

4.3. Case studies

4.3.1. Open-channel flow over small-scale roughness elements

Generally d_{50} is used as the roughness length scale k_s. In the range $D/d_{50} > 10$, the roughness element is commonly classified to be of small-scale. The velocity profiles of the flows follow the logarithmic linear relationship. To assess the performance of various methods to deal with the gravel induced resistance, including WFA, DFM

with SWD option and DFM with MWD option, for this case, the experiments carried out by Kironoto and Graf (1994) are numerically replicated. The experiments were performed in a tilting flume with bed surface covered densely by quasi-uniform gravels. The width of the flume was 0.6 m. The thickness of the gravel bed was about 0.10 m. The median and standard deviation values of the gravels are d_{50} = 23 ± 1.25 mm. Table 4.1 lists the flow parameters for the case chosen. The dimensionless roughness height $k_s^+ (= k_s \cdot u*/\nu) > 70$, which indicates the flow regime is fully rough.

Table 4.1. Summary of parameters for flow over small roughness elements

S_0	Q [l/s]	D [m]	k_s [m]	D/d_{50}	Fr	Re	$u*$ (cm/s)	k_s^+
0.00025	69.6	0.29	0.023	12.61	0.23	4.7×10^5	3.2	733.7

The computational domain extends from the reference level to the water surface (see Figure 4.1). The reference level is the level where the mean velocity is assumed to be zero, which is also the zero level (z = 0, where $z = z' - h_0$) used in the model. The drag force is then added in the roughness layer (from the reference level to the visual bed level) with the thickness equal to h_1 to represent the resistance effect induced by gravels. A rectilinear grid with refinement at the near wall region is employed. In order to evaluate the sensitivity of these two methods to mesh resolution, three meshes with 61, 31 and 21 grid cells were used in the simulation under the same flow condition. The simulations using WFA with the same meshes are also performed for comparison. In these simulations f_{rk} = 25 m^{-1} in DFM and B_r = 9 in WFA The value of f_{rk} = 25 m^{-1} is consistent with Equation 4-9 with $C_d \sim 0.45$, $N \sim 1/k_s^2$ = 1890 m^{-2}, and $b_s \sim 0.75k_s$.

The equivalence between WFA and DFM can be explained by the following analysis. If the shear stress is reduced from the value of the bed shear stress u^* at the crest level of the roughness elements to zero at the zero-reference level, based on Equations 4-9 and 4-10 the bed shear stress can be given by

$$u^* = \frac{\bar{u}(h_1)}{\frac{1}{\kappa}\ln\left(\frac{h_1}{k_s}\right) + Br} \sim \sqrt{\frac{f_{rk}h_1}{2}}\bar{u}_1 \tag{4-12}$$

So there is a relationship among f_{rk}, h_1 and k_s. In the present case the above equation approximately holds for $f_{rk} \sim 25\ \text{m}^{-1}$, $k_s = 0.023$ m and $h_1 \sim 0.2k_s$, if $\bar{u}(h_1) \sim \bar{u}_1$.

Figure 4.5 shows the computed results using the two methods. In this figure and the subsequent figures (Figure 4.6 and Figure 4.7) DFM1, DFM2 and DFM3 denote the computed results using DFM with grid number n = 61, 31 and 21 respectively. Similarly, WFA1, WFA2 and WFA3 denote the computed results using WFA with grid number n = 61, 31 and 21. With the finest mesh (n = 61) the computed velocity profiles using these two methods are indistinguishable from each other. They also fit perfectly with the experimental data in the logarithmic inner region. An apparent discrepancy occurs in the near-water-surface region where the measured maximum velocity occurred beneath the water surface. This is the typical 'velocity dip phenomenon' which is due to the side-wall induced secondary current effect.

In Figure 4.6 and Figure 4.7 it can be seen that the decrease of grid number has no significant impact on the accuracy of these two methods in the inner region. No visible difference can be identified for the reduction of grid cells by 66%. However, the decrease in grid number leads to a smaller velocity in the near-water-surface region.

This is attributed to the numerical dissipation error since the number of the grid cells has been substantially reduced in the near-water-surface region. Comparatively speaking, the numerical error resulting from the reduction in grid number is smaller for DFM. The velocities in the near-water-surface region computed by DFM3 differ by less than 2.7% from those of of DFM1, while the largest discrepancy of the computed velocities from WFA3 and WFA1 is 5.33%. It appears that DFM is less sensitive to grid refinement as compared to WFA, mainly because the drag force is imposed to a flow region rather than at the boundary.

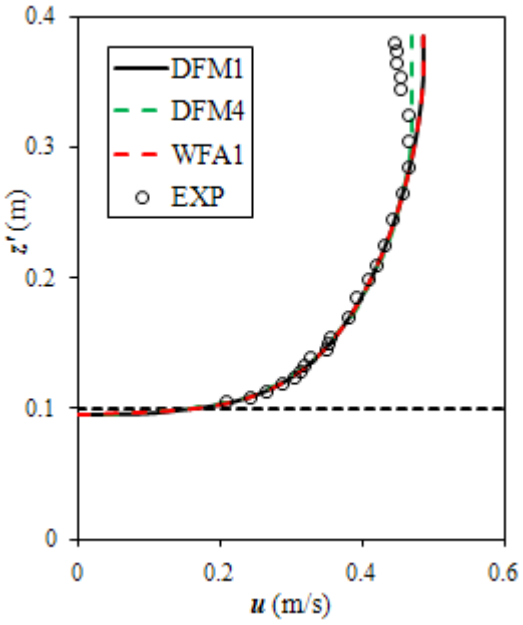

Figure 4.5. Measured and calculated velocity profiles for flow over small-scale roughness elements

(The horizontal dash line denotes the upper level of the roughness layer; Grid number = 61; DFM1 and WFA1 – without secondary current, DFM4 – with secondary current)

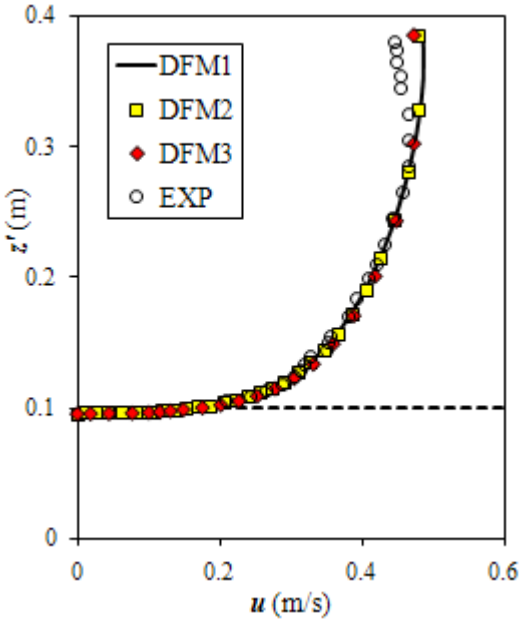

Figure 4.6. Grid convergence test of DFM

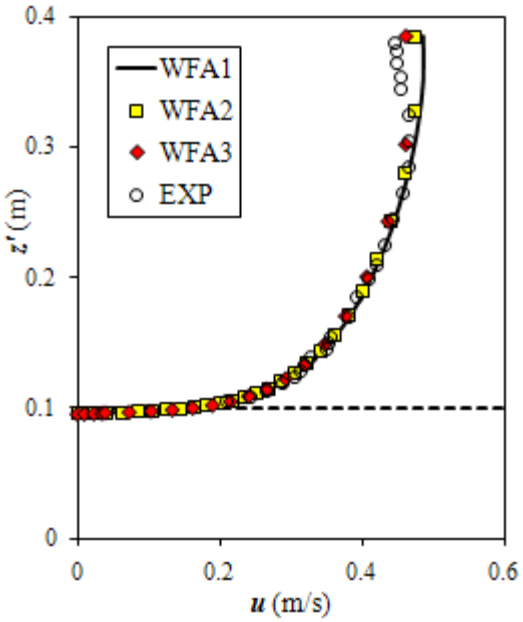

Figure 4.7. Grid convergence test of WFA

Figure 4.8 shows the normalized Reynolds stress profiles. It can be seen that the measured Reynolds stress reduced linearly from the bottom to zero at z = δ where velocity reaches the maximum value. This is a consequence of the sidewall-induced secondary current and the associated anisotropic turbulence. The Reynolds stress follows the linear distribution which is also plotted in Figure 4.8, viz.,

$$\frac{-\overline{u'w'}}{u_*^2} = 1 - \frac{z}{\delta} \tag{4-13}$$

The computed profiles of Reynolds stress for all the three methods (WFA, DFM with SWD, DFM with MWD) collapse on the same line which is denoted by DFM1 in Figure 4.8. The profile is in acceptable agreement with measured data. As the secondary current effect is not accounted for in the numerical models, the surface dip phenomenon cannot be predicted. Figure 4.9 compares the computed and measured

eddy viscosity profiles. Again the computed eddy viscosity profiles for all the three methods (WFA, DFM with SWD, DFM with MWD) collapse on the same line which is denoted by DFM1 in Figure 4.9. The computed eddy viscosity profile is in reasonable agreement with the measured data in magnitude and trend.

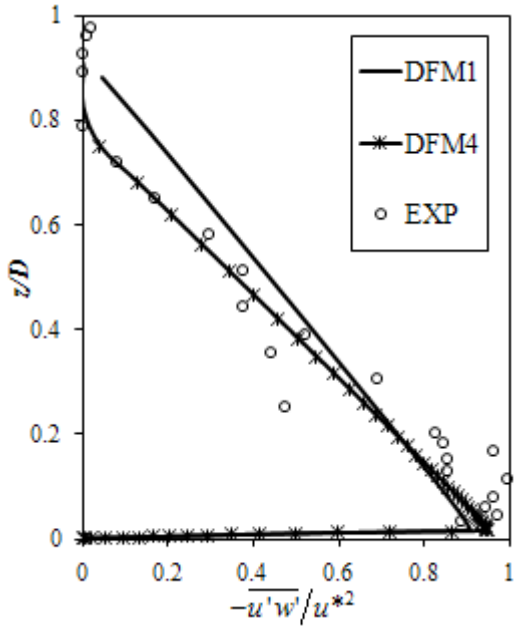

Figure 4.8. Normalized Reynolds stress profiles for flow over small-scale roughness elements

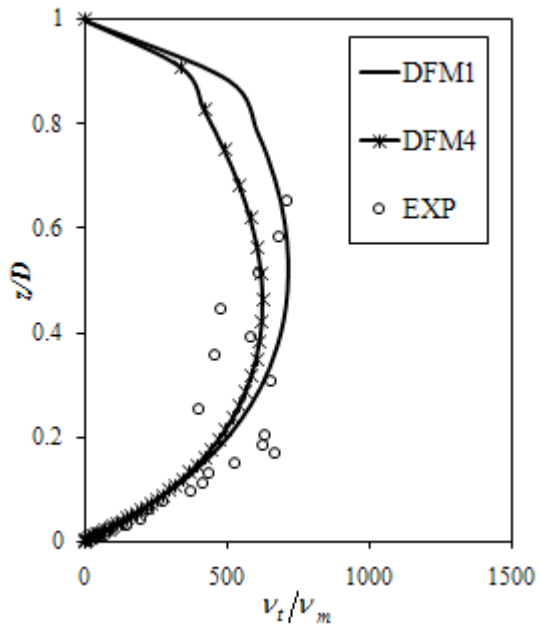

Figure 4.9. Normalized eddy viscosity profiles for flow over small-scale roughness elements

In using the MWD option, the turbulence length scale L and hence the viscous force within the interfacial sublayer increase as compared to those in the SWD option. The resultant DA velocity within the interfacial sublayer $\langle \bar{u}_1 \rangle$ is then reduced and a larger value of $f_{rk}h_1$ is required to balance the shear stress u^* (Equation 4-12). Assuming a constant value of f_{rk}, the interfacial layer h_1 varies with c_r and the results are shown in Table 4.2. It can be seen that the range of h_1 is $0.2k_s$ - $0.37k_s$, which falls

within the experimentally determined range. The computed velocity and Reynolds stress profiles are indistinguishable from the corresponding profiles computed by using the SWD option. Thus both the MWD and SWD options are applicable for this problem, providing the total shear stress at the crest of the roughness elements can be simulated accurately.

Table 4.2. Model parameters for SWD and MWD (grid number = 61, f_{rk} = 25 m^{-1})

Model option	c_r	h_1/k_s	Computed mean velocity (m/s)
SWD	—	0.2	0.415
MWD	0.3	0.26	0.415
MWD	0.15	0.34	0.409

Further improvement in the prediction can be achieved by noting that the secondary current produces an approximate balance of the forces in the near-water-surface region. In the simulation the body force density g_x can be set to zero in this region. Figure 4.5 and Figure 4.8 (curves DFM4) show that marked improvement in the velocity profile and Reynolds stress at the near-water-surface can be obtained. The balance of the body force and the secondary current induced force there generates a constant velocity and a zero Reynolds stress, which are in better agreement with the measured data. The eddy viscosity is smaller (Figure 4.9) mainly because the secondary current dissipates part of the flow energy.

4.3.2. Open-channel flow over large-scale roughness elements

4.3.2.1. Open-channel flow over spherical segment-type roughness element

In the range $10 > D/d_{50} > 1$, the roughness element is commonly classified to be of large-scale. In this section, laboratory measured data of open-channel flows over two different kinds of widely-spaced, large-scale roughness elements were used to test the performance of the DANS model. The first data set was collected from the case of regular spherical segment-type roughness, and the second data set was collected from the natural-setting case with irregular pebble clusters.

The experiments of open-channel flows over spherical segments (diameter d = 63.8 mm, roughness height Δ = 21 mm) were performed by Nikora *et al*. (2001). The elements were arranged in a regular staggered configuration. The relative distances between two adjacent elements in the streamwise and spanwise direction were 114 mm and 66.5 mm respectively. The experimental data were collected at two different flow rates, Q = 48.9 l/s (case 1) and Q = 92.0 l/s (case 2) (see Table 4.3). Based on the DA (time and space averaged) velocity data, Nikora *et al*. (2001) found that the form-induced sublayer did not exist and the flow region only consisted of the outer layer, the logarithmic layer and the interfacial sublayer. The empirical equations obtained for the latter two layers are as follows:

$$\frac{\langle \bar{u} \rangle}{u*} = \frac{1}{\kappa}\left(\frac{z}{d_0}\right) + C \qquad \text{within logarithmic layer} \qquad (4\text{-}14)$$

$$\frac{\langle \bar{u} \rangle}{u*} = C\frac{z}{d_0} \qquad \text{within interfacial sublayer} \qquad (4\text{-}15)$$

where $\langle \overline{u} \rangle$ is the DA streamwise velocity component; d_0 is the thickness of the interfacial sublayer; C is a parameter of velocity distribution ($= \langle \overline{u} \rangle d_0 / u^*$) and was determined to be 7.1 experimentally.

Table 4.3. Flow parameters for the simulations (experiments by Nikora, *et al*., 2001)

Case	Q [l/s]	S_0	D [cm]	D/d_0	u^* [cm/s]	Re^+ ($= u^* k_s / \nu$)
1	48.9	0.0032	13.5	6.4	6.5	1,365
2	92.0	0.0031	18.2	8.7	7.7	1,617

In the simulations, the mesh with grid number = 61 used in the previous section was employed. In the presentation of the experimental data the subsurface layer thickness has already been deducted. The reference level is taken at $z = z' = 0$. The drag force was added in the interfacial sublayer with the thickness $d_0 = \Delta = 2.1$ cm. The MWD option is used with $f_{rk} = 3.8\ \mathrm{m}^{-1}$, which is consistent with the calculation using $b_s = d$ (= 0.0638 m), $N = 1/(0.114 \times 0.0665) = 132\ \mathrm{m}^{-2}$, $C_d C_s = 0.45$ (suggested by Coleman (1967)). The value of c_r is set to 0.3. Table 4.3 summarizes these two experimental conditions used for comparison in the numerical study. For comparison, computer simulations using other model options have also been carried out. Details of the computer runs are tabulated in Table 4.4.

Figure 4.10 shows the computed velocity profiles as well as Equations 4-14 and 4-15 with $\kappa = 0.41$ and $C = 7.1$. The computed velocity profiles match the measured mean velocity profiles in both the interfacial sublayer and the logarithmic layer. This show that the DFM with MWD option is capable of yielding velocity profiles which are linear in the interfacial sublayer and logarithmic in the logarithmic layer.

The advantage of using the DFM with MWD option is demonstrated by comparing the results with those using the DFM with SWD option and the WFA option. For the DFM with SWD option, by neglecting the change in the turbulence structure within the interfacial sublayer, the linear velocity profile within the sublayer cannot be produced, and the whole flow region becomes the logarithmic region. Also, to match the measured velocities, the value of f_{rk} has to be reduced slightly to 1.9 m^{-1}(Figure 4.4). For the WFA option, the value of k_s is large and unrealistic negative velocities occur at the near-wall region. Also the linear velocity variation within the interfacial sublayer cannot be reproduced since the WFA option assumes the velocity follows the logarithmic-linear relationship.

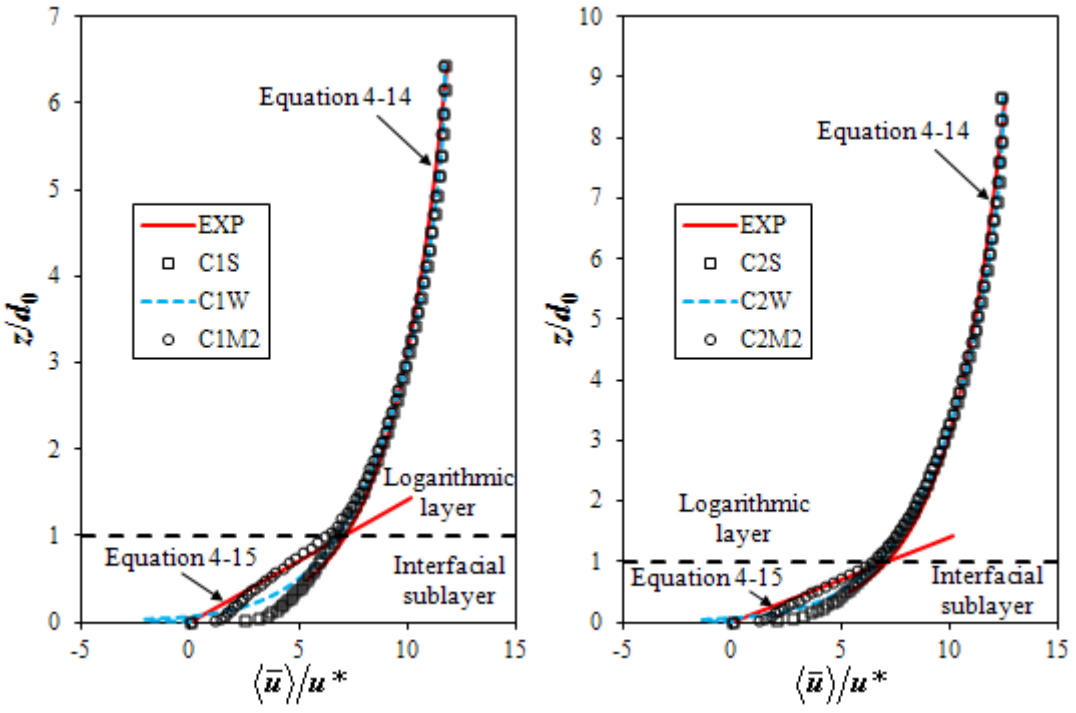

Case 1 in Table 4.3 Case 2 in Table 4.3

Figure 4.10. Normalized velocity profiles for flows over spherical segment-type bed, runs C1S, C1W, C1M2, C2S, C2W, C2M2 are defined in Table 4.4 (experiments by Nikora *et al*., 2001; the dash line denotes the upper level of the interfacial sublayer)

Table 4.4. Computational parameters used in the simulations (experiments by Nikora *et al*., 2001)

Case	Run	Model option	c_r	f_{rk} [m^{-1}]	C_dC_s
1	C1S	DFM-SWD	—	1.9	0.23
	C1W	WFA-SWD	—	—	—
	C1M1	DFM-MWD	0.15	7.3	0.87
	C1M2	DFM-MWD	0.3	3.8	0.45
	C1M3	DFM-MWD	0.5	2.3	0.27
2	C2S	DFM-SWD	—	1.9	0.23
	C2W	WFA-SWD	—	—	—
	C2M1	DFM-MWD	0.15	7.3	0.87
	C2M2	DFM-MWD	0.3	3.8	0.45
	C2M3	DFM-MWD	0.5	2.1	0.25

The computed vertical profile of the Reynolds shear stress (Figure 4.11) exhibits a linear variation with zero value at the free surface and the maximum at the crest level of the roughness elements, and then decreases towards the trough level of the roughness elements. The increase in Reynolds shear stress with the decrease of the elevation is caused by the balance between the longitudinal gravitational force component and the Reynolds shear force. The decrease in the Reynolds shear stress within the roughness element layer is due to the existence of the drag force which counteracts partly the gravitational force component. This typical variation of the Reynolds shear stress has been confirmed experimentally (Manes *et al.* 2009).

The sensitivity of the solution to the parameter c_r was further investigated. The value of c_r is expected to vary within the range 0.1 to 0.5. The computations show that the resulting velocity profile can match the measured profile very well by adjusting the value of f_{rk} which is not exactly known. h_1 is kept constant in this case since its value

is comparatively large and a significant change is not justified. A smaller value of c_r requires a larger value of f_{rk} to produce a constant total resistance to the flow (Table 4.4). However, it is noteworthy that the value of f_{rk} remains nearly constant for different flow conditions (Case 1 and Case 2) with the same c_r.

Figure 4.11 also shows the corresponding computed Reynolds stress profiles for different values of c_r. It can be observed that the Reynolds stress variation within the interfacial sublayer is sensitive to the parameter set (c_r, f_{rk}) used. A smaller value of c_r leads to a smaller Reynolds stress within the interfacial sublayer. Previous studies have revealed that the shear stress is mainly composed of the Reynolds stress and the form-induced stress within the interfacial sublayer. Because the form-induced stress is dependent on the bed forms, the Reynolds stress would be affected accordingly. It is, therefore, inappropriate to use the standard S-A model for cases with large-scale roughness as the standard version is designed for smooth beds. With the MWD option, apart from yielding the quasi-linear distribution of the mean velocity, the DFM can also control the magnitude of the Reynolds stress within the roughness layer by adjusting the value of c_r.

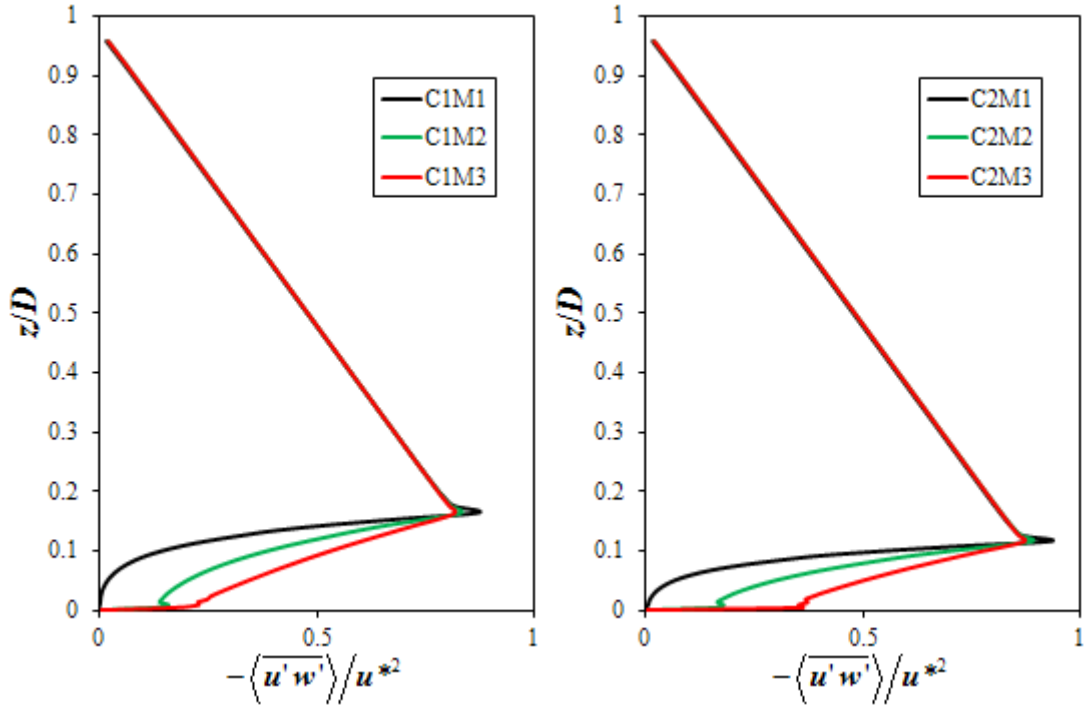

Case 1 in Table 4.3 Case 2 in Table 4.3

Figure 4.11. Normalized Reynolds stress profiles for flows over spherical segment-type bed (experiments by Nikora *et al*., 2001)

4.3.2.2. Open-channel flow over sparely distributed pebble clusters

This model is subsequently applied in a natural setting: an open-channel flow over a plane bed of real gravels including large, sparely distributed pebble clusters. The laboratory experiments were carried out by Lawless and Robert (2001a; 2001b). The bed roughness elements consisted of a mixture of two components: the ground components with d_{50} = 12.4 mm and manually developed pebble clusters. Seven pebble clusters were arranged in a staggered pattern on the top of the ground layer (as shown in Figure 4.12). The total area examined for the experiments was 0.96 m^2 (1.6 m long, 0.6 m wide). The average dimensions of the pebble clusters were 0.262

m in length, 0.085 m in width. The maximum bed form height is 5.9 cm and the mean bed elevation is 3.06 cm. Velocity measurements were collected in a series of vertical profiles spaced at 0.1 m intervals along the channel under steady flow conditions with an acoustic Doppler velocimeter (ADV). In the present study totally 18 vertical profiles (shown as the filled circles in Figure 4.12) were chosen for the computation of a statistically representative DA flow field. Two flow conditions with identical flow rate and different water depths were selected for model test. The water depths were 0.137 m and 0.275 m for the shallow flow condition (Case 1) and deep flow condition (Case 2), respectively. The corresponding relative submergence (D/d_0) were 4.5 and 9. To be consistent with the experiments (Lawless and Robert 2001a; Lawless and Robert 2001b), the reference level is taken at the top of the ground layer due to the apparent difference in size between the ground components and the pebble clusters. Figure 4.13 shows the variation of the porosity ϕ with the dimensionless height z/Δ. It can be seen that ϕ equals to 0.8 at the top of the ground layer and increases linearly to 1 at the top of the roughness layer.

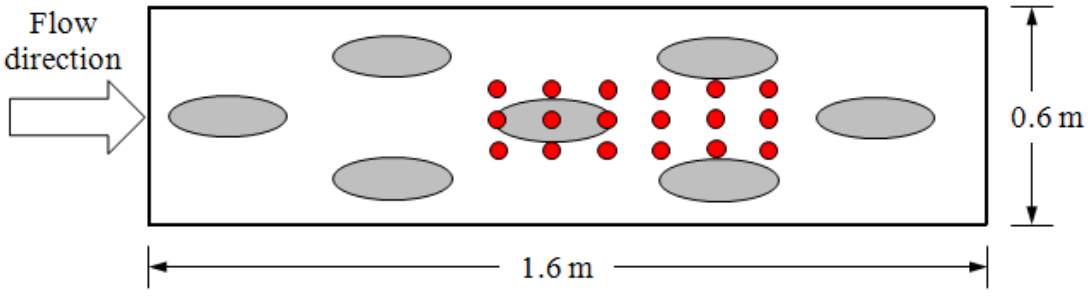

Figure 4.12. Plan view of the roughness arrangement and the location of position of spatially-averaged verticals (experiments by Lawless and Robert, 2001a & 2001b)

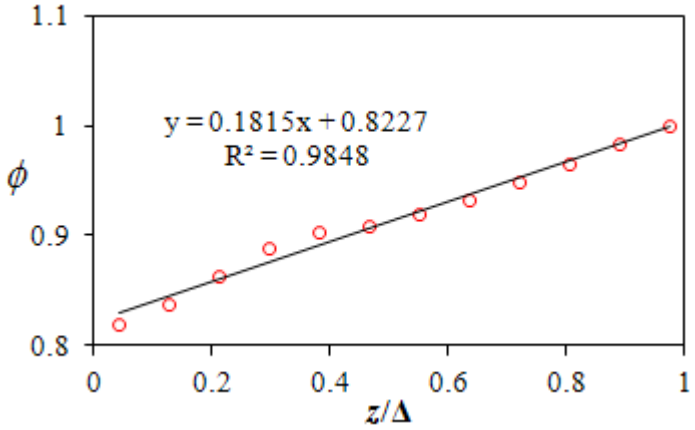

Figure 4.13. Variation of porosity with the z/Δ

The finest grid adapted in the previous section (n = 61) was also used herein. The drag force was introduced in the interfacial sublayer with the thickness d_0 = 3.06 cm. The numerical simulations were also performed using DFM with SWD and MWD options. The parameters used in the simulations are listed in Table 4.5. The bulk drag coefficient C_dC_s can be obtained in accordance with Equation 4-11 with b_s = 0.085 m, N ≈ 7 m^{-2}. It can be seen from this table that the MWD option leads to more consistent parameterization of the bulk drag coefficient (C_dC_s = 0.77), which also fall within the suggested range (0.6 ~ 0.8) for the DANS modeling by Rameshwaran *et al.* (2011), for shallow and deep flow conditions.

Table 4.5. Computational parameters used in the DANS modelling (experiments by Lawless and Robert, 2001a & 2001b)

Case	D/d_0	Model option	c_r	f_{rk} [m^{-1}]	C_dC_s
1	4.5	DFM-SWD	—	0.34	0.54
		DFM-MWD	0.3	0.46	0.77
2	9	DFM-SWD	—	0.29	0.49
		DFM-MWD	0.3	0.46	0.77

Figure 4.14 shows the comparisons between the predicted and the average measured vertical velocity profile, along with the standard deviation of the flume measurements (horizontal bars for the data points) for both Case 1 and Case 2. It can be seen from the DA experimental data that for Case 1 with smaller relative submergence (D/d_0 = 4.5), a velocity inflection occurred and an S-shape profile was formed. The average measured velocity profile appears to be linearly distributed within the interfacial sublayer. For Case 2 with larger relative submergence (D/d_0 = 9), however, the average measured velocity distribution was logarithmic. The standard deviations shown in Figure 4.14 also indicate that the measured velocities within the interfacial sublayer are more scattered than those in the outer flow region for these two cases. The predicted profile of the spatially-averaged mean velocity for the RANS model with high-resolution topography (Rameshwaran *et al.* 2011) are also plotted for Case 1. It can be seen that for the shallow flow condition (Case 1), the DANS model with SWD option, which perform equally well with the high-resolution RANS model, under-predicted the mean velocities above the interfacial sublayer and over-predicted the mean velocities within the interfacial sublayer. On the contrary, the simulated velocity profile with the MWD option shows excellent agreement with the average measured profile. Although all the predicted values fall within the standard deviation of the measured values, the DANS model with MWD option faithfully reproduced the quasi-linear variation of the mean velocity within the interfacial sublayer. For the deep flow condition (Case 2), it can be seen from Figure 4.14 that the computed velocity profile with SWD option fit well with the logarithmic profile. In the region above the interfacial sublayer the computed velocities with MWD option were slightly higher than that with SWD option but still in good agreement with the experimental measurements. Within the

interfacial sublayer, the agreements between the numerical prediction and the experimental measurements were satisfactory by using both the SWD and MWD options.

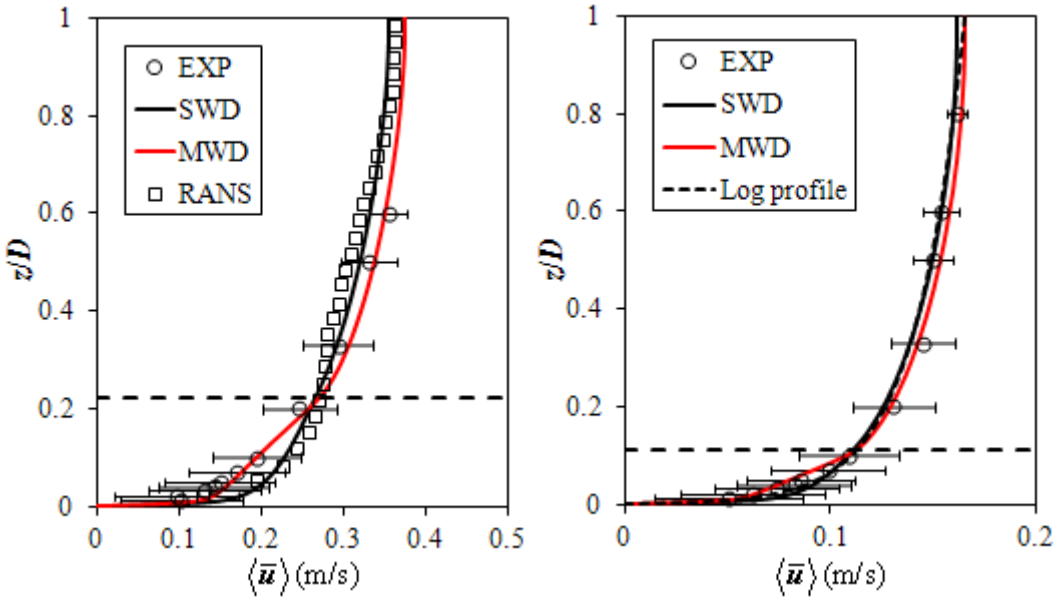

Case 1 in Table 4.5 Case 2 in Table 4.5

Figure 4.14. Vertical velocity profiles for flows over large and widely-spaced pebble clusters (experiments by Lawless and Robert, 2001a & 2001b; the horizontal dash line denotes the upper level of the interfacial sublayer)

4.3.3. Steep-slope gravel-bed river flow

The model is then applied to the field. The data for field verification of the model were collected by Marchand *et al*. (1984) in high-gradient, coarse-grained streams in Colorado. They measured velocity profiles from nine streams with depth sediment ratio ranging from D/d_{84} = 2.33 to 14.3. The reported water surface slope ranged from 0.002 to 0.029. For each stream, velocity profiles were collected at 3 or 4 locations

along the centerline with 8-10 points between the bed and water surface. At each location, velocity profiles were measured at several flow stages. Due to the heterogeneity in local bed geometries for different locations, the measured velocity profiles show some degree of variability. Hence the field data used herein for comparison have been processed through spatial averaging. The characteristic parameters for these three streams are summarized in Table 4.6.

Table 4.6. Characteristic parameters and average velocities for three simulations of river flows

	Case 1	Case 2	Case 3
Parameters	Clear Creek at Golden	Blue River near Dillon	Lake Creek
Bed slope	0.006	0.013	0.029
d_{50} (cm)	4.5	4.9	11.9
d_{84} (cm)	10.08	10.71	23.76
D (cm)	112	63	88
Range of U measured by Marchand et al. (1984) (cm/s)	193-250	161-213	140-285
U computed by Carney et al. (2006) (cm/s)	200	191	285
U for simulation with SWD model (cm/s)	214	188	261
U for simulation with MWD model (cm/s)	217	190	263

For the computational details, the reference level is taken to be the bed level measured by Marchand *et al.* (1984), which is approximately $0.5d_{50}$ higher than the actual channel bed ($h_0 = 0.5d_{50}$). For MWD, the thickness of the interfacial sublayer is taken as the other half of the median diameter ($d_0 = d_{50} - h_0 = 0.5d_{50}$) and $c_r = 0.15$. The rectilinear mesh with grid number $n = 61$ is still used. The value of f_{rk} is determined from Equation 4-9 and is equal to 4.4 m^{-1}, 4.2 m^{-1} and 1.9 m^{-1} for Clear Creek, Blue River and Lake Creek, respectively. Computed average velocities are listed in Table 4.6. All the computed values with both the SWD option and the MWD option fall within the range of measured mean velocities. The two set of results are very close with the results from the SWD option marginally smaller than those from the MWD option.

Figure 4.15 shows the computed velocity profiles with the SWD option and the MWD option, the range of spatially averaged data collected by Marchand *et al.* (1984), and computed profiles from Carney *et al*. (2006). It can be seen that most of the computed velocities fall within the range of the field measurements. Both the computed and measured velocity profiles do not follow the logarithmic linear relationship (Figure 4.15). In the last case (Lake Creek) in which $D/d_{84} = 3.7$, the velocity profiles are approximately S-shape. Lake Creek has a bed slope greater than 1% and D/d_{84} value within the range of 1 to 4, meeting the conditions for the development of the S-shape velocity profile. Marked difference in velocities occurs near the water surface for cases 1 and 2. This is probably due to that in the field the flows were non-uniform and under the spatially decelerating condition. For the case of Lake Creek, the computed velocities fall on the boundaries of the measured velocity range. The computed velocity profile exhibits an apparent S-shape as compared to the measured

velocity profile.

The computed velocities using the RNG *k-ε* model due to Carney *et al*. (2006) are also included for comparison. The present model gives a slightly better prediction of the mean velocities as shown in Table 4.6. The present computed velocity profile is remarkably close to that in Carney *et al*. (2006) for the case of Clear Creek and better matches the field measured data for the case of Blue River. It also gives a more apparent S-shape profile for the case of Lake Creek. The slightly better performance of the present model is mainly due to that a different turbulence modelling strategy is used. In the RNG *k-ε* model the gravels are assumed to have no effect on the turbulence generation or dissipation rates (FLUENT 2005), therefore no modification to the equations has been made. It is expected that the RNG *k-ε* model is unable to reproduce the S-shape profile shown in Figure 4.15 (similar to the DFM with SWD option) and a higher order turbulence closure may not have benefit.

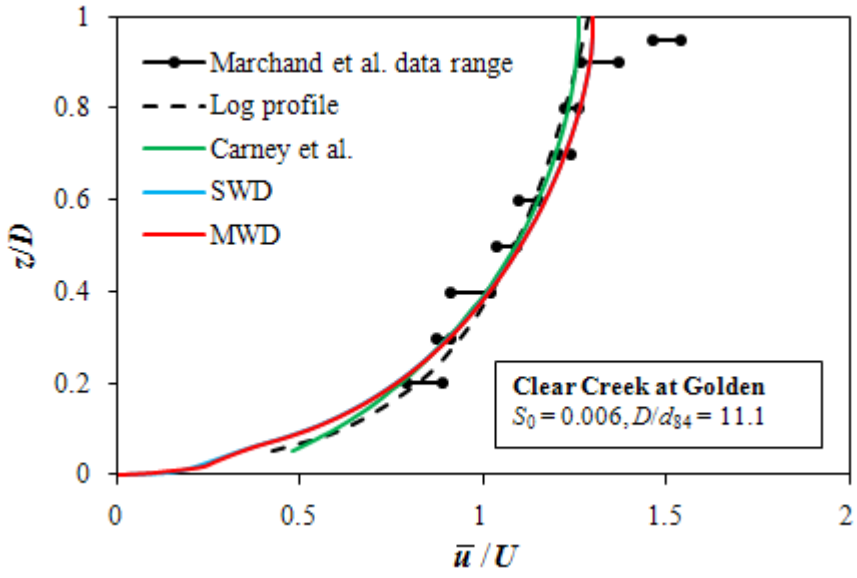

(a) Clear Creek at Golden

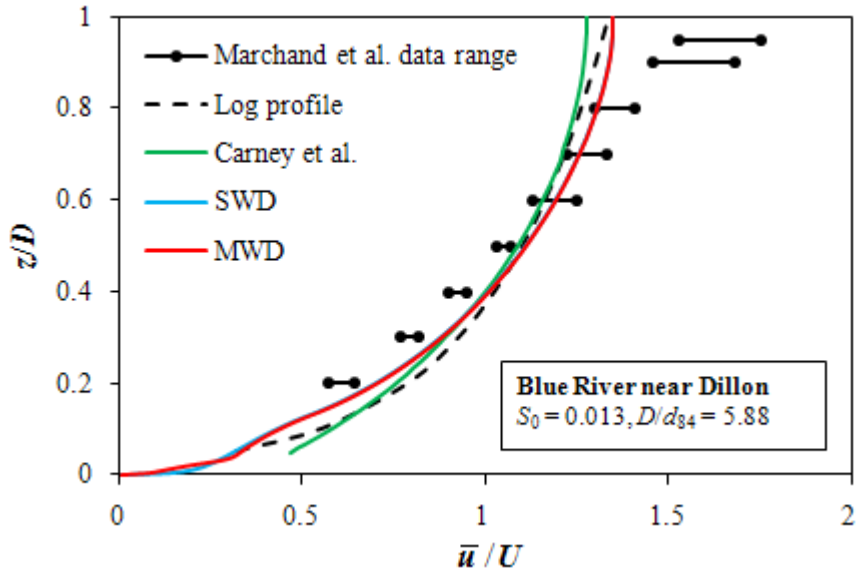

(b) Blue River near Dillon

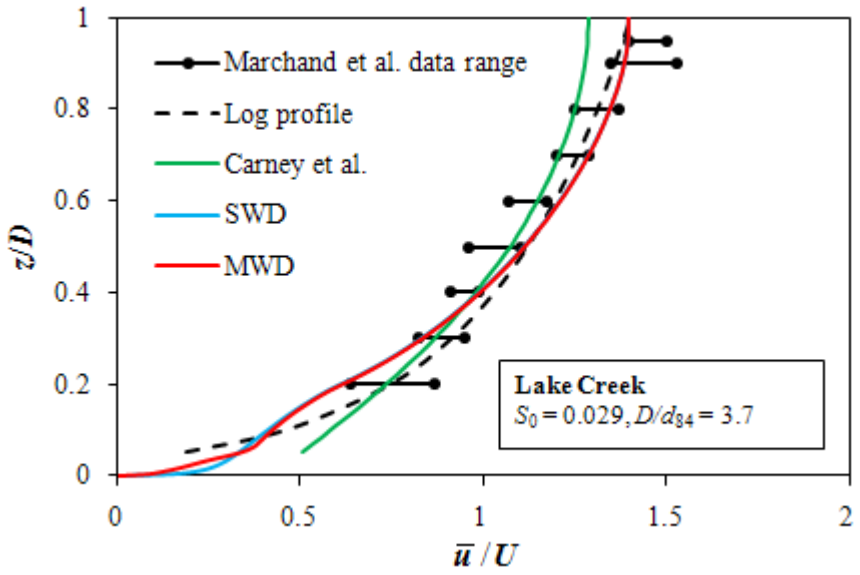

(c) Lake Creek

Figure 4.15. Velocity profiles for steep-slope gravel-bed rivers

4.4. Conclusions

A DANS model incorporating the drag force method (DFM) and a modified S-A turbulence closure has been developed for gravel-bed open-channel flows. Extensive tests show that the model can simulate accurately the velocity profiles in the interfacial sublayer, form-induced sublayer and logarithmic layer. Particularly, the S-shaped velocity profile for sparsely distributed large size roughness elements can be faithfully reproduced. The modification of the turbulence length scale within the interfacial sublayer increases the viscous force and reduces the drag force in balancing the gravitational force component. The model leads to a more consistent parameterization of the bulk drag coefficient (C_dC_s) and generates a quasi-linear velocity distribution within the interfacial sublayer. For practical applications, the drag force parameter f_{rk} can be obtained from the measurable parameters shown in Equation 4-11. The parameter for the turbulence length scale (c_r) was found to be able to control the magnitude of the Reynolds stress within the interfacial sublayer and the value of 0.3 is recommended from the case studies. Further improvement of the model can be done by seeking an accurate parameterization of the form-induced stress term.

Chapter 5.

Depth-limited Open-Channel Flow over Gravel Patch

5.1. Introduction

The mean flow and turbulence characteristics of open-channel flows over hydraulically smooth surfaces have been extensively studied in the last 20-30 years (Nezu and Nakagawa 1993). Progress was also achieved in understanding the mean flow and turbulence structure in flows over hydraulically rough beds with high relative submergence (Kirkgoz 1989; Kironoto and Graf 1994; Nikora and Smart 1997). Knowledge of mean velocity and turbulence characteristics of open-channel flow over gravel bed with small relative submergence (e.g., mountain streams and floodplain rivers) remains incomplete and needs to be further studied.

One of the main topics in the study of turbulent geophysical flows is the form of the streamwise velocity profile. In shallow gravel-bed rivers the mean velocity profiles, which are greatly affected by the macro-rough beds, have two kinds of shapes, i.e., logarithmic and S-shaped. As mentioned previously, the S-shaped velocity profile is a consequence of local protrusions and simultaneously exists with the logarithmic velocity profile in gravel-bed river flows (Franca and Lemmin 2009). Thus for most cases in gravel-bed open-channel flows, especially under the well-sorted condition,

the streamwise mean velocity might still follow the logarithmic distribution (Equation 2-7). However, due to the low relative submergence, the Karman constant κ appears to be non-universal (Rand 1953).

The Karman constant κ, which is defined as the ratio of the mixing-length to the vertical distance from the wall, is a crucial parameter to describe the time averaged streamwise velocity profile along the vertical axis in a wall-bounded shear flow based on the log-law. There have been many attempts to accurately determine κ for an idealized flow over a smooth wall or for homogeneous turbulence. Based on systematic velocity measurements with an LDA-system, Nezu and Rodi (1986) obtained a universal value for κ (= 0.412) for fully-developed open-channel flows over smooth beds. This value has been confirmed extensively in the subsequent experimental and numerical studies. On the contrary, the value of κ for rough-bed flows with low submergence still remains unclear. To the author's knowledge, Rand (1953) could be the first researcher to study the effect of relative submergence on κ. By performing laboratory experiments on an open-channel flow with artificial bottom roughness, he reported a value of κ = 0.3 for the open-channel flow with relative submergence S_r = 3.3. Dittrich and Koll (1997) experimentally demonstrated that κ is non-universal and dependent on both the bed roughness and S_r. Their experimental results indicated that the vertical velocity distributions can be described by the logarithmic relationship with modified κ values in the order of 0.18. In addition, they also claimed that the value of κ strongly depends on the chosen reference level. Koll (2006) also reported that κ is non-universal but depends on the irregularity of the bed roughness as well as the S_r. For regular surfaces and large relative submergences, κ approaches a value of 0.4. The κ-value decreases

significantly as the bed roughness becomes more irregular or the values of S_r decreases. Furthermore, he suggested that the κ-value reaches a mimimum within the range $4 < S_r < 7$ and increases again as S_r further decreases. Cooper (2008) also reported values of $\kappa < 0.41$ when $4 < S_r < 13$. Gaudio (2010) summarized the existing experimental data and suggested a non-monotonic dependency of κ on S_r: κ-value decreases as S_r increases if $S_r > 2$, reaches a minimum value of 0.27 at $S_r = 7.5$, and becomes universal for $S_r > 15$. Nevertheless, the cause of the non-monotonic dependency still remains unexplained.

In this study, a series of laboratory experiments were conducted to further investigate the mean velocity and turbulence intensity distribution, as well as the friction factor in gravel-bed open-channel flows with small relative submergence. Experiments were carried out in a laboratory flume instead of a natural channel due to the fact that it was feasible to control the flow properties, such as flow rate and water depth. Furthermore, homogeneous vegetation and gravel bed can be fabricated in the laboratory while there are more difficult to be constructed in the field. Based on the experimental results, a sensitivity analysis of the drag force parameter (f_{rk}) was also performed subsequently.

5.2. Experimental facilities

5.2.1. Tilting Flume

The laboratory experiments in this study were conducted in a 12.5 meter long, 0.31 meter wide, and 0.4 meter deep tilting flume which was manufactured by GUNT

Hamburge, Germany (Photo 5.1). Its longitudinal bed slope can be varied from -0.83% to 2%. The sidewalls and the bottom of the flume were made of glass and steel. A series of honeycomb grids were installed at the entrance of the channel to straighten the flow and prevent the formation of large-scale flow disturbances. The flume received a constant supply of water from a head tank and had an adjustable tailgate at the downstream end of the flume to regulate the flow depth. Water leaving the flume entered a large sump under the flume, where it was recirculated to the constant head tank with a pump. Two wheeled trolleys, which can be moved along the double-rail track on the top of the flume, were used to mount the point gauge and velocity measuring instruments (i.e., UVP and Vectrino ADV).

Photo 5.1. Tilting flume

5.2.2. Water depth and discharge measurements

A Vernier point gauge with ± 1mm accuracy was mounted on the mobile trolleys to measure the water depth. As shown in Photo 5.2, the water discharge rate was measured by a build-in electromagnetic flow meter (PROMAG type, made by Endress & Hauser) installed in the flow return pipe.

Photo 5.2. The build-in electromagnetic flow meter

5.2.3. Velocity measurement

Two types of velocity measuring instruments, namely ultrasonic velocity profiler (UVP) and Vectrino acoustic Doppler velocimeter (Vectrino ADV), were used in the flume experiments. Both instruments were operated in a non-intrusive way. The UVP is 1D and can record only one component of velocity along a line. The Vectrino ADV is 3D and can measure all three components of the velocity at a single point.

5.2.3.1. Ultrasonic Velocity Profiler (UVP)

The UVP system is manufactured by Met-Flow SA and consists of a specially made personal computer (PC) with a monitor (as shown in Photo 5.3), and a cylinder probe (60 mm long and 13 mm in diameter).

Photo 5.3. The UVP system

The probe generates a short emission of ultrasound (US) which travels along the measurement axis. When the US pulse hits moving particles, part of the US energy scatters by the particles and echoes back. The echo reaches the transducer after a time delay:

$$t = \frac{2x}{c} \tag{5-1}$$

where t = time delay between transmitted and received signal; x = distance of scattering particle from transducer; c = speed of sound in water. If the scattering particle is moving with non-zero velocity component along the beam axis, the received echo is Doppler-shifted so that:

$$\frac{V}{c} = \frac{f_d}{2 f_0} \tag{5-2}$$

where V = velocity component along the transducer axis (only one velocity component can be collected); f_d = Doppler shift (Hz); f_0 = transmitting frequency. UVP measures the time delay t and the Doppler shift f_d and then calculates both the position and velocity of a particle. The basic function of the UVP is the ability to measure instantaneous velocities at many spatial points (channels) along the measurement distance, permitting the calculation of both time- and space-averaged velocities.

In the present application, velocities were measured by means of a 2MHz Met-Flow UVP probe. The probe measures instantaneous velocities at 128 locations or bins within a length of about 9.5 cm. The sampling volume at each measurement point is shaped as a disk having ~ 10 mm diameter (the diameter increases at a rate imposed by the divergence of the beam, i.e., 2.2 degrees) and 0.74 mm thickness. The velocities measured at each point, represent the average velocity of the particles moving within the sampling volume.

The signals coming from the UVP probe are transferred to the PC in which the velocity data can be stored, analyzed and visualized. More details about the Met-Flow UVP system can be found in the UVP Monitor User Guide.

5.2.3.2. Vectrino ADV

As a new generation of 3D ADV, a Nortek AS Vectrono ADV (as shown in Photo 5.4) was used to measure the instantaneous velocity components in the experimental

study. Its operation acoustic frequency is 10 MHz.

Photo 5.4. 3D Vectrino ADV (NORTEC)

As shown in Photo 5.5, the probe is down-looking and consists of four receive transducers and a transmit transducer. Each of the four receive transducers is mounted inside a receiver arm. The transmit transducer is in the centre of the probe. The sampling volume, which is located 5 cm below the transmit transducer, is a cylinder of water with a fixed diameter of 6 mm and a user-defined height of 3-15 mm. The sampling rate was also adjustable (0 ~ 200 Hz).

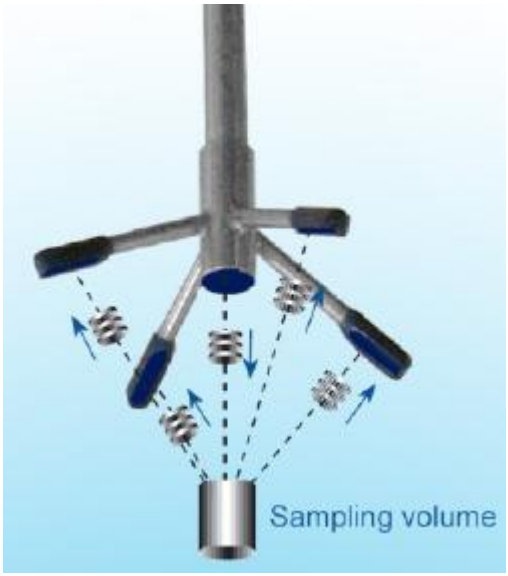

Photo 5.5. Image of the ADV probe and schematic diagram of sampling volume

(Source: Vectrino User Guide 2009)

The ADV technology is based on the measuring method known as pulse-to-pulse coherence (Lohrmann *et al.* 1994; Nikora and Goring 1998). The transmit transducer generates an acoustic signal that is reflected back by sound scattering particles present in water (such as naturally fine particles or seeding material) and are assumed to move at the fluid velocity. The scattered signal is detected by the receivers and used to calculate the signal Doppler phase shift from which the flow velocity components are estimated accordingly. The ADV measures the sound scattered from two consecutive pulses. After the signal is processed, the phase difference determines the value of velocity. A PC with Windows XP operation system was connected directly to the Vectrino to obtain real time series of the velocities. Vectrino Plus software was employed to gather experimental data. The WinADV software (version 2.027) was used to analyze these data.

The correlation coefficient is a measure of the similarity of two pulses. Thus it becomes an important parameter to estimate the quality and accuracy of the ADV velocity data. Correlation is expressed as a percentage: values close to 100% indicate that the transmitted and received signals are fully coherent and thus the measurements are reliable; low correlations indicate insufficient seeding, the probe is out of the water, the signal-to-noise ratio (SNR) is too low, or ADV malfunctioning. It is commonly accepted that the correlation coefficient should be above 70% (e.g., Voulgaris and Trowbridge 1998; Martine 2003). This threshold criterion was also followed in the data analysis performed in this study.

The noise in ADV phase measurements, which is an inherent part of all Doppler-based backscatter systems, is caused by a number of factors. The most important one is the effect of electronics noise which is determined by the SNR. In the laboratory, the minimum SNR at which the ADV should be operated is about 15. Throughout the experiments, the SNR was maintained at 17 or above.

In addition, the Vectrino ADV was equipped with temperature correction, self-adjusting for sound propagation speed depending on the water temperature. The temperature was read by a thermometer included within the ADV.

5.3. Experimental arrangement

5.3.1. Pre-experiment calibration

Flow rate and bed slope are the control parameters for open-channel flow conditions,

the instruments used to measure them need to be calibrated before conducting the experiments. As shown in Photo 5.6, a portable ultrasonic flowmeter (GE Panametrics TransPort, Model PT878) and a rectangular sharp-crested weir were used for the calibration of flow rates. Five flow rates were produced in the flume experiments. Table 5.1 shows the calibration results for these 5 flow rates. It can be seen that the values evaluated from these three methods are very close and their difference is within 5%. The averages, as shown in Table 5.1, were taken as the real values of these flow rates in the following data processing.

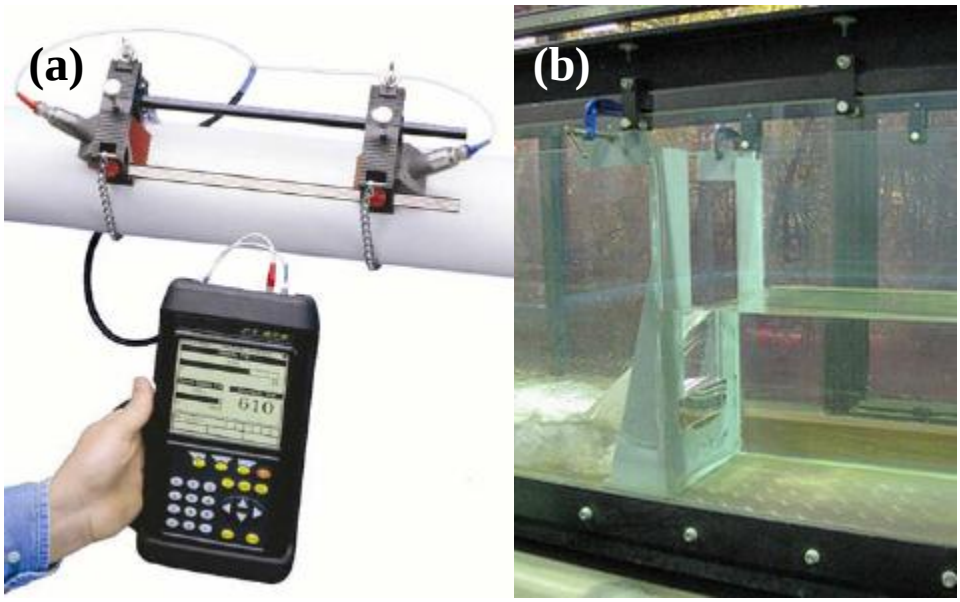

Photo 5.6. Facilities used to calibrate the flow rates

(a) Portable Liquid Flowmeter (Source: Model PT878 User's Manual);

(b) Rectangular sharp-crested weir.

Table 5.1. Calibration results for flow rates

	Build-in electromagnetic flowmeter [m^3/hr]	Portable ultrasonic flowmeter [m^3/hr]	Rectangular sharp-crested weir [m^3/hr]	Average [m^3/hr]
Flow rate Ⅰ (R1)	30	31.4	31.14	30.85
Flow rate Ⅱ (R2)	40	41.67	41.0	40.89
Flow rate Ⅲ (R3)	50	52.1	50.93	51.01
Flow rate Ⅳ (R4)	60	62.63	61.3	61.31
Flow rate Ⅴ (R5)	70	73.02	71.07	71.36

The bed slopes were calibrated with a laser maker (as shown in Photo 5.7). A horizontal laser beam was emitted from the laser maker and projected to the longitudinal direction of the flume. The height of the laser beam from the flume bottom at different locations can be measured and used to calculate the bed slopes. 5 bed slopes (as shown in Photo 5.2) was verified and used in the experiments.

Table 5.2. Calibration results for bed slopes

Bed slope Ⅰ (S1)	1.8‰
Bed slope Ⅱ (S2)	2.5‰
Bed slope Ⅲ (S3)	3.3‰
Bed slope Ⅳ (S4)	4.2‰
Bed slope Ⅴ (S5)	4.8‰

Photo 5.7. Laser maker

5.3.2. Experimental procedures

The experimental study was conducted in the Hydraulic Laboratory of the Civil and Structural Engineering Department at the Hong Kong Polytechnic University. A schematic diagram of the laboratory setup is shown in Figure 5.1. The laboratory flume is a closed system in which water is recirculated by means of an electrically powered pump.

Natural gravels were used to roughen the flume bottom in the testing section. A sample of the gravels were sieved and weighted to obtain the grain size distribution. The weight of the sample was 49.3 kg. The sieving was performed using the following set of sieves: 9.5, 13.2, 19.0, 25.4, 38.1, 50.0 mm. All the gravels were shaked through the sieves from coarser to finer in a mechanical shaker for 10 minutes. These five sub-samples were subsequently weighted. Table 5.3 illustrates the grain size distribution of the gravels. It can be seen that the diameters of most of the particles range from 19.0 mm to 38.1 mm (over 96.7%). Thus the gravels are quasi-uniform with median diameter approximately equal to 23 mm. These gravels were densely and randomly deployed into plates which were then placed consecutively on the flume bottom. The armoured bed was considered fixed since no motion of the gravels was observed throughout the experiments.

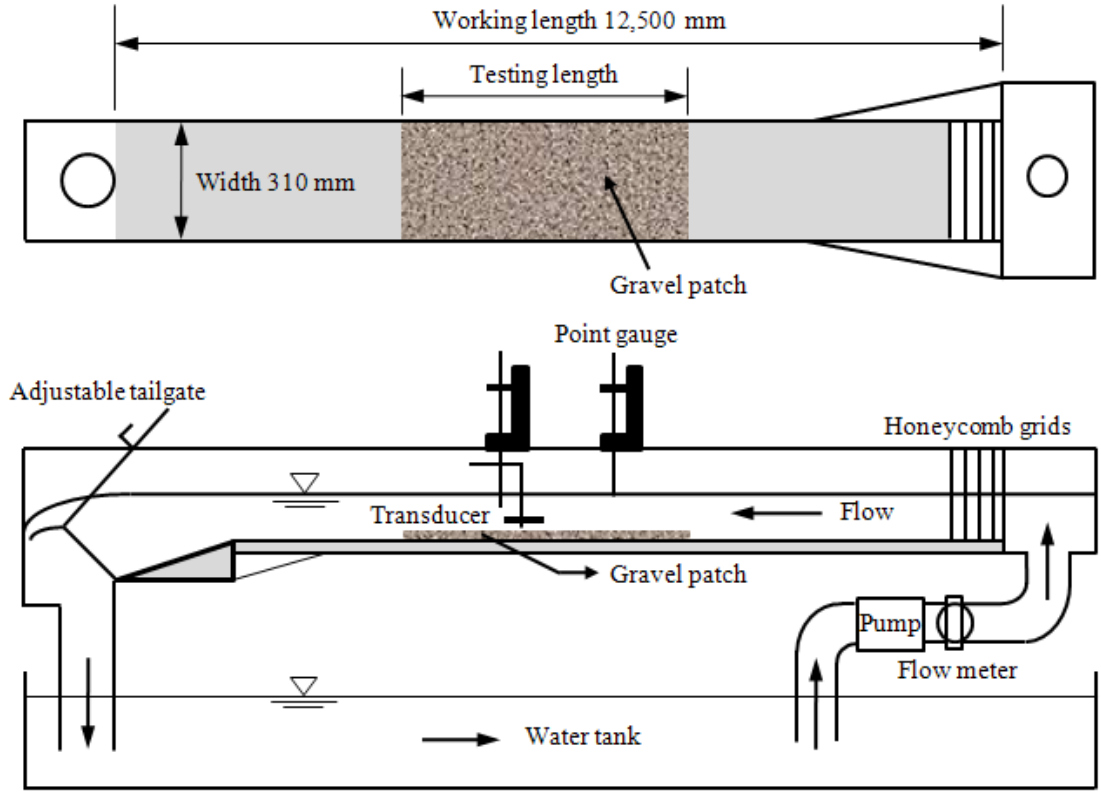

Figure 5.1. Schematic of laboratory setup (not to scale)

Table 5.3. Grain size distribution for the original material

Maximum diameter (mm)	Cumulative finer (%)
50.0	100
38.1	99.3
25.4	83.1
19.0	2.6
13.2	0.2
< 9.5	0.0

Two GPs with different length were tested under the uniform flow condition. Throughout the flume experiments, the water depths along the testing area were monitored. We consider the uniform flow state is reached within the testing area as long as the water depths are identical. The testing length of the short patch (SP) and

long patch (LP) were 3.81 m and 7.5 m, respectively. The gravels used in the SP and LP are also slightly different. While the original gravel pack, which is quasi-uniform, was used in the SP, the uniform gravels with very narrow size distribution (19.0 ~ 25.4 mm) was used in the LP. By using uniform gravels, it can be more effective to control the uniformity of a relatively long patch. The characteristic parameters of these two patches are listed in Table 5.4. These two GPs were both well sorted with low protrusion.

Table 5.4. Characteristic parameters for GPs

	SP	LP
Length (m)	3.81	7.5
Width (m)	0.3	0.3
Median diameter d_{50} (mm)	23	22.2
Thickness k_r (mm)	35	35

Steady uniform flow conditions were obtained by regulating the water level with the downstream tailgate. For the laboratory applications, the water depth is found not very sensitive to the flow rate. The uniform flow condition can be reached for a range of water depths. Past experiences show that the uniform flow depth is the minimum flow depth satisfying the uniform flow criterion. Therefore, for each experimental condition, we followed these procedures: (a) Drop down the tailgate; (b) Turn on the pump and adjust the water discharge to the assigned rate; (c) Raise the tailgate slowly until the uniform flow condition is firstly reached. The uniform flow obtained from this procedure is depth-limited as their water depth is of the same order of magnitude as the bed material size. Water surface elevations were measured with Vernier point gauge at several points along the channel centerline to ensure the uniform flow was maintained.

As shown in Photo 5.3, the transducer of the UVP was placed horizontally inside the water body and measured the longitudinal profile of the centerline velocity. The uniform flow condition was reconfirmed by checking the uniformity of the longitudinal velocity profiles. The vertical profiles of the centerline velocity were obtained by measuring the longitudinal velocity profiles at different levels. The vertical measurement interval was 0.5 cm. At each level, the UVP sampled for 252 s, yielding 4000 records. For the use of Vectrino ADV, the height of the sampling volume was set to 7 mm and the sampling rate was set to 75 Hz according to the sampling frequency criteria suggested by Nezu and Nakagawa (1993). Centreline velocities were measured every 0.5 cm in the vertical direction except for the uppermost 5 cm layer where measurement cannot be performed. At each point, the Vectrino ADV sampled for 107 s, yielding 8000 records. Since the water depth is limited in the study, fewer measurement points were used for a single vertical profile. Thus the experimental data measured by ADV were mainly used to estimate the bottom shear stress and recheck the measuring accuracy of UVP.

The SP and LP began at 3.74 m and 2.5 m from the flume entrance respectively. The testing area was predetermined by checking the uniformity of the longitudinal velocity profiles to ensure a fully developed boundary layer flow was achieved. The velocity measurement section was located between 6.1 m and 6.5 m for SP cases. For each LP case, three vertical profiles were collected from three testing areas, i.e., 5.7 m ~ 6.1 m, 6.1 m ~ 6.5 m, 6.5 ~ 6.9 m (hereinafter referred to as L1, L2 and L3). This arrangement also provides a sufficiently long distance from the downstream weir for the flow to be independent of the downstream boundary condition.

Orientation set up was done so that the measuring instrument's *z* ordinate coincided with the vertical axis and the *x* and *y* coordinates were aligned with the streamwise and spanwise flow directions, respectively. Velocities were measured at 5 mm interval in the vertical direction.

5.3.3. Experiment conditions

A total of 33 experiments were performed (25 with SP and 8 with LP) to investigate the profiles of mean velocity, turbulence intensity, and drag in gravel-bed open-channel flows with small relative submergence. The controllable variables in the laboratory were flow discharge, channel bed slope, and patch length. A summary of the experimental conditions is shown in Table 5.5. It can be seen that the investigated flows are highly turbulent ($1.11 \times 10^5 < \mathrm{Re} < 2.56 \times 10^5$) and subcritical ($0.37 < \mathrm{Fr} < 0.68$). Their relative submergences are relatively small and range from 2.68 to 5.94.

It should be noticed that the aspect ratios (W/D) of the present experiments are all less than 5, the flows thus should be classified as narrow channel flows (Nezu and Nakagawa 1993). In such flow conditions, the secondary currents may occur and result in the velocity-dip phenomena in the outer region. However, in our laboratory setting the gravel-bed is fully rough while the sidewalls are smooth. The effect of aspect ratio is thus less severe as compared to that for the case in which the bottom and sidewalls are equally rough. As a consequence, the streamwise velocity will not be strongly affected by the secondary currents. Nevertheless, when estimating the flow resistance, the correction of the side-wall effect should still be conducted.

Table 5.5. Experimental conditions in gravel-bed flows with limited water depth

	RUN	S_0 [-]	Q [m^3/hr]	D [m]	W/D [-]	S_r [-]	Re (10^5)	Fr [-]
Short patch	SPS1R1	0.0018	30.85	0.084	3.71	3.63	1.11	0.37
	SPS1R2		40.89	0.099	3.14	4.29	1.47	0.38
	SPS1R3		50.01	0.114	2.73	4.94	1.83	0.38
	SPS1R4		61.31	0.124	2.51	5.37	2.2	0.4
	SPS1R5		71.36	0.137	2.27	5.94	2.56	0.4
	SPS2R1	0.0025	30.85	0.078	3.99	3.37	1.11	0.41
	SPS2R2		40.89	0.093	3.35	4.03	1.47	0.42
	SPS2R3		50.01	0.104	2.99	4.5	1.83	0.44
	SPS2R4		61.31	0.113	2.75	4.9	2.2	0.46
	SPS2R5		71.36	0.126	2.47	5.46	2.56	0.46
	SPS3R1	0.0033	30.85	0.074	4.21	3.2	1.11	0.44
	SPS3R2		40.89	0.085	3.66	3.68	1.47	0.48
	SPS3R3		50.01	0.097	3.21	4.2	1.83	0.49
	SPS3R4		61.31	0.107	2.91	4.63	2.2	0.5
	SPS3R5		71.36	0.117	2.66	5.07	2.56	0.51
	SPS4R1	0.0042	30.85	0.072	4.33	3.11	1.11	0.46
	SPS4R2		40.89	0.114	3.94	3.42	1.47	0.53
	SPS4R3		50.01	0.125	3.46	3.9	1.83	0.54
	SPS4R4		61.31	0.136	3.08	4.37	2.2	0.55
	SPS4R5		71.36	0.145	2.83	4.77	2.56	0.56
	SPS5R1	0.0048	30.85	0.103	4.59	2.94	1.11	0.5
	SPS5R2		40.89	0.112	4.05	3.33	1.47	0.55
	SPS5R3		50.01	0.122	3.58	3.77	1.83	0.57
	SPS5R4		61.31	0.13	3.28	4.11	2.2	0.6
	SPS5R5		71.36	0.141	2.94	4.59	2.56	0.59
Long patch	LPS2R1	0.0025	30.85	0.077	4	3.49	1.11	0.46
	LPS2R2		40.89	0.088	3.51	3.98	1.47	0.49
	LPS2R3		50.01	0.101	3.06	4.57	1.83	0.53
	LPS2R4		61.31	0.117	2.64	5.29	2.2	0.54
	LPS5R1	0.0048	30.85	0.059	5.22	2.68	1.11	0.61
	LPS5R2		40.89	0.069	4.46	3.13	1.47	0.64
	LPS5R3		50.01	0.077	4	3.49	1.83	0.68
	LPS5R4		61.31	0.088	3.51	3.98	2.2	0.67

Code for the names of the runs:

SP and LP – stand for short gravel patch and long gravel patch (Table 5.4)

S1, S2, S3, S4 and S5 – stand for different bed slopes (Table 5.2)

R1, R2, R3, R4 and R5 – stand for different flow rates (Table 5.1)

5.4. Experimental results

5.4.1. Shear velocity

Detail investigation of turbulence structures in open-channel flow requires accurate evaluation of the shear velocity u^*. This parameter is of engineering significance as it represents the skin friction drag, and is also an essential scaling parameter for the theoretical analysis of the mean velocity profile and turbulence intensity profile. Several methods for the determination of the shear velocity can be found in the literature (Nezu and Nakagawa 1993):

1. Clauser's method

   The shear velocity can be determined from the measured mean velocity profile in conjunction with the logarithmic law (Equation 2-7).

2. Energy-gradient method

   The shear velocity can be calculated using the global momentum balance equation under the uniform flow condition as follows:

$$u^* = \sqrt{gDS_0} \tag{5-3}$$

3. Reynolds-stress method

   The shear velocity can be determined by extending the measured Reynolds stress profiles to the boundary, i.e.,

$$u^* = \sqrt{\tau_0/\rho} = \sqrt{-\overline{u'w'}\Big|_{z=0}} \tag{5-4}$$

4. Mean-velocity profile in the viscous sublayer

   If a viscous sublayer exists, the shear velocity can be deduced by using the linear distribution of the mean velocity (Equation 5-5) in this sublayer.

$$\bar{u}/u* = z \cdot u*/\nu \tag{5-5}$$

5. Direct measurement

   The shear velocity can be determined by using skin friction probes, Preston tubes, etc.

Amongst the methods described above, the first three methods were used in this study.

The evaluation of shear velocities by using Clauser's method can be problematic over rough beds (Smart 1999), since three unknowns must be determined simultaneously: h_1, k_s, and $u*$. Furthermore, the universal logarithmic law for the velocity distribution might not exist in gravel-bed flows with small relative submergence. To address this problem, Manes *et al*. (2007) suggested a procedure to evaluate h_1 and $u*$ in the absence of the universal log law and confirmed that the zero-plane position depends on the roughness density and energy of large eddies. In other words, a gravel-bed flow with small relative submergence but of the same $u*$ and roughness density as a flow with a larger relative submergence should have the same zero-plane displacement as that flow. Following their conclusions, the assumptions used by Kironoto and Graf (1994) were taken herein to identify the h_1 and k_s since the roughness geometry and the flow properties of their experimental study are similar to the present flume experiments. The present laboratory experiments can be considered as a continuing study of Kironoto and Graf (1994) as their investigated flows were under a large relative submergence. They assumed $k_s = d_{50}$ and $h_1 = 0.2k_s$, and also justified these assumptions in the data analysis. Therefore, in the present study the equivalent sand roughness k_s is taken to be $k_s = d_{50} = 2.3$ cm

for the SP case, and k_s = 2.22 cm for the LP case. Since the use of the Clauser's method is still questionable for gravel-bed flows with small relative submergence, the results of the shear velocities estimated by the energy-gradient method (u^*_e) and Reynolds-stress method (u^*_r) are compared in Table 5.6 for selected cases. It should be noted that the agreement between the values of u^*_r and u^*_e are not so favorable with the maximum difference up to 10%. This error could be attributed to the deficient performance of the ADV near the channel bed (Precht *et al.* 2006). Firstly, the ADV technique underestimates the flow velocities very close to the bottom inherently. Secondly, the sampling volume used in the flume experiments was not small enough for the near-bottom measurements.

Table 5.6. Comparison of the shear velocities calculated by energy-gradient method (u^*_e) and Reynolds-stress method (u^*_r).

RUN	S_0 [-]	$u^*_e \times 10^2$ [m/s]	$u^*_r \times 10^2$ [m/s]	$(u^*_e - u^*_r)/u^*_e$ (%)
SPS1R4	0.0018	4.68	4.24	9.4
SPS2R4	0.0025	5.23	5.05	3.44
SPS3R4	0.0033	5.89	5.47	7.13
SPS4R4	0.0042	6.41	6.31	1.56
SPS5R4	0.0048	6.7	6.27	6.42
LPS5R3L1	0.0048	6.06	5.54	8.58
LPS5R3L2	0.0048	6.06	5.88	2.97
LPS5R3L3	0.0048	6.06	6.01	0.83

By taking u^*_e as the reference, κ and B_r can be determined by fitting the measured vertical velocity profiles to Equation 2-7 with the predetermined k_s and h_1. For the fitting process, the Karman constant of κ = 0.4 (recommended by Kironoto and Graf (1994) for the gravel-bed flows with large relative submergence) was assumed at the very beginning. The data in the inner region were fitted against the logarithmic-linear

equation (Equation 2-7) using the least squares method which is available as an add-in sub-program in Microsoft Excel. The values of κ and Br affecting the slope and y-intercept of the logarithmic curve (Equation 2-7) can then be determined. The correlation coefficients of the least square fitting were $R \geq 0.974$ for SP cases, and $R \geq 0.991$ for LP cases.

5.4.2. Velocity profiles

Totally 49 vertical profiles (25 for SP case and 24 for LP case) were collected in the laboratory flume under uniform flow condition. Since the UVP measures the streamwise component of the velocities along a distance of 9.5 cm, its averaged values can be considered as double averaged values, i.e., spatially and temporally averaged. It has been widely recognized that the double averaging procedure could account for the spatial heterogeneity effect of the rough bed (Buffin-Belanger *et al.* 2006; Nikora *et al.* 2007a; Nikora *et al.* 2007b).

Figure 5.2 shows the comparison between the streamwise velocities measured by the ADV and UVP for runs SPS1R4, SPS2R4, SPS3R4, SPS4R4 and SPS5R4. The good agreement ($R^2 = 0.9391$) indicates that the accuracy of these two measuring instruments is acceptable.

Figure 5.3 shows the power spectra of the measured velocity components for the run LPS5R3L1 ($S_r = 3.49$) from ADV. It is noteworthy that, even with the small relative submergence, the power spectra still approximately follow the classic Kolmogorov -5/3 law.

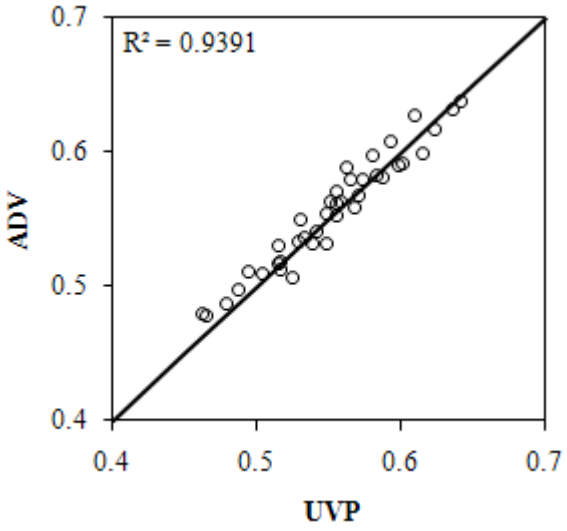

Figure 5.2. Comparison between streamwise velocities measured by UVP and ADV

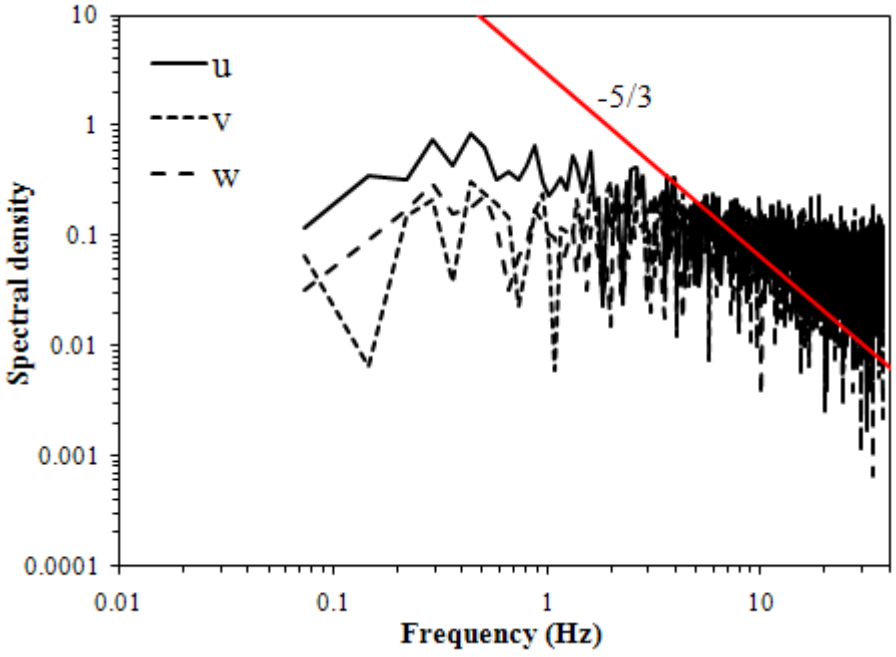

Figure 5.3. Power spectra of velocity components from ADV (LPS5R3L1 with S_r = 3.49, at depth z/D = 0.35; for reference, -5/3 power slope is also shown by the red straight line.)

The resultant histograms of the probability density function (PDF) distribution of velocity for run LPS5R3L1 are shown in Figure 5.4. It can be seen that the PDFs of the three velocity components resemble Gaussian distribution, which indicates that the sampling size is large enough to yield adequate flume measurements.

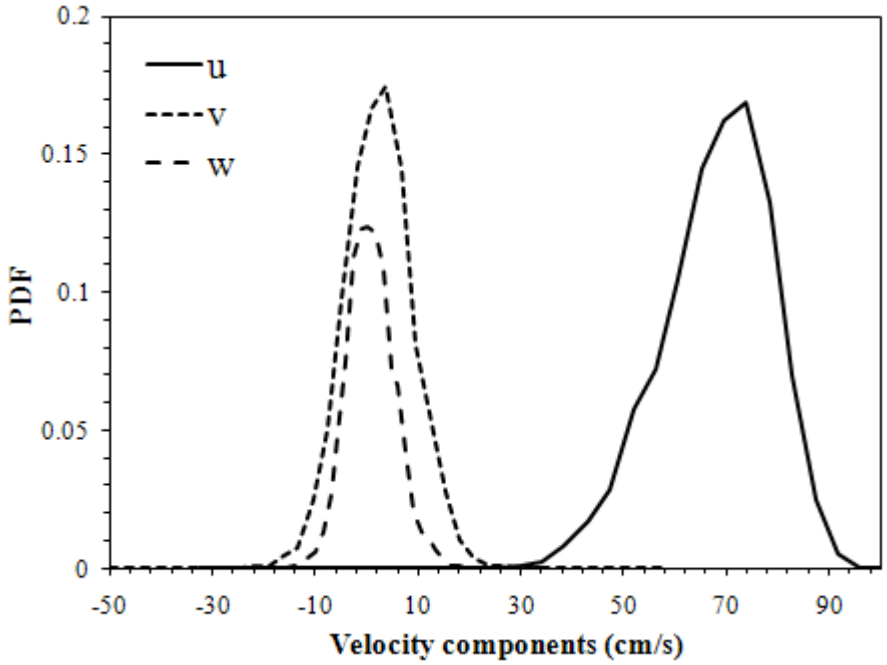

Figure 5.4. Probability density function (PDF) of velocity components from ADV (LPS5R3L1 with S_r = 3.49, at depth z/D = 0.35.)

Figure 5.5 and Figure 5.6 show the double averaged velocity profiles for selected SP case (SPS5R1) and LP case (LPS5R1L1) respectively. It can be seen that the double averaged velocity profiles still agree well with the log law and the defect law even under small relative submergence (S_r = 2.94 for SP case and S_r = 2.68 for LP case) in the present experiments. It can be explained by the fact that the gravel patches were well sorted with low protrusion. Therefore, the S-shaped velocity profiles were not

observed throughout the laboratory experiments. It can also be found from these two figures that the streamwise velocity data follow the outer velocity-defect law without the need for a wake correction for both SP and LP cases. This can be interpreted as a confirmation that the effect of the aspect ratio is not evident in the depth-limited open-channel flow with gravel roughness.

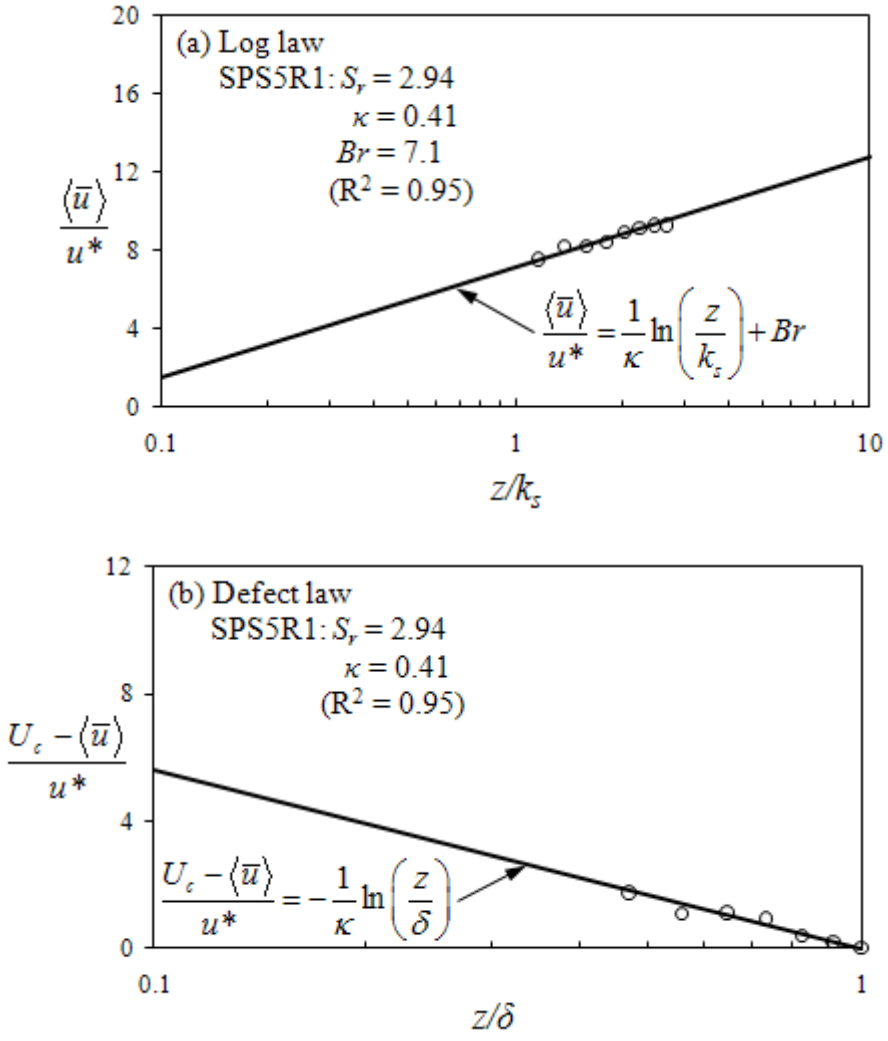

Figure 5.5. Double averaged velocity profiles of selected SP case:

(a) Fitting with log law; (b) Fitting with defect law

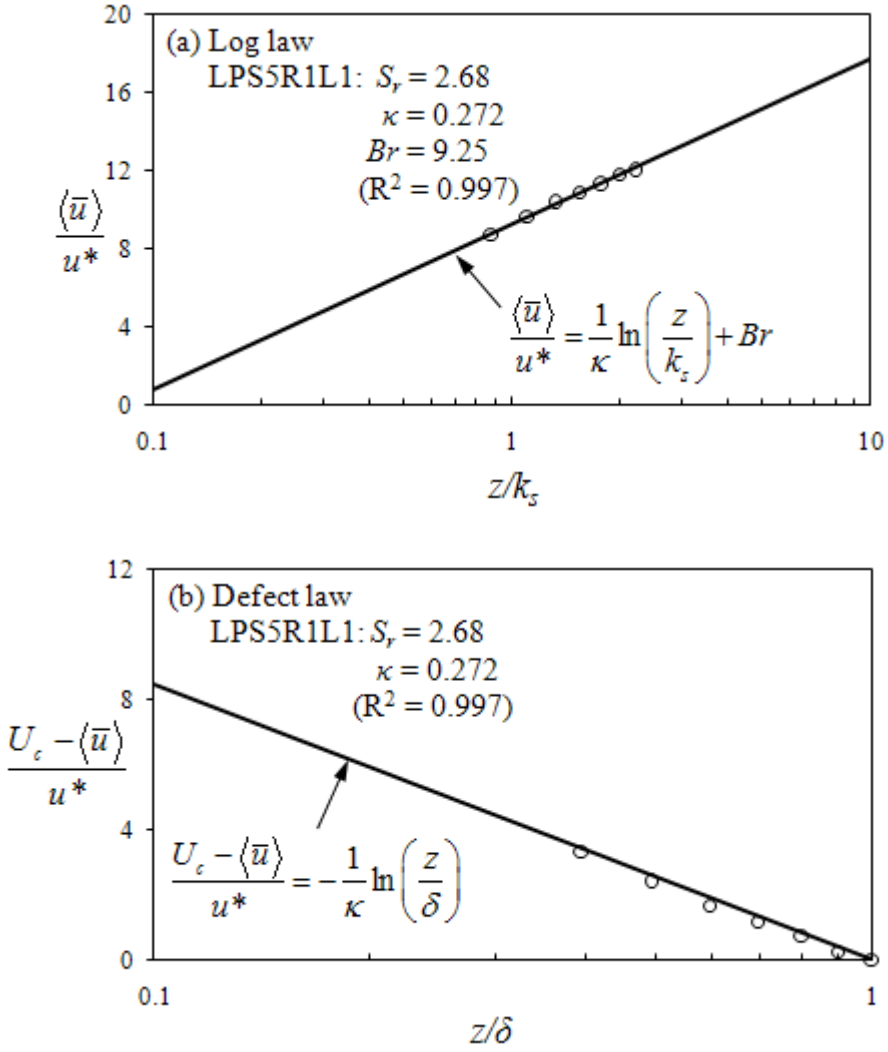

Figure 5.6. Double averaged velocity profiles of selected LP case:

(a) Fitting with Log law; (b) Fitting with Defect law

Figure 5.7 shows the values of κ for different relative submergence S_r. It can be seen from this figure that with nearly the same S_r, the values for SP cases are greater than 0.3 with the mean value approximately equal to 0.4 and the values for LP cases are smaller than 0.3 with the mean value approximately equal to 0.23. Although the non-monotonic dependency of κ on S_r was not observed, the values for LP cases are more consistent with the previously reported κ-values with small relative submergence. As the κ-value reflects the formation and evolution of turbulence coherent structures, the

higher κ-values of the SP cases could be attributed to the finite patch length. Because of the finite length, the large-scale coherent vortices are not fully developed and thus not strong enough to completely alter the velocity gradient near the rough bed. With sufficient length for LP cases, it also can be found from Figure 5.7 that the κ-values of different locations (L1, L2 and L3) do not vary significantly.

There are also some uncertainties in the determination of the numerical constant *Br* in log law (Equation 2-7). For smooth-bed open-channel flow, Nezu and Nakagawa (1993) suggested that B_r = 5.0 - 5.3 irrespective of flow type. Reynolds (1974) suggested *Br* = 8.5 $\pm$ 15% for rough-bed open-channel flows and Kironoto and Graf (1994) further reported *Br* = 8.8 $\pm$ 0.96 (mean and standard deviation of *Br* value) for gravel-bed open-channel flow with large relative submergence (S_r > 12.3). For the depth-limited gravel-bed open-channel flow (2.68 < S_r < 5.94) investigated in the present study, the average *Br*-value is *Br* = 8.2 $\pm$ 0.71, which is in good agreement with the values reported by Reynolds (1974) and smaller than the values suggested by Kironoto and Graf (1994) for gravel-bed open-channel flow with large relative submergence. Figure 5.8 shows the variation of B_r with dimensionless roughness height k_s^+ (for LP cases, the *Br*-value is the average of three profiles in different locations). Within experimental scatter range, it still can be found that for the SP cases the *Br*-value decreases gradually as k_s^+ increases which are consistent with the variation of *Br* for transitionally-rough flows (5 < $k_s^+ \leq$ 70). However, for the LP cases, the *Br*-value remains nearly constant and equals to 8.5 which is consistent with the value of *Br* for fully rough flows (k_s^+ > 70). The decrease of *Br*-value with k_s^+ for open-channel flow over short gravel patch (even with 885 < k_s^+ < 1630) could also be attributed to the finite patch length.

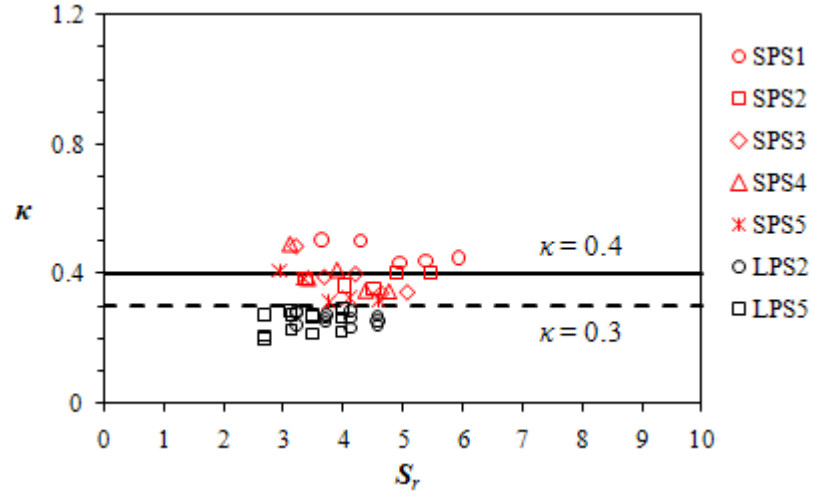

Figure 5.7. Variation of κ with relative submergence S_r

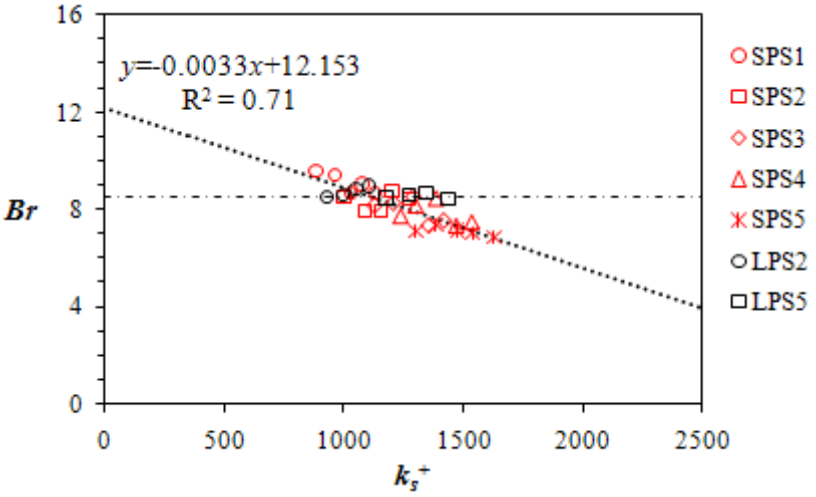

Figure 5.8. Variation of B_r with dimensionless roughness height k_s^+

5.4.3. Streamwise turbulence intensity

The vertical distribution of streamwise turbulence intensity (I), which is defined as the ratio of the root-mean-square of the velocity fluctuations u_{rms} to the shear velocity u^*, has been measured in earlier research work (Nezu 1977; Nezu and Rodi 1986; Cardoso *et al.* 1989; Wang *et al.* 1993) on smooth- and rough-bed open-channel flows. For uniform open-channel flow, Nezu (1977) claimed that the distribution of the streamwise turbulence intensity is independent of the Reynolds and Froude

numbers and follows an exponential law:

$$I = \frac{u_{\text{rms}}}{u*} = \frac{\sqrt{u'^2}}{u*} = D_{\text{u}} e^{-\lambda_{\text{u}}(z/D)} \tag{5-6}$$

Nezu (1977) also suggested that D_{u} = 2.3 and λ_{u} = 1.0 for smooth-bed open-channel flow. Nezu and Rodi (1986) measured in details the distribution of turbulence intensity for the uniform flow in a smooth-bed flume with a two-dimensional LDA. By regression analysis on their experimental results and other available flume measurement data (Clark 1968; Blinco 1971; Nezu 1977; Steffler *et al.* 1983), they reported D_{u} = 2.26 and λ_{u} = 0.88. Caroso *et al*. (1989) carried out similar flume studies and suggested that D_{u} = 2.28 and λ_{u} = 1.08 for smooth-bed open-channel flow. The values of D_{u} and λ_{u} reported by Nezu and Rodi (1986) and Caroso *et al*. (1989) agree well with the values of Nezu (1977). Therefore, D_{u} = 2.3 and λ_{u} = 1.0 can be considered as the standard values for smooth-bed open-channel flow. For gravel-bed open-channel flow, Wang *et al*. (1993) suggested that the distribution of the streamwise turbulence intensity depends greatly on the relative submergence S_r and D_{u} = 2.14 and λ_{u} = 0.8 when $S_r \dot{\geq} 4$. Kironoto and Graf (1994) reported that D_{u} = 2.04 and λ_{u} = 0.97 for uniform open-channel flow over rough plate and gravel bed.

Figure 5.9 and Figure 5.10 respectively show the distributions of streamwise turbulence intensities for SP and LP cases, together with the empirical equations proposed by Nezu (1977) and Wang *et al*. (1993). Due to the sample volume limitation of the UVP and its poor performance in the near-bottom region, the data for the distribution in the inner region ($z/D < 0.2$) as well as the peak value were lost. The present experimental data, for both SP and LP cases, were evaluated with the least squares method; the empirical constants were found to be: D_{u} = 2.28 and λ_{u} =

1.11 for SP case (with correlation coefficient, R = 0.8), and D_u = 2.44 and λ_u = 0.83 for LP case (R = 0.91). The streamwise turbulence intensity distributions of the present data compare reasonably well with the experimental data from the literatures. Even under the small relative submergence (S_r = 2 ~ 3), the measured streamwise turbulence intensities also fit well the empirical equation obtained for $S_r \geq 4$ (Wang *et al.* 1993) in the intermediate region, which should be attributed to the low-protrusion of the gravel-bed used in the present study.

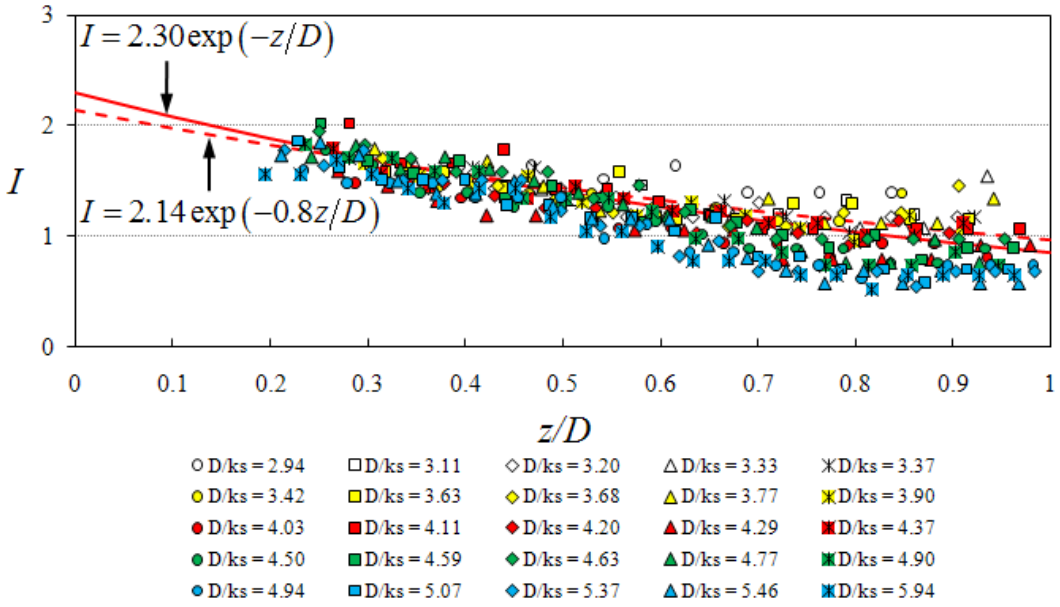

Figure 5.9. Variation of streamwise turbulence intensity I as a function of z/D for SP cases

Apart from more evident experimental scatter among the SP cases, the streamwise turbulence intensity distributions for the SP and LP cases are very similar. Within the near-water-surface region ($0.7 < z/D < 1$), the streamwise turbulence intensity increases gradually with the water depth, which could be induced by the effect of surface waves (Nezu and Nakagawa 1993). However, it was reported that this effect

is significant only for near-critical flows, i.e., Fr → 1. As the investigated flows in the present study are all subcritical (0.37 < Fr < 0.68), the surface waves should be caused by the enhanced large-scale coherent structures and the narrow width of laboratory flume. The large-scale coherent structures are enhanced because of the completely rough bottom and the limited water depth. The effect of the surface waves is also one of the reasons that the scatter of experimental data is larger near the free surface.

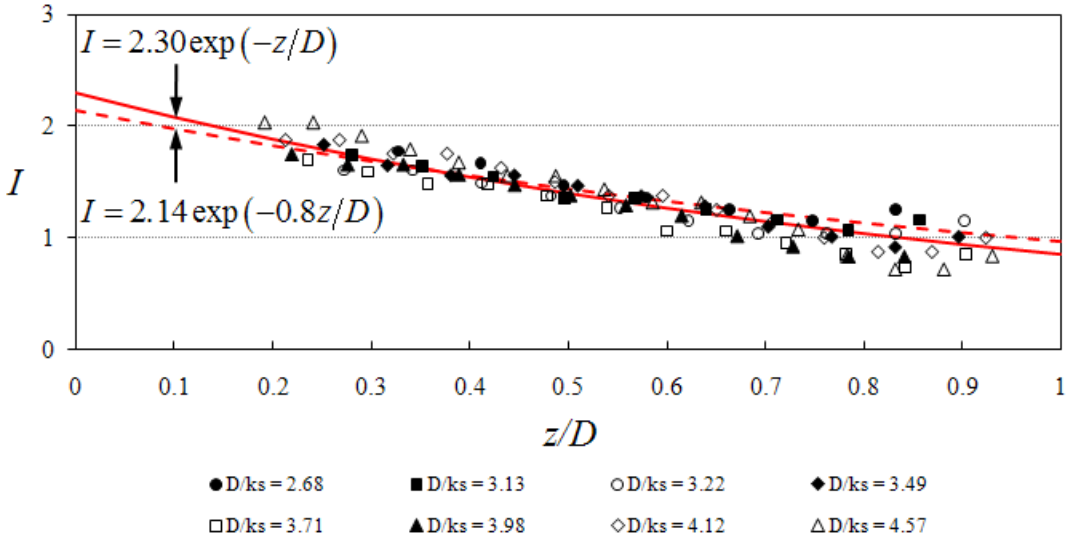

Figure 5.10. Variation of streamwise turbulence intensity I as a function of z/D for LP cases

Figure 5.9 and Figure 5.10 also compare the distribution of streamwise turbulence intensity for a wide range of relative submergence (D/k_s). It can be seen that the main difference occurs within the near-water-surface region ($0.7 < z/D < 1$). With the decrease of the relative submergence, the streamwise turbulence intensity increases significantly, which indicates that the effect of the surface waves is more evident. With the decrease of the relative submergence, the influence of the bed roughness on

flow turbulence increases and gives rise to stronger coherent vortices above the roughness elements.

5.4.4. Flow resistance

Well-established flow resistance formulas, such as the Darcy-Weisbach, Manning and Chezy equations, have long been used for open-channel flow. The flow resistance is commonly represented by three resistance coefficients, i.e., the Darcy-Weisbach friction factor (f), Manning roughness coefficient (n) and Chézy resistance factor (C_h). These three factors are related to the mean flow velocity through the following equations:

$$\bar{U} = \frac{K_n}{n} R_h^{2/3} S_f^{1/2} \quad \text{(Manning)} \tag{5-7}$$

$$\bar{U} = \sqrt{\frac{8g}{f}} \sqrt{R_h S_f} \quad \text{(Darcy-Weisbach)} \tag{5-8}$$

$$\bar{U} = C_h \sqrt{R_h S_f} \quad \text{(Chézy)} \tag{5-9}$$

where R_h = hydraulic radius, S_f = friction slope (= S_0, the bed slope in uniform flow conditions); g = gravitational acceleration; and K_n = 1 for $\bar{U}$ and R_h in SI units, 1.486 for $\bar{U}$ in ft/s and R_h in ft. From the above three equations, the resistance coefficients can be related by the following equation.

$$\sqrt{\frac{f}{8}} = \frac{n}{R_h^{1/6}} \frac{\sqrt{g}}{K_n} = \frac{\sqrt{g}}{C_h} = \frac{\sqrt{g R_h S_f}}{\bar{U}} \tag{5-10}$$

Therefore, knowing the value of one resistance coefficient, the values of other two resistance coefficients can be calculated.

5.4.4.1. Manning resistance coefficient

The relationship between the Manning resistance coefficient n and the relative submergence S_r (= D/k_s) was proposed by Sturm (2010) as follow:

$$c_n = \frac{n}{k_s^{1/6}} = \frac{\frac{K_n}{(8g)^{1/2}}\left(\frac{D}{k_s}\right)^{1/6}}{2.03\log\left(12\frac{D}{k_s}\right)} \tag{5-11}$$

where K_n = 1.0 for SI units and 1.49 for English units. The parameter c_n (=$n/k_s^{1/6}$) was found to be roughly constant over a fairly wide range of S_r and therefore is not a function of the flow depth (Sturm 2010). Furthermore, c_n was reported to vary within ±5% of a constant value over a range of $4 < S_r < 500$ (Yen 1992). However, in the literature different values of c_n were reported. Sturm (2010) suggested that the value is 0.039 in SI units (0.032 in English units), which is close to that reported by Henderson (1966) (0.041 in SI units, 0.034 in English units). This value was also verified in the case that the effective size in the gravel-bed stream is larger than d_{50} due to bed armoring. Several other sources, including Hager (1999), however, reported the value of c_n = 0.048 in SI units (0.039 in English units).

Due to the narrow width of the laboratory flume, the resistance effect of the glass side-walls has to be considered in analyzing the flow resistance. The Manning resistance coefficient calculated from Equation 5-7 is an equivalent n value which is corresponding to the composite roughness of channel bottom and side-walls. In order to distinct the roughness effect of the gravel-bed, a correction of the side-wall effect should be conducted to the equivalent n value. Following Chow (1959), we assumed that the total force resisting the flow is equal to the sum of the forces resisting the

flow developed in the subdivided areas, i.e., the near-bottom area and near-side-wall area. According to this assumption, the equivalent roughness coefficient can be decomposed as:

$$n = \frac{\left[\sum_{1}^{N}\left(P_N n_N^2\right)\right]^{1/2}}{P^{1/2}} = \frac{\left(P_b n_b^2 + P_w n_w^2\right)^{1/2}}{P^{1/2}} \tag{5-12}$$

where n, n_b and n_w denote the equivalent roughness coefficient, roughness coefficient for gravel bed and glass side walls, respectively. P, P_b and P_w denote the total wetted perimeter and wetted perimeter for gravel bed and glass side walls, respectively. Since the roughness coefficient for glass wall can be considered constant (n_w = 0.01), the roughness coefficient for the gravel bed can be evaluated accordingly.

The variation of the measured c_n (= $n_b/k_s^{1/6}$) with the relative submergence are plotted in Figure 5.11, together with the Equation 5-11. The agreement is satisfactory with the values of c_n around 0.04, supporting the results of Sturm (2010) and Henderson (1966). It can also found this figure that the values of the c_n for SP cases are greater than that for LP cases. This can be explained by the fact that the gravel roughness elements are more irregular in SP cases than that in LP cases. Generally speaking, the irregularity of the bed roughness leads to a higher relative grain protrusion and consequently a greater flow resistance effect.

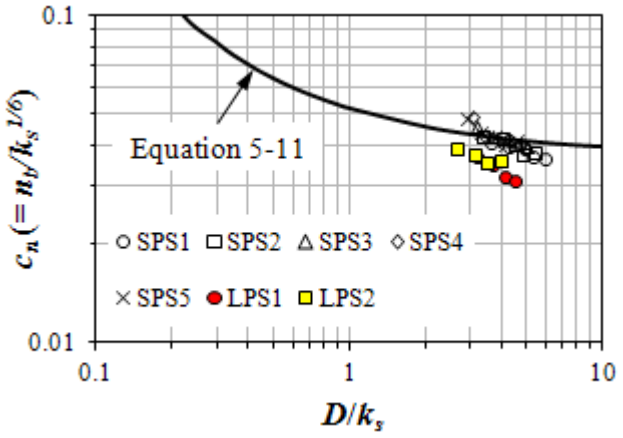

Figure 5.11. Variation of c_n (= $n_b/k_s^{1/6}$) with relative submergence S_r (= D/k_s)

5.4.4.2. Darcy-Weisbach friction factor

For the rough-bed open-channel flow with large relative submergence, the flow resistance law, which can be theoretically deduced from the log law through an integration procedure, is semi-logarithmic:

$$\frac{\bar{U}}{u*} = \sqrt{\frac{8}{f}} = \frac{1}{\kappa}\ln\left(\frac{R_h}{k_s}\right) + \overline{Br} \qquad (5\text{-}12)$$

where $\bar{U}$ is the cross-sectional averaged velocity; f is the Darcy-Weisbach friction factor; R_h is the hydraulic radius; $\overline{Br}$ is a integration constant.

Considerable studies have been performed on the resistance to flow over sand, gravel and boulder-bed channels, in both man-made and natural open-channel flows. A value of 6.25 is usually adopted for $\overline{Br}$ in the case of infinitely wide channels for large relative submergence of S_r > 20 (Graf *et al.* 1991). In the case of small relative submergence of S_r < 4 a $\overline{Br}$-value of 3.25 is recommended by Graf (1984), whereas in the intermediate range of 4 < S_r < 20 a linear relationship is supposed to exist (Graf *et al.* 1991) between the two threshold values of 3.25 and 6.25.

The corrected value of the Darcy-Weisbach friction factor (f_b) for the gravel bed can be calculated through the relationship between the f_b and n_b (Equation 5-10). When concerning about the f_b, the hydraulic radius $R_h = A/P_b = A/W = D$. The equation 5-12 thus can be rewritten as:

$$\sqrt{\frac{8}{f_b}} = \frac{1}{\kappa}\ln\left(\frac{D}{k_s}\right) + \overline{Br} \tag{5-13}$$

Figure 5.12 shows the variation of the measured $(8/f_b)^{1/2}$ with relative submergence, together with the Equation 5-13. The dash line indicates the Equation 5-13 with κ = 0.22 and $\overline{Br} = 3.25$ and the solid line indicates the Equation 5-13 with κ = 0.22 and $\overline{Br} = 6.25$. It can be seen that under the relatively small submergence ($2.68 < S_r < 5.94$), while the Karman constant κ decrease in the log law, it also decreases to 0.22 in the flow resistance law (Equation 5-13). Furthermore, the experimental data for the SP and LP cases follow the linear relationship and generally fall within the threshold $\overline{Br}$ -values of 3.25 and 6.25.

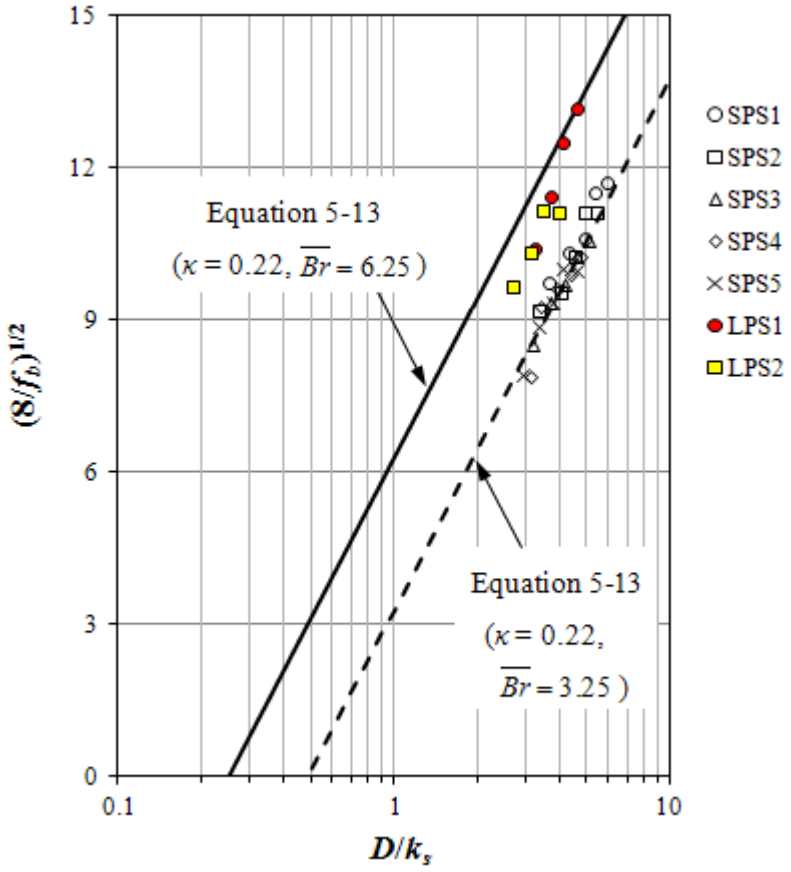

Figure 5.12. Variation of $(8/f_b)^{1/2}$ with relative submergence S_r (= D/k_s)

5.5. Numerical model results

The 1D DANS model developed in Chapter 4 was used to replicate the laboratory experimental cases herein. The drag force method (DFM) was employed to simulate the gravel-induced resistance effect. The drag force term is added within the roughness layer (from reference level to the visual bed level). A rectilinear mesh with refinement at the near wall region is used in the simulation. In order to evaluate the sensitivity of the drag force parameter (f_{rk}) to mesh resolution, a fine mesh with 60 grid cells and a coarse mesh with 30 grid cells were used in the simulation under the same flow condition.

Figure 5.13(a) and (b) show the comparison between the numerical results and the experimental data for the run SP2S2R4 (S_r = 4.9) with fine mesh and coarse mesh, respectively. It can be found that the calculated velocity profiles from both mesh systems fit the logarithmic law well in the inner region. Only a slight difference occurs for the velocities at the near-water-surface region where the number of grid cells has been significantly reduced as shown in Figure 5.13(b). The best-fit values of f_{rk} for cases with fine mesh and coarse mesh are 36 m^{-1} and 29 m^{-1}, respectively. Therefore, the value of the f_{rk} is dependent on the grid resolution. This is mainly due to the presence of a sharp discontinuity in the drag force distribution (f_{rk} = 0 above the gravel layer).

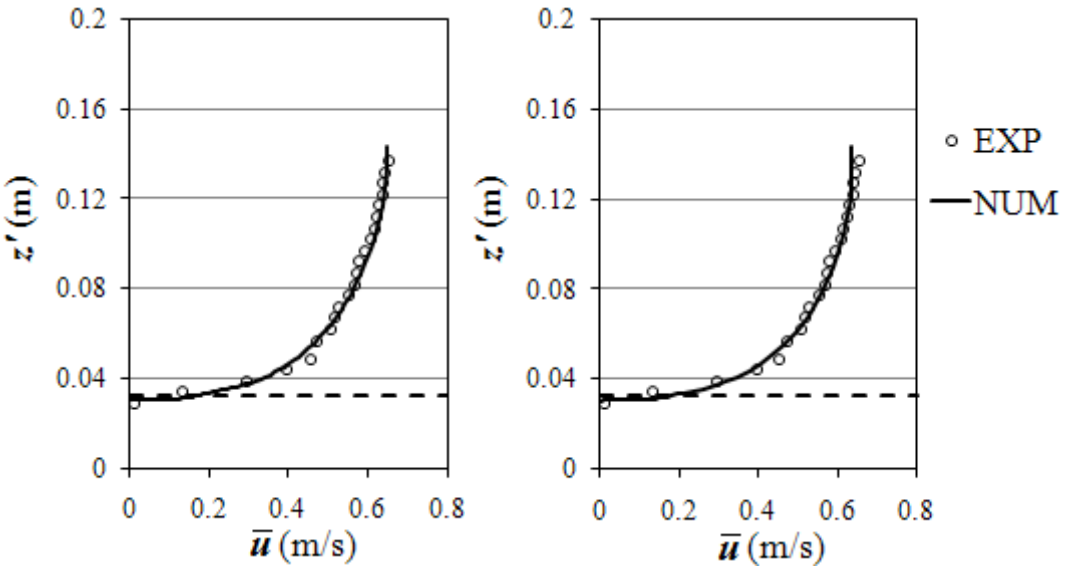

(a) Fine mesh (b) Coarse mesh

Figure 5.13. Measured and calculated velocity profiles for SPS2R4

(The dash line denotes the reference level)

Figure 5.14 and Figure 5.15 show the best-fit values of the f_{rk} for the SP and LP cases, respectively. It can be seen from these figures that the f_{rk} remains roughly constant for a single bedform with different relative submergence (S_r), which is of great benefit for the practical application of DFM. The best-fit f_{rk}-values for the SP cases are apparently greater than that for the LP cases which should attribute to the greater shielding factors (C_s, Equation 4-11) for the gravel bed in SP cases.

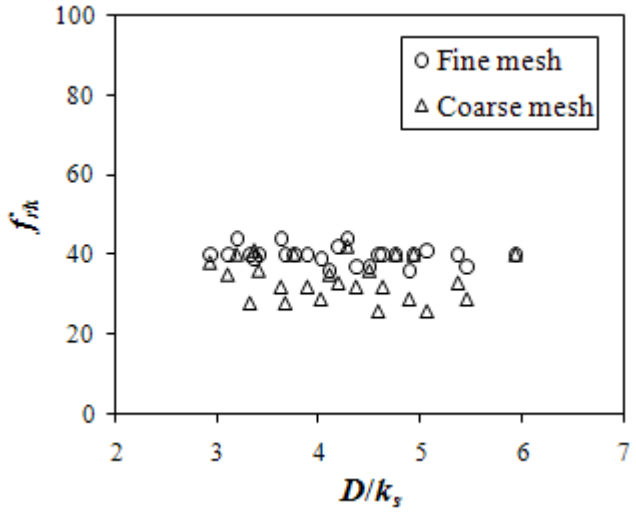

Figure 5.14. Best-fit values of f_{rk} (m^{-1}) against S_r for SP cases

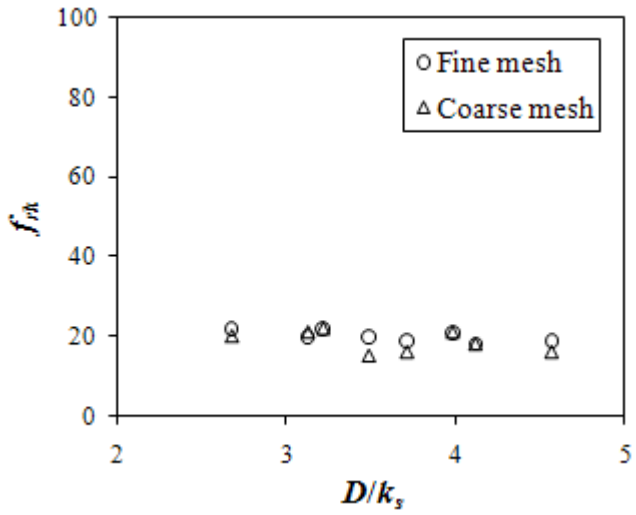

Figure 5.15. Best-fit values of f_{rk} (m^{-1}) against S_r for LP cases

Evident difference occurs in the best-fit values of f_{rk} between cases with fine mesh and coarse mesh. For the SP cases, the best-fit f_{rk} = 39.8 ± 2.2 m^{-1} (mean and standard deviation) with fine mesh and f_{rk} = 34.1 ± 5.1 m^{-1} with coarse mesh. For the LP cases, the best-fit f_{rk} = 20.1 ± 1.5 m^{-1} with fine mesh and f_{rk} = 18.6 ± 2.7 m^{-1} with coarse mesh. For both the SP and LP cases in the present study, the variance of the best-fit f_{rk}-values decreases significantly with the increase of grid cells by 50%. Therefore, with sufficient grid resolution, it could be feasible to take the f_{rk} as a constant for the computations of streamwise velocity profiles with different S_r. In other words, once the f_{rk} is successfully verified for one case with arbitrary S_r, it can be used in the other cases with different S_r.

5.6. Conclusions

Laboratory experiments were performed to investigate the mean streamwise velocity and turbulence intensity distributions, as well as the friction factors in depth-limited open-channel flow over gravel patch with the relative submergence (S_r) ranging from 2.68 to 5.94. The following conclusions can be drawn from the present study:

1. The measured double averaged velocity profiles were found to fit well with the log law and defect law with a non-universal Karman constant κ under small relative submergence. For the LP cases, with fully developed coherent large-scale vortices, the values of κ are nearly constant and in the range from 0.2 to 0.3. However, due to the finite patch length, the κ-values are scattered within a wider range from 0.3 to 0.5 for the SP cases. Furthermore, while the *Br*-value remains constant and equals to 8.5 for LP cases, the *Br*-value was found to decrease with the increase of

dimensionless roughness height k_s^+ for SP cases.

2. The streamwise turbulence intensity distributions under the small relative submergence were found to agree well with the empirical equations proposed by Nezu (1977) and Wang *et al*. (1993). The streamwise turbulence intensity increases gradually with the water depth within the near-water-surface region ($0.7 < z/D < 1$), which could be induced by the effect of surface waves. The streamwise turbulence intensity increases significantly in this region with the decrease of the relative submergence.
3. The measured value of c_n (= $n_b/k_s^{1/6}$) was found to be around 0.04, supporting the results of Sturm (2010) and Henderson (1966). Under the relatively small submergence, the κ-value decrease to 0.22 for the flow resistance law (Equation 5-13). The experimental data follow the linear relationship and generally fall within the threshold $\overline{Br}$-values of 3.25 and 6.25.
4. The 1D DANS model developed in Chapter 4 successfully reproduced the measured streamwise velocity profiles. The best-fit value of f_{rk} was found to be roughly constant for a single bedform with different S_r. The sensitivity analysis on f_{rk} indicates that its value is greatly dependent on the grid resolution, mainly due to the presence of a sharp continuity in the drag force distribution at the gravel-water interface.

Chapter 6.

Open-Channel Flow with Finite Flexible Vegetation Patch

6.1. Introduction

Submerged vegetation canopy plays an important role in aquatic ecosystems worldwide. The presence of a vegetation patch (VP) could baffle local currents and dampen wave energy by producing additional hydrodynamic drag force with the plant stems and branches. Therefore, the VPs are able to protect the wetland areas from erosion. In addition, the patchy vegetation creates regions of increased or decreased bed shear stresses and is of benefit to habitat and species diversity (Kemp *et al.* 2000; Shields and Rigby 2005). Furthermore, through the direct uptake of nutrients and heavy metals (Keskinkan *et al.* 2004), the capture of suspended sediment (Palmer *et al.* 2004) and the production of oxygen, submerged VP can dramatically improve water quality.

A number of experimental (both laboratory and prototype) and numerical studies have been conducted in the recent years to investigate the mean flow and turbulence characteristics of fully-developed open-channel flow with submerged vegetation canopies (Lopez and Garcia 2001; Jarvela 2002; Choi and Kang 2004; Poggi *et al.* 2004a; Ghisalberti and Nepf 2006; Okamoto and Nezu 2009; Li and Yu 2010;

Dimitris and Panayotis 2011 and their references). However, the effect of a limited length VP on aquatic environment has received less attention. Several experimental studies have been devoted to this topic. Neumeier (2007) made laboratory observations on the turbulence distribution and flow evolution across the front edge of saltmarshes. He believed that the roughness length of the vegetation is independent of the water depth or the flow velocity, but depends only on the canopy characteristics. Folkard (2005) reported the flume investigations of flows in and around simulated patches of the Mediterranean seagrass *Posidonia oceanic* in a shallow-water environment. He considered particularly the effects of the wake of a patch on an adjacent downstream patch and found that the turbulence conditions in downstream patches can be predicted by deriving a parameterization of the wake-length scale. By imitating the same seagrass, Maltese *et al.* (2007) presented a flume study which focused on the changes in the dominant coherent turbulent structures at the patch-gap interface, and changes to the shape of the velocity profile. Bouma *et al.* (2007) combined field, flume and numerical experiments to identify spatial sedimentation and erosion patterns developing within rigid VPs and assess the relevance of hydrodynamic flume studies for the long-term sediment dynamics in the field. Ghisalberti and Nepf (2009) experimentally investigated the distinguishing hydrodynamic features of flows with rigid and flexible VP and stated that the length at which the flow is considered to be fully-developed is governed by the growth of the vortex street and the mixing-layer. Zong and Nepf (2011) described the flow structure and the spatial pattern of deposition in a finite VP at the sidewall of a channel. They reported that the flow field was self-similar when scaled with the channel velocity for different patch densities. Folkard (2011) further examined the flow regimes in gaps within stands of flexible vegetation with laboratory flume

simulations. The Reynolds number based on the canopy overflow speed and the gap depth, and the gap aspect ratio are found to be the key parameters that can be used to identify the four different flow regimes, namely skimming flow, recirculation flow, boundary layer recovery and canopy through-flow.

CFD modelling is still largely restricted to fully-developed state simulations for aquatic canopy flows, while extensive modelling works have been carried out for the flow transition regions in terrestrial canopies (Irvine *et al.* 1997; Belcher *et al.* 2003; Yang *et al.* 2006a; Yang *et al.* 2006b; Dupont and Brunet 2008; Dupont and Brunet 2009). Two pioneer studies in aquatic environment have been reported. Bouma (2007) replicated their flume and field experiments with a k–ε model. The model was found to be capable of reproducing the general features of the measured flow except for the leading edge effects. Souliotis and Prinos (2011) performed a numerical study to investigate the effect of density and length of a VP on the development of computed mean and turbulence characteristics. The computed results by the three models (two models with k–ε type turbulence closure and with Reynolds stress turbulence closure) have a similar qualitative behavior. However, the predictions of the bed shear stress along the VP by the three models differ significantly for both sparse and dense vegetations.

The present study on open-channel flow with finite flexible VP will be divided into two parts. In the first part, laboratory experiments were performed to investigate the effects of the vegetation number density and flow rate on the momentum and energy transfer along the flexible submerged VP. In particular, we shall focus on changes in the dominant coherent structures within the adjustment region and the wake region

behind the VP. In the second part, a numerical simulation of the problem using the 3D RANS model with the S-A turbulence closure will be carried out. Although many turbulence models have been extensively tested for fully-developed vegetation turbulence (e.g., S-A model, k–ε model, k–ω model and RSM model), their performances in turbulent flow over a finite VP length have not been thoroughly investigated. In particular, the performance of the S-A model has not been reported to date.

6.2. Laboratory experiments

6.2.1. Experimental set-up

Experiments were conducted in the same laboratory flume as in Chapter 5. The details about this flume can be found in 5.2.1. For this set of experiments, the bed slope was fixed at 0.25%, which is a typical for a plant covered brook. Uniform inlet conditions were achieved using a honeycomb flow straightener to eliminate swirl. The tailgate at the downstream end of the flume controlled the water depth. The experimental section was 7.9 m in the longitudinal direction and consisted one VP and two GPs (as shown in Figure 6.1). The simulated VP was 0.3 m wide (equal to the flume width), 2.4 m long, and began at 5.5 m from the flume entrance. Two GPs of 3 m and 2.5 m length, were placed at the immediate upstream and downstream ends of the VP respectively. The length of the GP at the upstream side of the VP was found to be sufficient in preliminary experiments to establish near-uniform flow approaching the VP. Both the GPs and VP were used herein to representing a natural river bed. For the coordinate system employed, x, y and z denote the longitudinal,

lateral and vertical directions, respectively. x = 0 is located at the leading edge of the VP. z denotes the vertical coordinate starting from the top of the baseboard of the VP. Figure 6.1 shows the schematic diagram of the experimental set-up. The flow field can be separated into 5 regions. They are upstream gravel-bed region, adjustment region, fully-developed region, wake region and the downstream gravel-bed region along the flow direction.

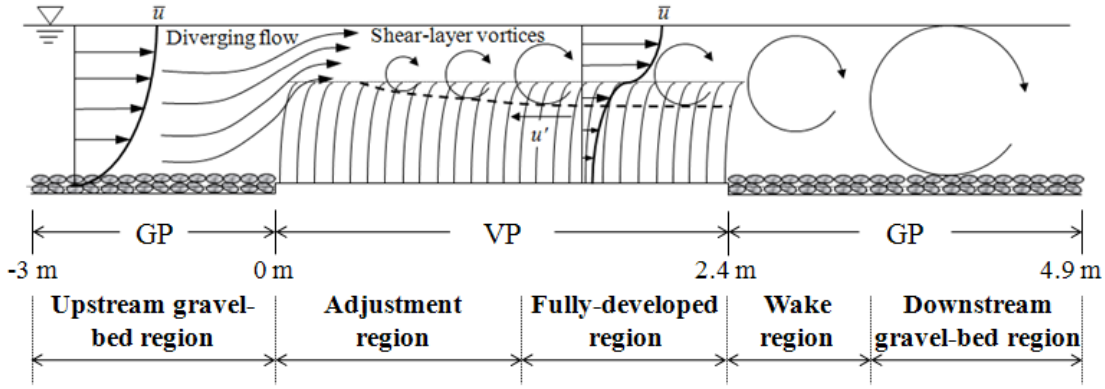

Figure 6.1. Schematic diagram of the longitudinal section of the flume

The plastic strips used to represent the flexible vegetation in this study were rectangular in cross section (as shown in Figure 6.2). The size of one vegetation element was h_v = 0.15 m height, w = 0.005 m width and t = 0.0015 m thickness. Their flexural rigidity $J \equiv E \times I_m = 4.75 \times 10^{-3}$ N/m^2, in which E = stiff modulus and I_m = inertial moment. Many previous experimental studies have used circular cylinder rods as vegetation elements (e.g., Dunn *et al.* 1996; Poggi *et al.* 2004b; Ghisalberti and Nepf 2006; Kothyari *et al.* 2009). However, the advantage of using the present plastic strip is that the vegetation model could become more flexible as the thickness is smaller. These plastic strips were held on perforated PVC baseboards

and densely distributed in parallel configuration (as shown in Figure 6.3). Two stem densities were considered in the present experimental study. For the relatively high density (HD) patch, the plant space in x and y directions (L_x and L_y) are identical and equal to 3 cm. For the low density (LD) patch, L_x and L_y are equal to 6 cm and 3 cm respectively. The density of the HD patch is twice as great as the density of the LD patch.

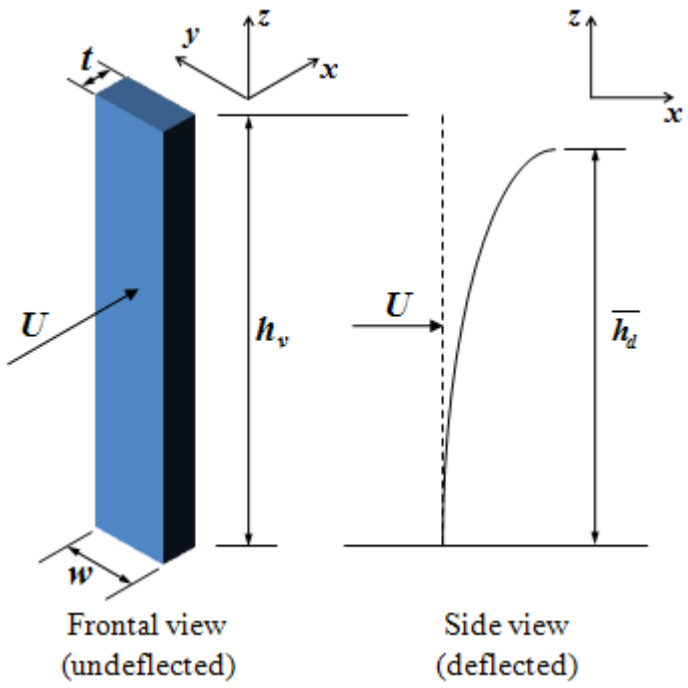

Figure 6.2. Definition of geometric characteristics of individual plastic strip

The two GPs were composed of natural gravels. These gravels are considered uniform as their size distribution is very narrow (19.0 mm ~ 25.4 mm). The median diameter (d_{50}) equals to 22.2 mm if the particle sizes are assumed to be uniform distributed in such narrow range. The thickness of these two GPs was about 35 mm. The GPs were considered fixed as no motion of the gravels was observed throughout the experiments. In the present study, the reference level is assumed to be given by h_1

= 0.20k_s, which has been confirmed in the previous experimental studies (Chapter 5). The equivalent sand roughness k_s, therefore, is given by $k_s = d_{50}$ = 22.2 mm.

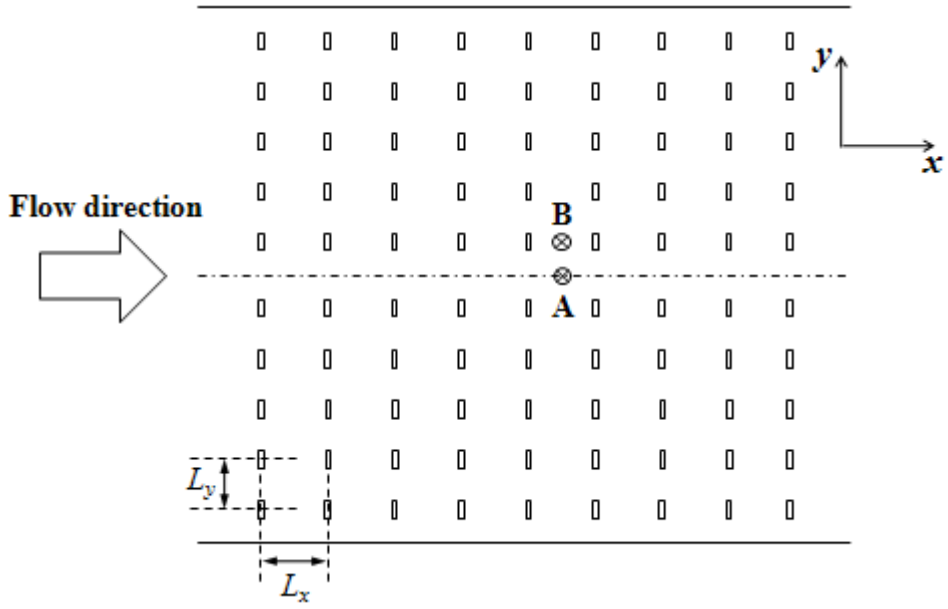

Figure 6.3. Plan view of the VP

6.2.2. Measurement techniques

6.2.2.1. Velocity measurement

The velocity measurements were undertaken by a new generation 3D acoustic Doppler velocimeter (ADV) Vectrino (NORTEK). The principle and the applications of ADV technique in the laboratory flume experiments have been reviewed in the previous chapter. The widely use of ADV in the flume measurements over gravel bed (Nikora *et al.* 2001; Ferro 2003; Rodriguez and Garcia 2008, etc.) or within the vegetation canopy (Dunn *et al.* 1996; Nepf 1999; Ghisalberti and Nepf 2006; Bouma *et al.* 2007, etc.) has indicated that this measuring instrument is reliable. Considering the sampling frequency criteria suggested by Nezu and Nakagawa (1993), turbulence

should not be sampled below 75 Hz in the flume measurements. According to Chanson *et al.* (2007), the sampling record must be larger than 5,000 samples to yield minimum errors on first and second statistical moments of the velocity components. In the present experiments, measurements at each point were taken for 120 s at 75 Hz, yielding 8,000 samples to give a good average.

The Vectrino ADV was positioned on a trolley mounted on runners at the top of the flume that facilitated accurate vertical and horizontal location. The measurements of the sample volume height provided by the ADV software can be used as a check on the positioning measured by the Vernier scale on the trolley. Previous experimental studies (Takemura and Tanaka 2007; Martino *et al.* 2011) indicated that the measuring location can be an important factor when studying the flow structure and drag characteristics of vegetated flows. In the present flume experiments, due to the size limits of the acoustic probe, all measurements had to be taken along the centerline of the flume (point A in Figure 6.3) to avoid interfering with the swaying vegetation for the cases with HD patch. For the LD patch measurements, two typical locations were chosen as the measuring locations for comparison. One is behind the plastic strip (point B in Figure 6.3), and the other is on the centre-line between two strip (point A in Figure 6.3).

Figure 6.4 shows the comparison of the mean velocity profiles and Reynolds stress profiles collected at point A and point B with the LD patch (Case 3 in Table 6.1) in the fully-developed region. It can be seen that the mean velocity profile collected at the point B is slightly smaller than that collected at point A within the vegetation canopy. The peak value of the Reynolds stress measured at point B is slightly greater

than that measured at point A. The good agreement between the measured profiles at point A and point B should be attributed to the narrow width of the plastic strips and their large density in the present laboratory study. Thus for the LD patch experiments, all measurements were also collected along the centerline of the flume. This comparison also indicates that the flow within the vegetation canopy is a skimming flow in the present study. The skimming flow was firstly identified by Morris (1955) and referred to the flows in which the wakes are unable to form in the gaps between the roughness elements when these roughness elements were densely packed.

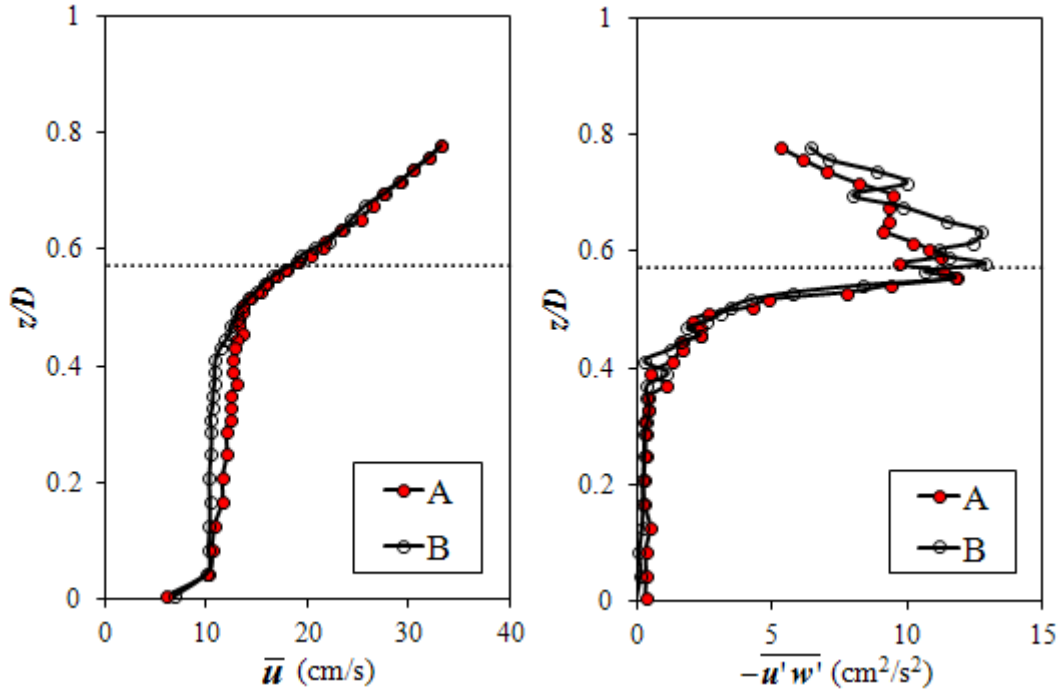

(a) Mean velocity (b) Reynolds stress

Figure 6.4. Measured profiles of mean velocity and Reynolds stress in point A & point B at x = 1.63 m for Case 3 in Table 6.1

(The dot line denotes canopy height)

In order to accurately obtain the maximum shear stress at each location, at least 32

point measurements were conducted at different vertical positions. The previous experimental studies have indicated that the peak Reynolds shear stress occurs at the deflected height for the fully-developed open-channel flow with submerged flexible VP. As there is a distance of 5 cm between the ADV probe and its sampling volume, the uppermost 5 cm layer of the flow cannot be sampled. Therefore, when designing the experimental conditions, we should ensure that the water depth is 5 cm higher than the undeflected canopy height to capture the maximum Reynolds stress within the VP.

Due to the well-known fact that with the increasing particle concentration in water the data quality measured by ADV remarkably increases, special attention was given to provide particle-rich environment in water to increase the data quality. Furthermore, the raw data collected from flume measurements were processed by applying a threshold greater than 70% to the signal-correlation time series and the phase-space thresholding method (Goring and Nikora 2002) to remove high-frequency Doppler noise. As a result, at least 90% of samples were retained in most time series, although in some this fraction was considerably lower.

6.2.2.2. Water depth measurement

A point gauge, which was positioned on another trolley at the top of the flume, was used to measure the water depth. The water depth was measured every 10 cm from x = -2.0 m to x = 4.4 m, covering most of the experimental section. In addition, water depth was measured along the channel centerline only, since the transverse variations of the water surface were too small to be measured accurately.

6.2.3. Experimental results and discussion

6.2.3.1. Test conditions

Table 6.1 summarizes the three experimental conditions employed in the flume experiments. The water depth D and the cross-section averaged velocity $\bar{U}$ in the table were measured at the leading edge of VP (x = 0 m). The Froude number, $\mathrm{Fr} = \bar{U}/(gD)^{0.5}$ and Reynolds number, $\mathrm{Re} = \bar{U} \cdot D/\nu$, where g = gravitational acceleration; ν_m = kinematic molecular viscosity, were computed using the measured D and $\bar{U}$ at the leading edge location. The flow was subcritical and fully turbulent for all cases. It is noteworthy that the Case 1 & 2 have the same upstream flow condition and thus the same Fr and Re. Case 1 was with the HD patch (α = 5.56) and Case 2 was with the LD patch (α = 2.78). Case 3 was a low-Re case (Re = 27,643) with the HD patch, in contrast to Case 1 (Re = 44,812).

Due to the finite length of the VP, the water flow cannot be uniform around the patch. Figure 6.5 shows the variation of the water surface for the three cases listed in Table 6.1. The presence of VP induces fluctuations of the water surface not only in the downstream region, but also the upstream region of the VP. This phenomenon indicates that the flow region under consideration in this study is always nonuniform even though its upstream or downstream region might have uniform flow. It can be also seen from the comparison of the profiles between the Case 1 and Case 2 that the denser VP results in a steeper water surface slope due to the stronger resistance effect.

Table 6.1. Summary of experimental conditions

Case	Q [m^3/hr]	D [m]	$\bar{U}$ [m/s]	W/D	α [m^{-1}]	$\overline{h_d}$ [m]	Fr	Re
1	50.01	0.246	0.182	1.26	5.56	0.145	0.117	44,812
2	50.01	0.246	0.182	1.26	2.78	0.141	0.117	44,812
3	30.85	0.21	0.132	1.48	5.56	0.147	0.092	27,643

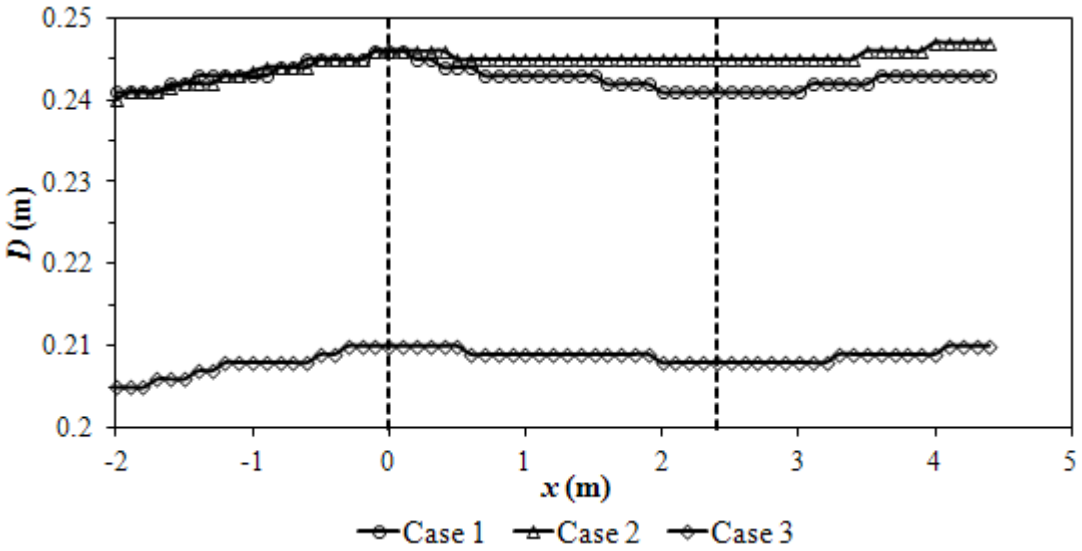

Figure 6.5. Measured water surface elevation profiles

Visualization experiments were also performed by injecting a fluorescent dye solution (Red Rhodamine) at several vertical layers. A digital video camera was used to record the flow visualization and the motion of the plastic strips. Photo 6.1 shows an experimental evidence of K-H vortices in flows over vegetation canopy. The vortex, outlined by the dot circle, is displaced upwards relative to the top of the canopy. These vortices, in both terrestrial and aquatic canopy flows, dominate the exchange of mass and momentum between the canopy and the overlying flow (Finnigan 2000; Ghisalberti and Nepf 2005; Nepf and Ghisalberti 2008; Nezu and Sanjou 2008). Throughout the experimental period, the simulated plants were found to be deflected (as shown in Photo 6.1) and swaying. Because Ghisalberti and Nepf's

mixing layer theory (Ghisalberti and Nepf 2002) requires an extended free shear for K-H instabilities to grow, the lack of *monami* in the present laboratory observations can be seen as a corroboration of this theory. In the fully-developed region, the plants appeared to be gently swaying without organized motion. The plants were more deflected and violently swayed at the leading and trailing edges. While the plants only swayed in the longitudinal direction in the fully-developed region, the plants swayed and vibrated in both the longitudinal and transverse directions at the leading and trailing edges. As the bending degree of plants was different along the patch length, the time-averaged deflected height in the fully-developed region was chosen to represent the canopy height for simplicity. The time-averaged deflected height, $\overline{h_d}$, are included in Table 6.1 for all these three cases. It can be seen that in the present study the bending degree of the plastic strips are small in the fully-developed region which attributes to their large flexural rigidity ($J = 4.75 \times 10^{-3}$ N/m^2). Lower vegetation density or higher Reynolds number leads to a smaller $\overline{h_d}$.

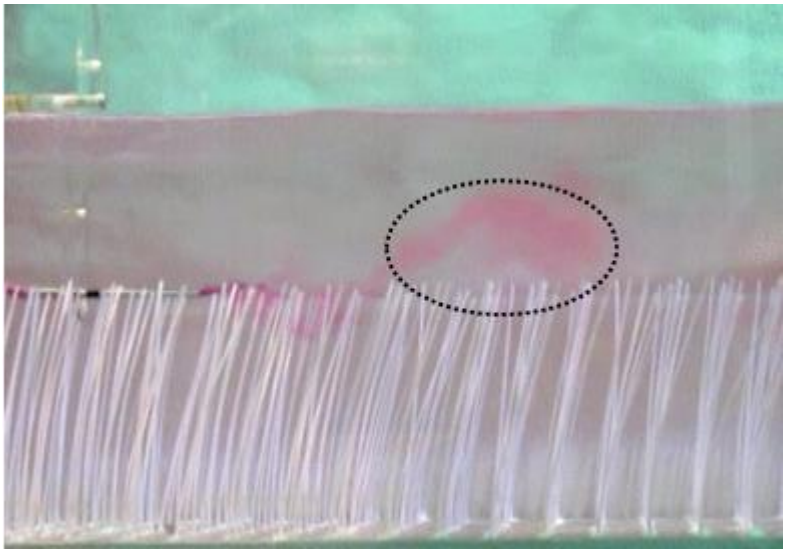

Photo 6.1. A K-H vortex above the flexible vegetation canopy is visualized using red dye for Case 1 in Table 6.1

6.2.3.2. Mean flow measurement results

The primary objective of this study is to investigate the response of mean velocity and turbulence to the presence of finite and flexible VP in a gravel-bed open-channel flow. Therefore, the research focus was limited in the adjustment region, fully-developed region and wake region (as shown in Figure 6.1). The experimental measurements within these three regions will be demonstrated and discussed separately below.

Adjustment region

The adjustment of the mean velocity downstream of the leading edge was found similar for all the cases. The flume measurements of Case 1 were taken as an example to show the variations of mean velocity components in this region. The contour plot of the mean velocities in the streamwise and vertical directions is shown in Figure 6.6. The two-dimensional (2D) velocity vectors were also plotted to show the values and directions of mean velocity at each measurement point. It can be seen from this figure that downstream of the leading edge, the streamwise velocities decelerated progressively within the vegetation canopy and accelerated above it (development of skimming flow). The reduction of streamwise velocity within the vegetation canopy was always accompanied by vertical flow to maintain the water flux, i.e., a part of the water reaching the canopy was slowed down, but the major part was deflected upwards (as shown in Figure 6.6b). The vertical position of the maximum velocity gradient moved upwards with the greater distance from the leading edge.

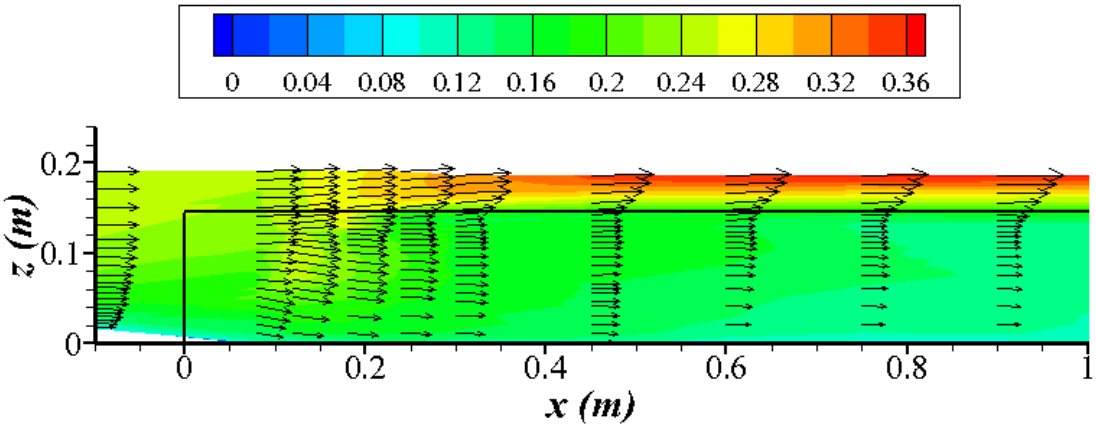

(a) Mean streamwise velocity $\bar{u}$ (m/s)

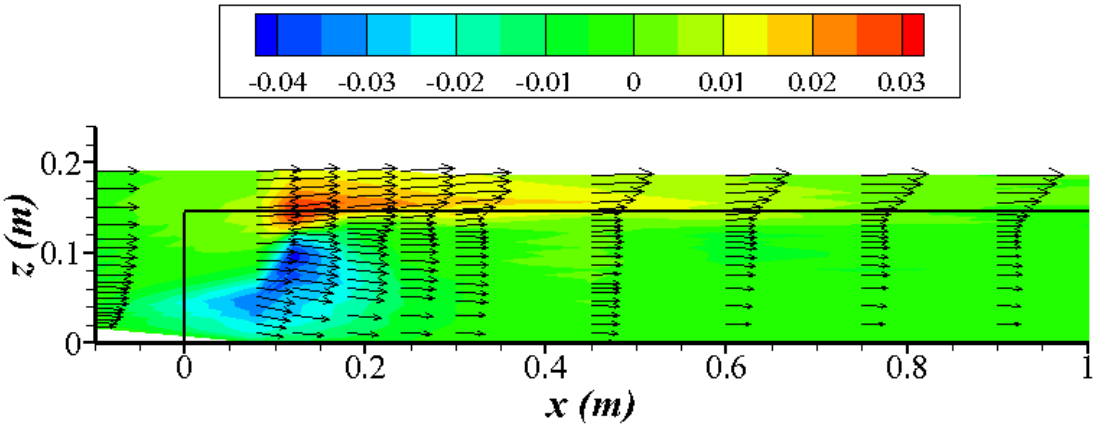

(b) Mean vertical velocity $\bar{w}$ (m/s)

Figure 6.6. Contour plots of the mean velocity components $\bar{u}$ and $\bar{w}$ (m/s) within adjustment region for Case 1 in Table 6.1

(The rectangle indicates the location of the VP)

Fully-developed region

With submerged VP, a skimming flow developed immediately downstream of the leading edge (Bouma *et al.* 2007; Neumeier 2007). After a certain distance for adjustment, the mean velocity profiles become uniform. This distance is called adjustment length (x_a). As shown in Figure 6.7, at a downstream distance of 1.65 m

and 1.99 m from the leading edge, the mean velocity profiles become uniform for Case 1 and Case 2, respectively. The values of x_a for all the three cases are listed in Table 6.2. The x_a appears to be dependent on the vegetation density and Reynolds number. A higher vegetation density or smaller Re leads to a smaller x_a. It can be seen from Figure 6.7, an inflection point was generated in each mean velocity profiles for Case 1 and Case 2.

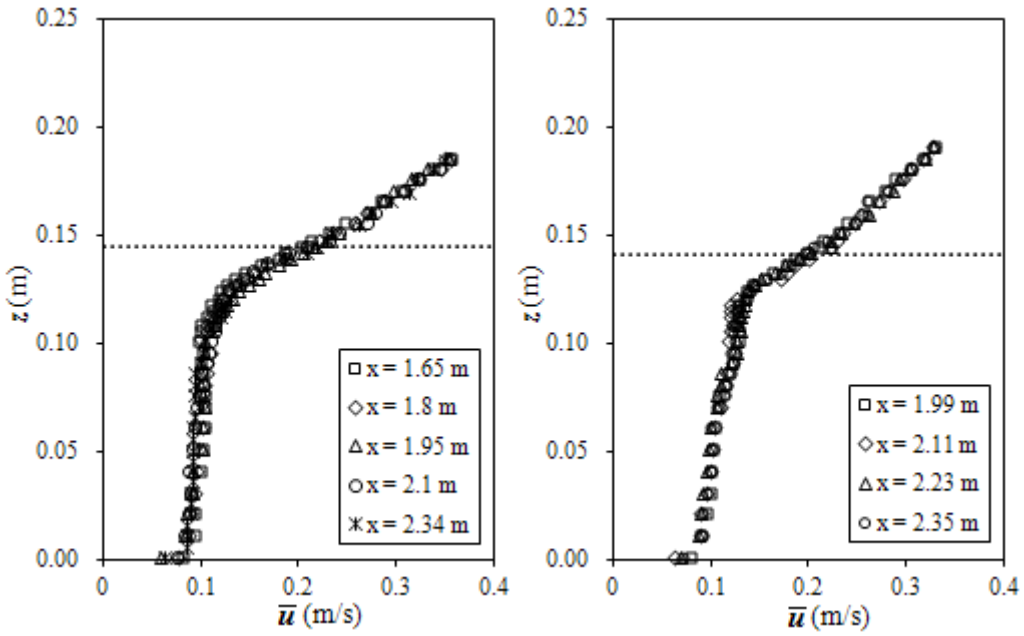

Case 1 in Table 6.1 Case 2 in Table 6.1

Figure 6.7. Streamwise mean velocity profiles measured within the fully-developed region

(The dot line denotes the canopy height)

Table 6.2. Values of x_a for experimental conditions

	Case 1	Case 2	Case 3
x_a (m)	1.65	1.99	1.5

Figure 6.8 shows the comparisons of the double-averaged (in time and spatial domains) velocity profiles within the fully-developed region. It can be found from the comparison that the decrease in vegetation density leads to greater mean velocities within the canopy layer, and smaller mean velocities in the upper layer. In other words, the increasing canopy density leads to the increasing inflection in the mean velocity profile.

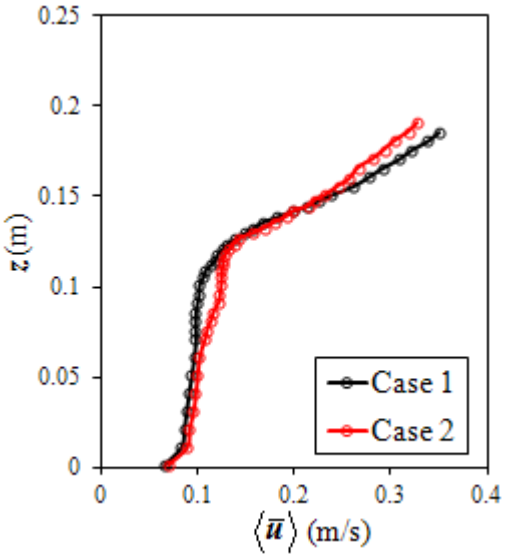

Figure 6.8. Comparison of DA velocity profiles within fully-developed region between Case 1 & Case 2

Wake region

Figure 6.9 shows the contour plots of the streamwise mean velocity in the vicinity of the trailing edge for Case 1 and Case 2. The canopy resistance suddenly disappears downstream the trailing edge, which causes a gradual change of the vertical profile of the velocity along the longitudinal direction. Thus the high flow in the upper layer tends to move downward and reattach with the gravel bed. The hydrodynamic

characteristics in this area have strong similarities with those of a mixing layer and a reattached mixing layer in backward-facing step flow. A low-velocity region is found behind the trailing edge. It can be seen from the comparison of the results between Case 1 and Case 2 that the increase in the vegetation density leads to lower velocities behind the trailing edge. Due to the highly porosity of the VP, no recirculation zone was found according to the flume measurements.

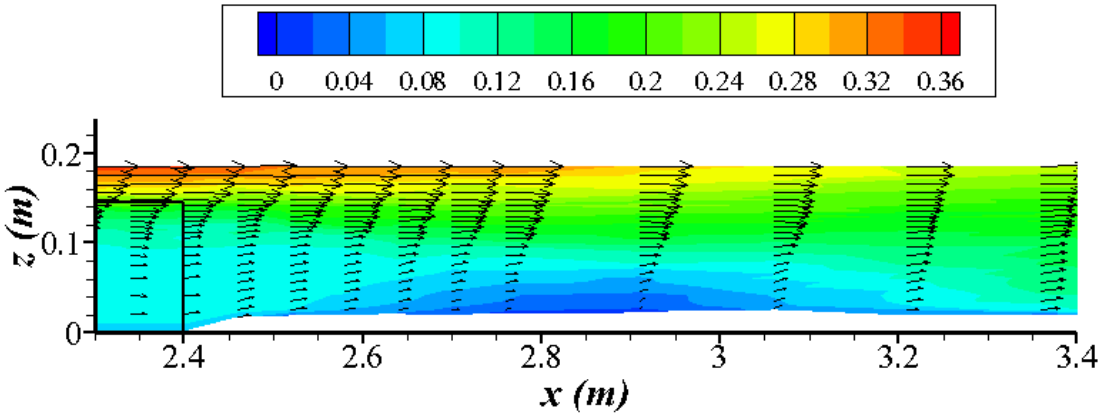

(a) Case 1 in Table 6.1

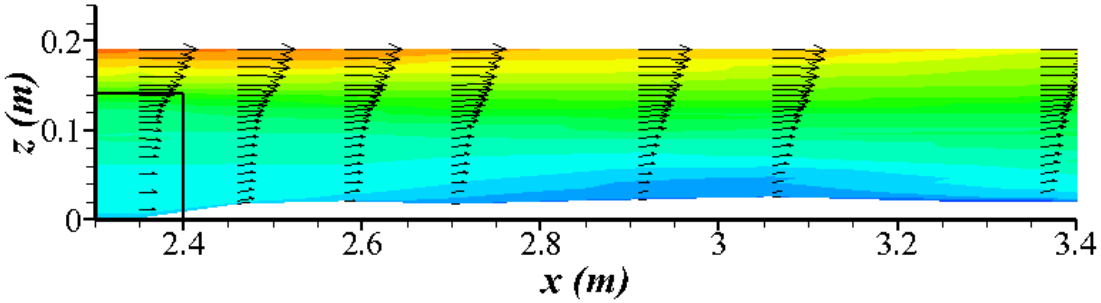

(b) Case 2 in Table 6.1

Figure 6.9. Contour plots of the streamwise mean velocity $\bar{u}$ (m/s) within wake region

(The rectangle indicates the location of the VP)

6.2.3.3. Turbulence measurement results

As expected, the flexible plants had evident effects on the turbulence structure within and above the VP, which correspond closely with the measurements made by Neumeier (2007).

Adjustment region

For the turbulence analysis, the Reynolds stress $-\overline{u'w'}$ (per unit mass) and the turbulence kinetic energy (TKE) k (per unit mass) were computed from the measured instantaneous velocities. Figure 6.10 shows the contour plot of $-\overline{u'w'}$ within the adjustment region for Case 1 and Case 2. In a Cartesian co-ordinate system the positive value of $-\overline{u'w'}$ indicates the momentum flux transports towards the bed which is the predominant situation in a wall-bounded flow. This quantity is of great engineering interest as it reflects the sedimentation and erosion processes of open-channel flows. Negative values of $-\overline{u'w'}$ can be identified at the top of the VP near the leading edge for both Case 1 and Case 2, indicating the flow momentum transports upwards into the upper layer. In all other areas beyond the leading edge, however, this quantity appears to be positive, suggesting the momentum flux transports towards the sediment bed. The values of the Reynolds stress are generally low inside the VP because of the small velocity gradient. A high level of this quantity can be only measured at the very frontal part of the patch which indicates a higher sediment deposition would occur in this region. This high-level area is greater in Case 1 with HD patch. This phenomena are in fair agreement with the field observations by Bouma *et al.* (2007).

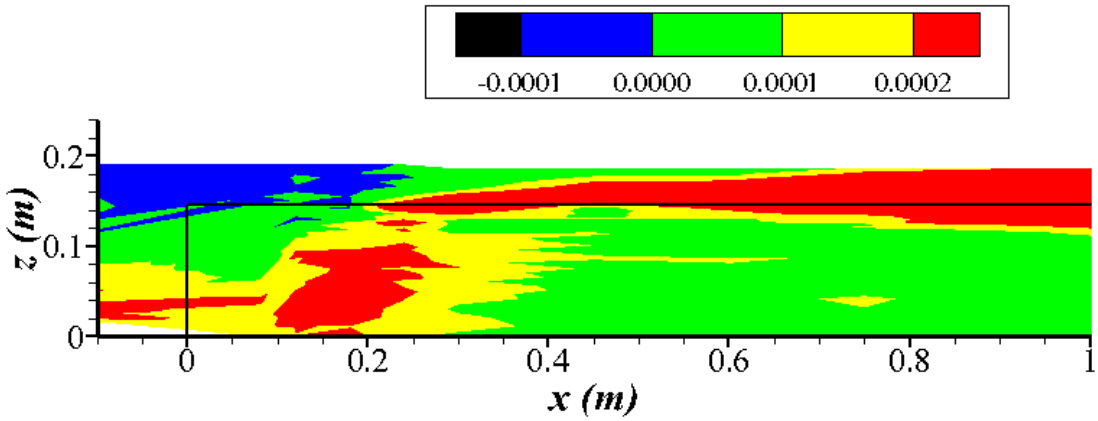

(a) Case 1 in Table 6.1

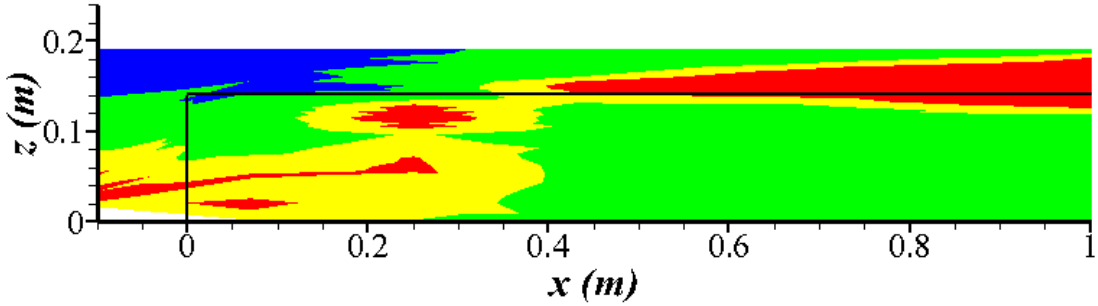

(b) Case 2 in Table 6.1

Figure 6.10. Contour plots of measured Reynolds stress per unit mass $-\overline{u'w'}$ (m^2/s^2) within adjustment region

(The rectangle indicates the location of the VP)

Figure 6.11 shows the contour plot of *k* within the adjustment region for Case 1 and Case 2. It can be seen that, for both open-channel flows with HD and LD patch (Case 1 and Case 2), a significant increase in turbulence (TKE) occurs within the upstream area of the VP with longitudinal length 50 cm. The TKE then decreases further downstream. This is in good agreement with the flume observations by Neumeier (2007), but inconsistent with the statement by Bouma *et al.* (2007). Bouma *et al.* (2007) performed flume experiments with open-channel flows with submerged bamboo patch. They found that the highest level of *k* was generated at the leading

edge of VP. This difference can be attributed to the stem flexibility of the simulated plants. As the flexible plants were employed in the present study, 2 ~ 3 rows of these plants beyond the leading edge appear to be deflected more and violently vibrated. These motions would dissipate part of the TKE at the leading edge and result in the downstream movement of the high-level TKE region. Beyond this high-level region, the position of the turbulence maximum moved upwards with the downstream distance from the leading edge, corresponding to the upward shift of the maximum velocity gradient. According to the comparison of the results between Case 1 and Case 2, it also can be concluded that a denser VP leads to a higher TKE level inside the patch within the adjustment region.

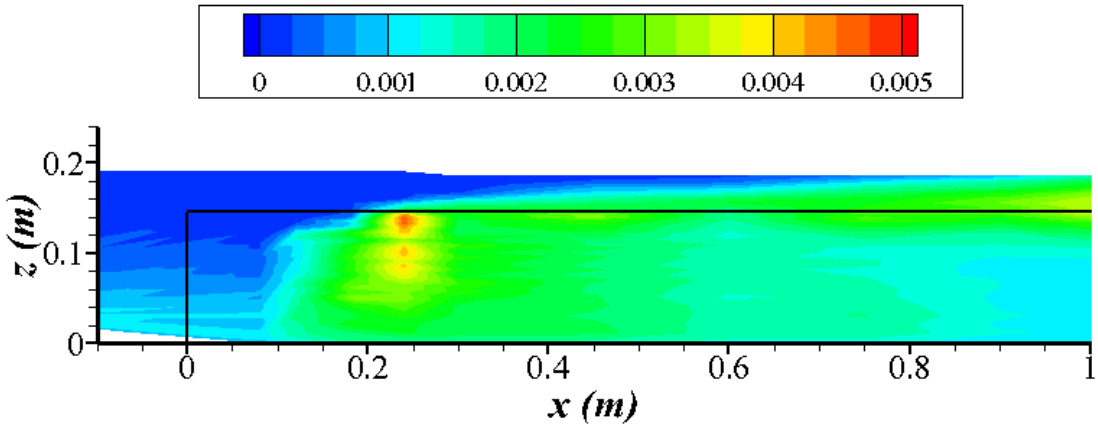

(a) Case 1 in Table 6.1

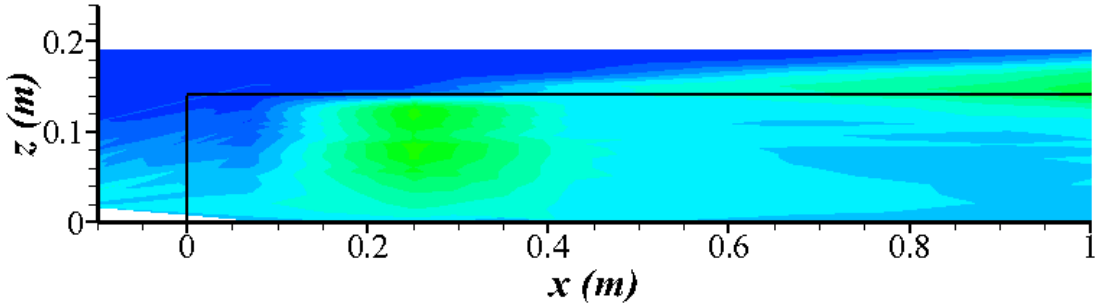

(b) Case 2 in Table 6.1

Figure 6.11. Contour plots of measured TKE per unit mass k (m^2/s^2) within adjustment region

Fully-developed region

Figure 6.12 shows the vertical profiles of the measured $-\overline{u'w'}$ within the fully-developed region for Case 1 and Case 2. The profiles at different streamwise locations all follow the typical distribution of vegetated flows. The values of the Reynolds stress reach the peak value at the time-averaged deflected height. While the values remain nearly constant inside the canopy, the values increase with the downstream distance from the leading edge in the upper layer. The height, at which the Reynolds stress decays to 10% of its peak value, is regarded as the penetration depth suggested by Nepf and Vivoni (2000). Based on the flume measurements, the penetration depth is 0.11 m for Case 1 and 0.1 m for Case 2, approximately. The decrease in vegetation density leads to the decrease in the penetration depth.

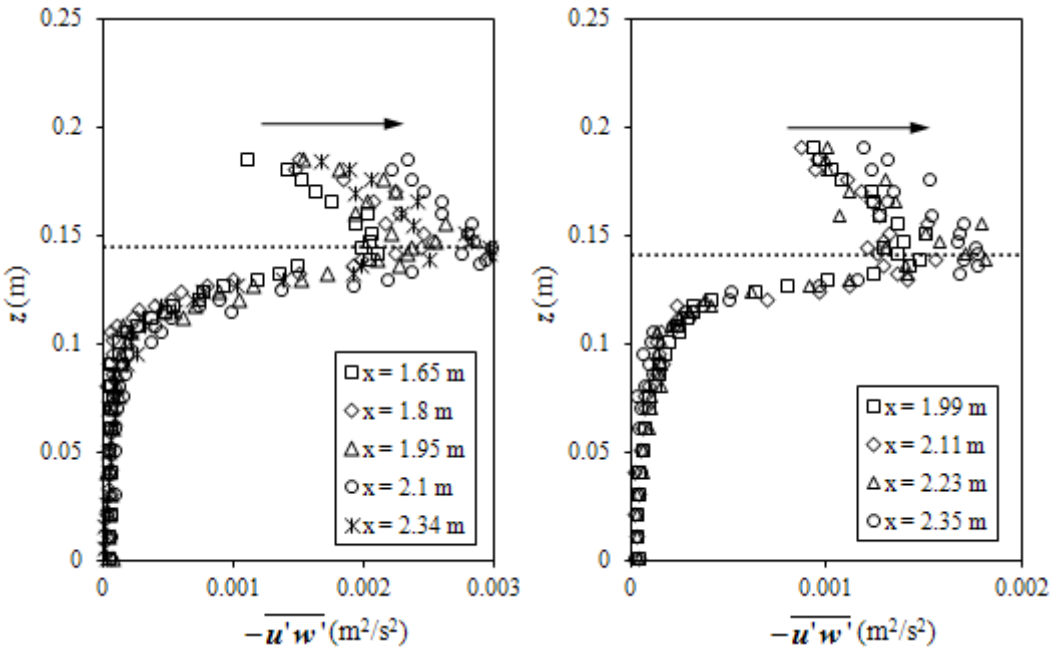

Case 1 in Table 6.1 Case 2 in Table 6.1

Figure 6.12. Vertical distribution of measured Reynolds stress

(The dot line denotes the canopy height)

Figure 6.13 shows the vertical profiles of measured k within fully-developed region for Case 1 and Case 2. They show great similarities with the profiles of Reynolds stress. Both cases show peak values of TKE at the time-averaged deflected height. Due to the damping effect of the VP, the values of TKE were reduced significantly inside the patch and reach a nearly constant minimum below the penetration depth. In the upper layer, the TKE gets increased with the downstream distance from the leading edge. According to the comparison between the Case 1 and Case 2, it can be found that the values of TKE are nearly identical with α = 5.56 and 2.78 below the penetration depth. Above the penetration depth, the decrease in the vegetation density leads to the decrease of TKE.

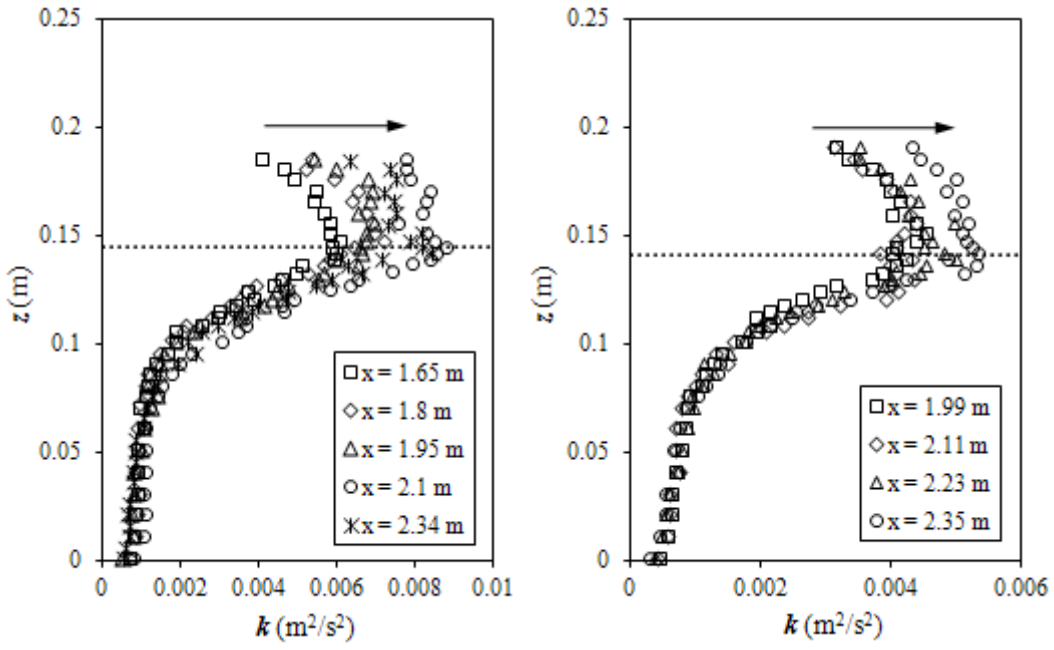

Case 1 in Table 6.1 Case 2 in Table 6.1

Figure 6.13. Vertical distribution of measured TKE per unit mass k

(The dot line denotes the canopy height)

Wake region

Figure 6.14 shows the maxima of the measured $-\overline{u'w'}$ throughout the whole testing area for all the three cases. It can be seen that the values of the Reynolds stress, within the open-channel flows with VP, increase monotonically from the leading edge to the trailing edge, and then decrease monotonically beyond the trailing edge. At a sufficient distance further downstream, the value of the Reynolds stress reduces to the same level measured in the upstream of leading edge. The decrease in the vegetation density (Case 2) or the upstream Reynolds number (Case 3) leads to the smaller values of Reynolds stress beyond the leading edge. Although for these two cases the two distributions of the maximum Reynolds stress value are similar, the effects of reduction in vegetation density and reduction in Reynolds number cannot be the same. The dependence of the maximum Reynolds stress on these two parameters has to be further studied.

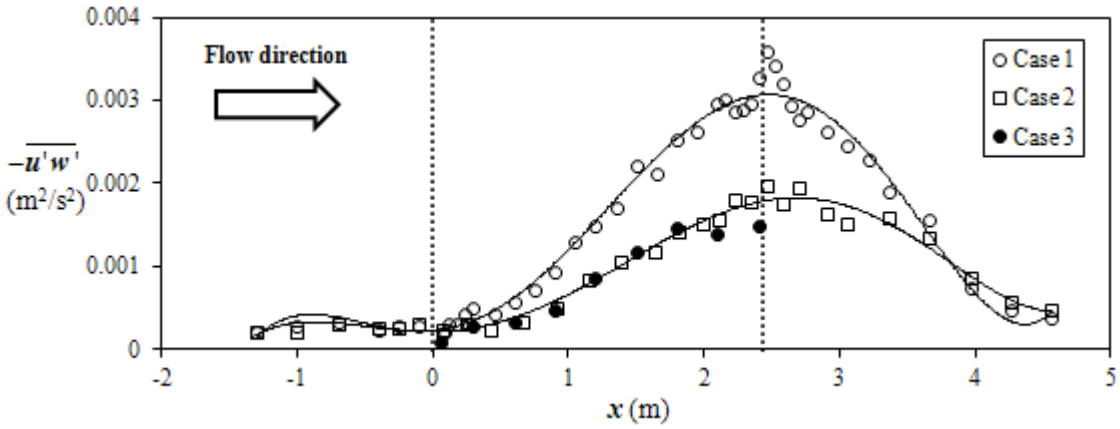

Figure 6.14. Maxima of measured Reynolds stress per unit mass $-\overline{u'w'}$ along the flow direction

(The dot lines, on the left and right, denote the leading edge and trailing edge, respectively)

Figure 6.15 shows the contour plots of the measured *k* within the wake region for Case 1 and Case 2. It can be seen that for these two cases the highest level of the TKE occur at the top of the trailing edge. Beyond the trailing edge, the TKE is dissipated and its peak value shifts slightly downwards. A denser VP also produces a higher level of TKE within this region.

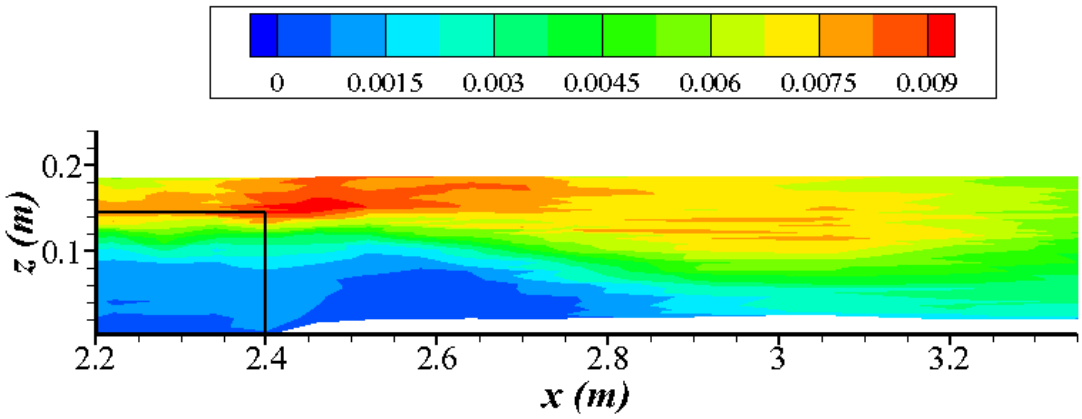

(a) Case 1 in Table 6.1

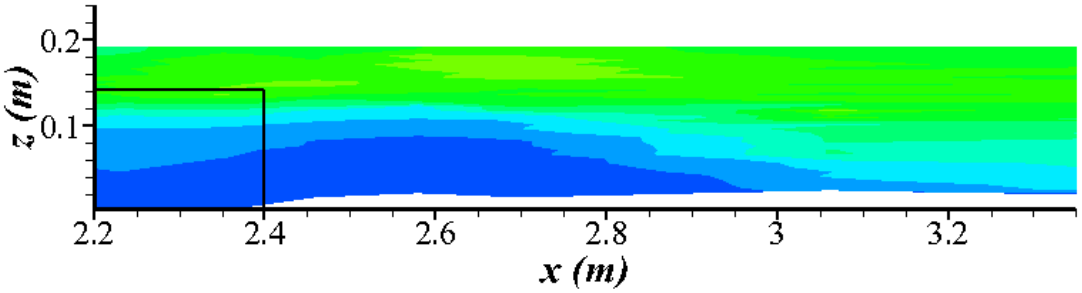

(b) Case 2 in Table 6.1

Figure 6.15. Contour plots of measured TKE per unit mass *k* (m^2/s^2) within wake region

(The rectangle indicates the location of the VP)

6.2.3.4. Quadrant analysis

The conventional quadrant analysis of the instantaneous *u* and *w* velocity signals allows a quantitative understanding and description of the turbulence structure. The method was developed by Lu and Willmarth (1973) and Luchik and Tiederman (1987) and based on the joint distribution of the streamwise and vertical velocity fluctuations (*u*' and *w*' respectively). It has been widely used in the last decade to illustrate changes in turbulent flow fields above different bed surfaces (Robert *et al.* 1996; Buffin-Belanger and Roy 1998; Poggi *et al.* 2004b; Pokrajac *et al.* 2007; Hardy *et al.* 2009). As shown in Figure 6.16, four distinct quadrants can be defined (Q_i stands for the event associated with quadrant *i*). For each quadrant, the quadrant Reynolds stress RS_i can be defined as follows:

$$RS_i = \left(\overline{u'w'}\right)^{-1} \lim_{T\to\infty} \frac{1}{T}\int_0^T u'(t)\cdot w'(t) I_i(t)dt \quad \left(i = 1,2,3\ and\ 4\right) \tag{6-1}$$

where $I_i(t) = 1$ when the (u', w') exists in quadrant *i*, and otherwise $I_i(t) = 0$; *i* is the quadrant number and *T* is the total record length. RS_i represents the contribution rate of each event to the Reynolds stress. The sum of these four components equals to 1.

Quadrant contributions and time scale of quadrant events can be evaluated for various threshold values. Threshold values are defined by the hole size (*H*):

$$H = \frac{\left|u'w'\right|}{u_{rms}w_{rms}} \tag{6-2}$$

where u_{rms} and w_{rms} are the root-mean-square value of *u* and *w* velocity components, respectively. In order to characterize low- and high-magnitude events, arbitrary threshold values of 0 and 2 are used. $H = 0$ means that all events within a quadrant

are considered whereas H = 2 means that only high-magnitude events in terms of shear stress production are considered. The value of 2 is often used to analyze the bursting phenomena in rough-bed open-channel flows (e.g., Bennett and Best 1995; Buffin-Belanger and Roy 1998). However, Nezu and Sanjou (2008) argued that such a threshold level may not be necessary to analyze coherent motions in canopy flows as the contribution of low-magnitude events is significantly small.

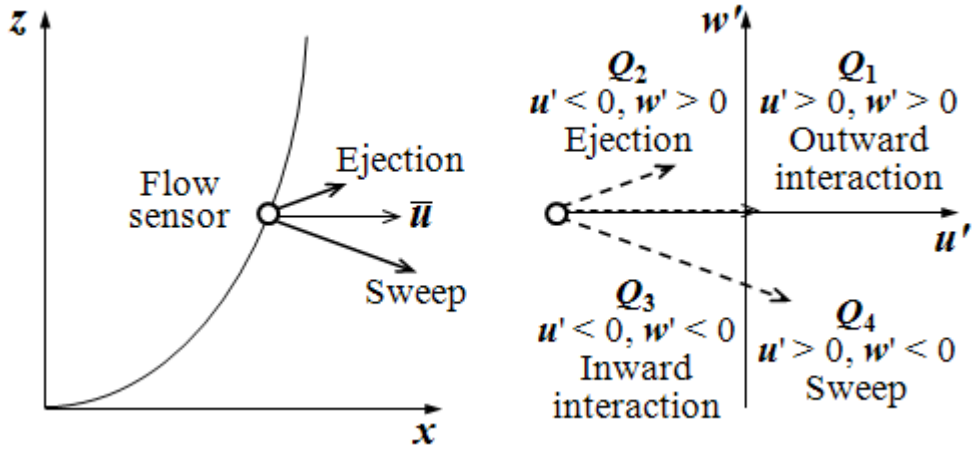

Figure 6.16. Quadrant diagram of downstream (u') and vertical (w') turbulent flow components (after Robert *et al.* 1993)

Of the four quadrant events, Q_2 events (ejections) and Q_4 events (sweeps) are mostly interested in experimental observations, since they contribute positively to the shear stress and the strong sweep events are also critical in the mechanisms of sediment transportation. In the following, an attempt was made to relate the flume measurements to the dominant coherent structures using the quadrant analysis.

Adjustment region

The contour maps of the Ejection-to-sweep ratio (RS_2/RS_4) are shown in Figure 6.17 within the adjustment region for Case 1 and Case 2. This ratio is useful to identify whether ejections or sweeps of coherent structures are more predominant. From this figure, it can be seen that the adjustment region is dominated by the ejection events ($RS_2/RS_4 > 1$). The high-magnitude Q_2 events ($RS_2/RS_4 > 1.4$) occur at the leading edge, suggesting the presence of stronger coherent vertical motions associated with upwelling motions of flow at the upstream side of the VP.

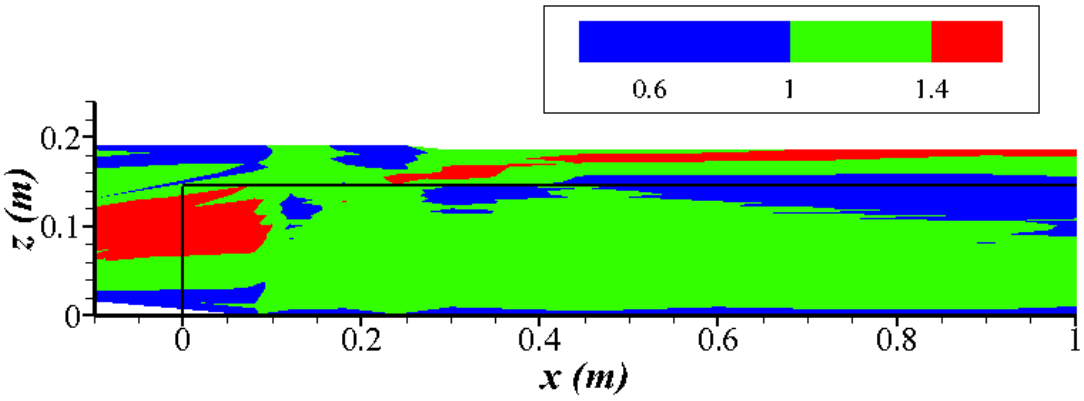

(a) Case 1 in Table 6.1

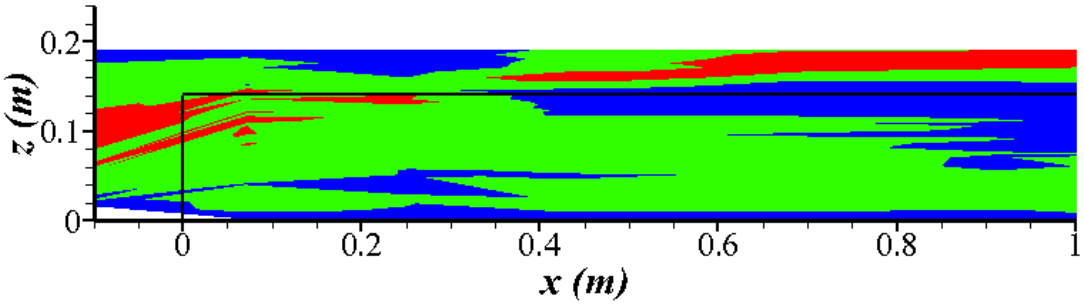

(b) Case 2 in Table 6.1

Figure 6.17. Contour maps of the ratio of time contribution from Q_2 and Q_4 (RS_2/RS_4) within the adjustment region

Fully-developed region

Base on the mixing layer analogy, Ghisalberti and Nepf (2006) separated the canopy layer into the exchange zone and the wake zone; the boundary between the two layers is at z_1 where Reynolds stress just decays to zero. The shear layer extends from z_1 to z_2 (where the velocity gradient is approximately zero). Thus the shear layer comprises two layers. One is the exchange zone, the other one between ($\overline{h_d} < z < z_2$) is termed the "upper shear layer". Because the uppermost 5 cm layer of the flow cannot be measured by using the ADV, the flow layer above the shear layer will not be taken into consideration in the present study.

Figure 6.18 shows the vertical profiles of the quadrant Reynolds stress RS_i within the fully-developed region for Case 1 and Case 2. It is found that the outward and inward interactions (RS_1 and RS_3) become much smaller than RS_2 and RS_4 near the vegetation tips. This strongly indicates that the ejections and sweeps near the vegetation tips are more organized motions which do not almost contain the less-organized motions, such as the outward and inward interactions. The values of RS_2 and RS_4 within the VP for Case 1 are found to be larger than those for Case 2 which indicate a stronger organized motion in the canopy layer with denser patch.

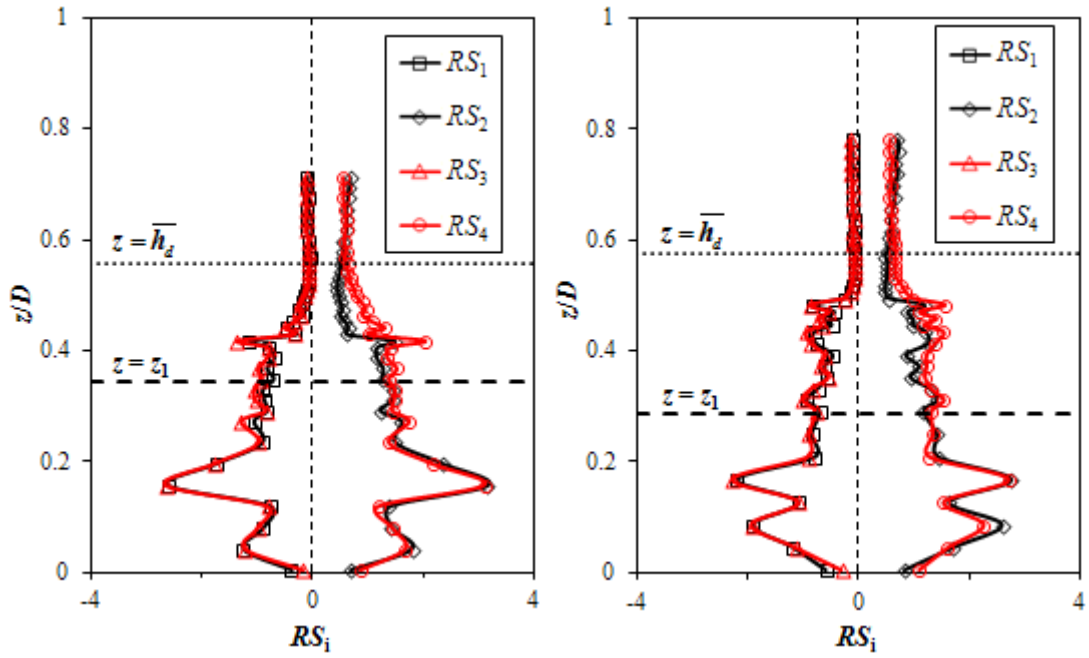

Profile at x = 1.95 m in Case 1 Profile at x = 2.11 m in Case 2

Figure 6.18. Vertical distributions of quadrant Reynolds stress RS_i within the fully-developed region

(The dot line denotes the time-averaged deflected height; the dash line denotes the lower limit of the exchange zone)

Figure 6.19 shows the vertical variations of Ejection-to-sweep ratio (RS_2/RS_4) within the fully-developed region for Case 1 and Case 2. As the shear layer is dominated by a street of coherent K-H type vortex structures (as shown in Photo 6.1), the Q_2 events (ejections) and the Q_4 events (sweeps) appear to be dominant in the upper shear layer and the exchange zone, respectively. The Ejection-to-sweep ratio is close to unity below z_1 because the wake zone is dominated by stem wakes and without the coherent large-scale eddies.

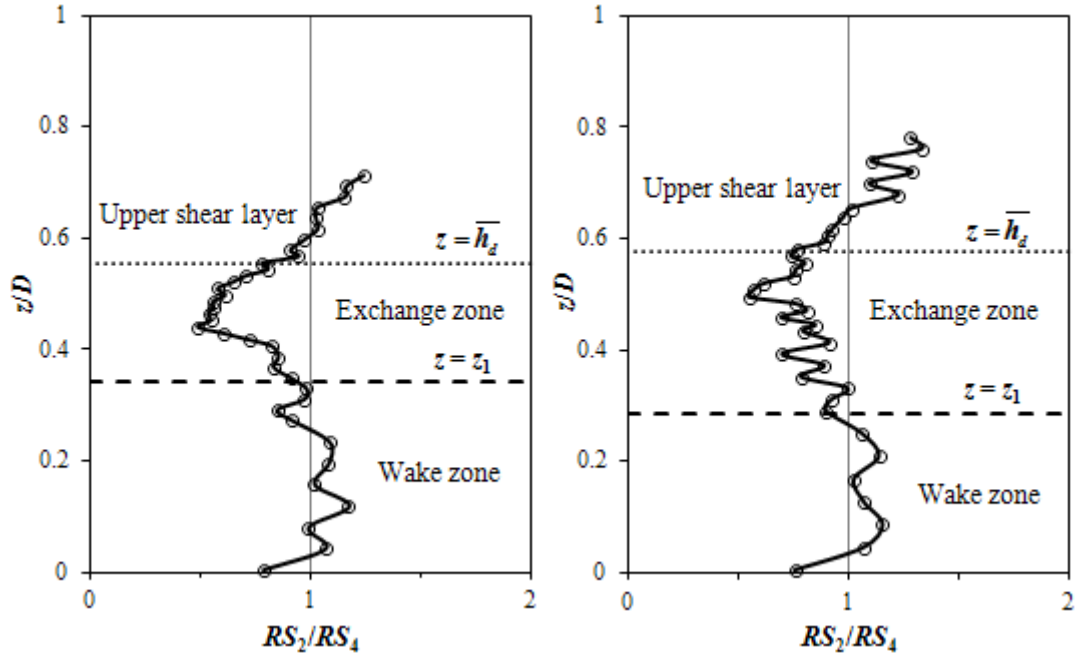

Profile at x = 1.95 m in Case 1 Profile at x = 2.11 m in Case 2

Figure 6.19. Vertical distributions of Ejection-to-sweep ratio (RS_2/RS_4) within fully-developed region

Figure 6.20 presents the scatter plots of u'/u^* against w'/u^* in the three layers within the fully-developed region (x = 1.95 m) for Case 1. Figure 6.20(a-c) depicts the fluctuating velocity components (u', w') in the upper layer (z/D = 0.713), exchange zone (z/D = 0.521) and wake zone (z/D = 0.195), respectively. The fluctuating velocity components (u', w') were nondimensionalized by the shear velocity u^*.

In the present study, the shear velocity is defined as the square root of the maximum in a Reynolds stress (per unit mass) profile. That is,

$$u^* = \sqrt{(-\overline{u'w'})_{\max}} \tag{6-3}$$

The maximum Reynolds stress is expected to occur at the time-averaged deflected height for a flexible canopy.

The scatter plots in Figure 6.20(a & b) show that a long tail stretches towards the second quadrant (ejection events) in the upper shear layer and fourth quadrant (sweep events) in the exchange zone, respectively. This is in good agreement with the previous analysis that the ejections and sweeps are dominant in the upper layer and the exchange zone. In these two layers (upper shear layer and exchange zone) the number of Q_2 events (ejections) and Q_4 events (sweeps) are significantly larger than those of Q_1 events (outward interactions) and Q_3 events (inward interactions), which also indicates that the organized motions (K-H vortices) are dominant in the upper shear layer and exchange zone. In the wake zone (as shown in Figure 6.20(c)), however, these four quadrant events are nearly of equal weightings. This suggests that the organized motions are vanished in the lowest layer.

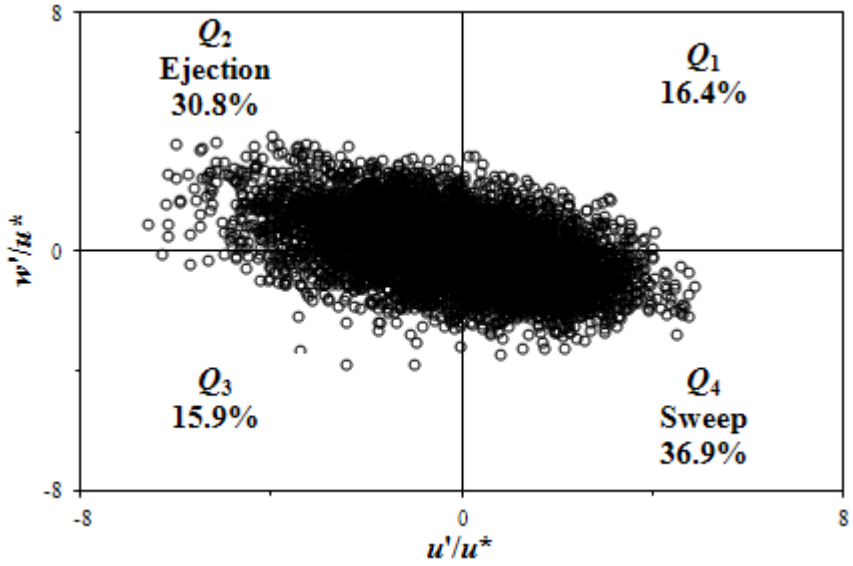

(a) Upper layer (z/D = 0.521)

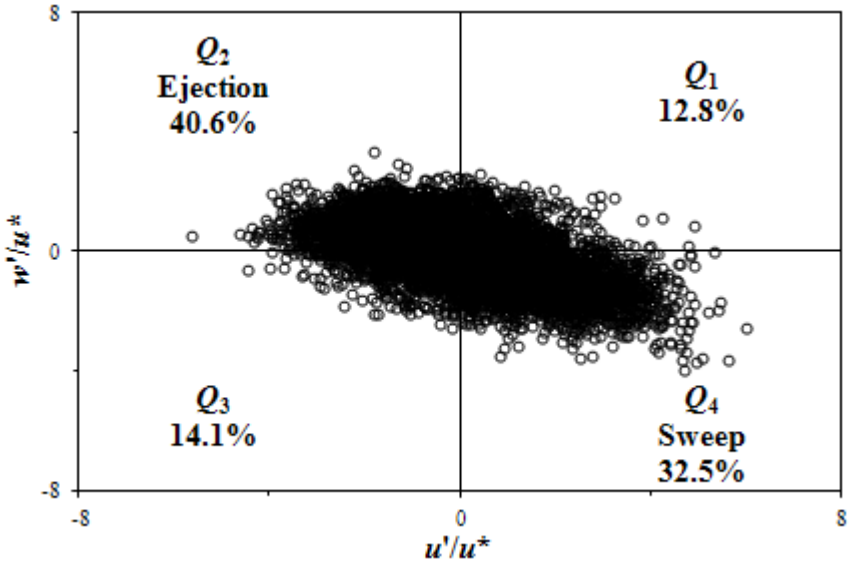

(b) Exchange zone (z/D = 0.521)

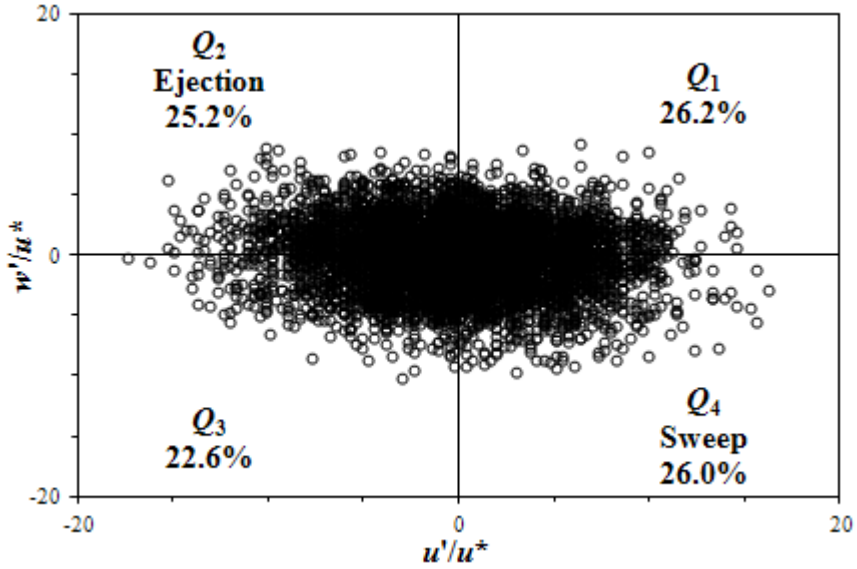

(c) Wake zone (z/D = 0.195)

Figure 6.20. Scatter plots of u'/u^* against w'/u^* in different layers within fully-developed region for Case 1

Wake region

Figure 6.21 shows the contour maps of the Ejection-to-sweep ratio (RS_2/RS_4) within the wake region for Case 1 and Case 2. It was found that the wake region is dominated by the sweep events (RS_2/RS_4 < 1). The high-magnitude Q_4 events (RS_2/RS_4 < 0.6) occur near the trailing edge of VP, indicating the presence of stronger coherent vertical motions associated with shedding motions of the flow beyond the VP. Higher level of the Q_4 events is observed downstream of the denser patch (Case 1) which indicates a stronger vortex shedding.

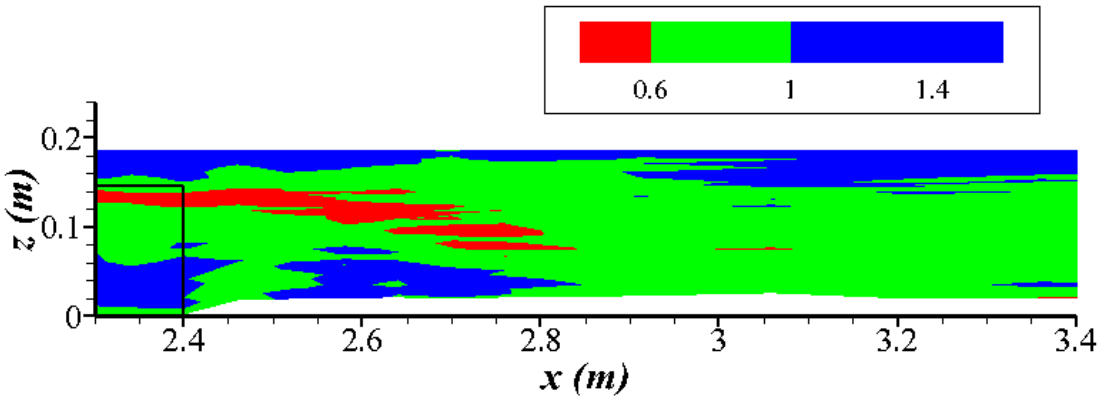

(a) Case 1 in Table 6.1

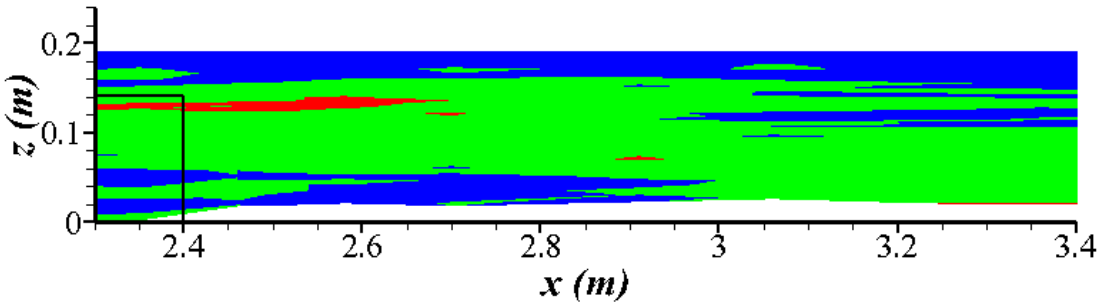

(b) Case 2 in Table 6.1

Figure 6.21. Contour maps of the ratio of time contribution from Q_2 and Q_4 (RS_2/RS_4) within the wake region

6.3. Numerical simulations

6.3.1 Simulation setup

The 3D RANS model described in Chapter 3 was used to replicate the flume experiments. Case 1 and Case 2 in Table 6.1 were chosen to test the applicability of the Spalart-Allmaras (S-A) model to reproduce the velocity and turbulence variations along the finite VP. The primary parameters for these two cases are shown in Table 6.1. Figure 6.22 illustrates the computational domain of the numerical simulations. The computational domain is carefully chosen for proper setting up of the inflow and outflow boundaries. The length of the computational domain is equal to the length of the VP (L_v = 2.4 m) and the width is equal to the width of flume (W = 0.31 m). The computational domain, therefore, covers the adjustment region and full-developed region (see Figure 6.1). Uniform grids were used in the present simulations. A grid independence study was firstly conducted to determine the appropriate number of grid points to be used by varying the total number of grid points. The final grid chosen has 97, 21 and 41 points in the streamwise, spanwise and vertical directions, respectively. A finer mesh used did not show any appreciable difference in the results. The time step is 0.002 s which is small enough to obtain grid convergent results. At the inflow boundary, a measured upstream velocity profile (as shown in Figure 6.23) was specified and the gradient of the water surface elevation is assumed to be zero. At the outflow boundary, the water surface elevation is specified and the velocity gradients are assumed to be zero. The zero gradient boundary condition was applied to the bottom and the side walls.

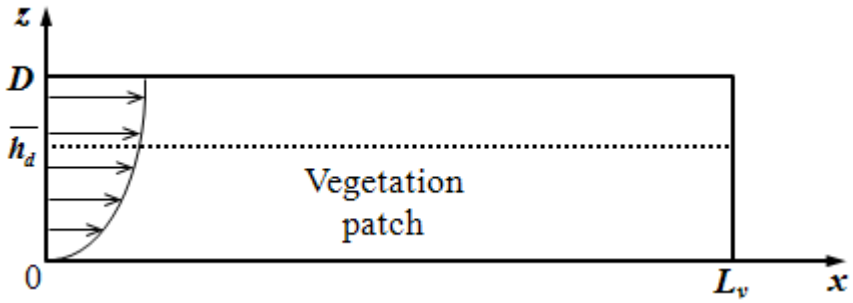

Figure 6.22. Computational domain (not to scale)

(The dot line denotes the time-averaged deflected height)

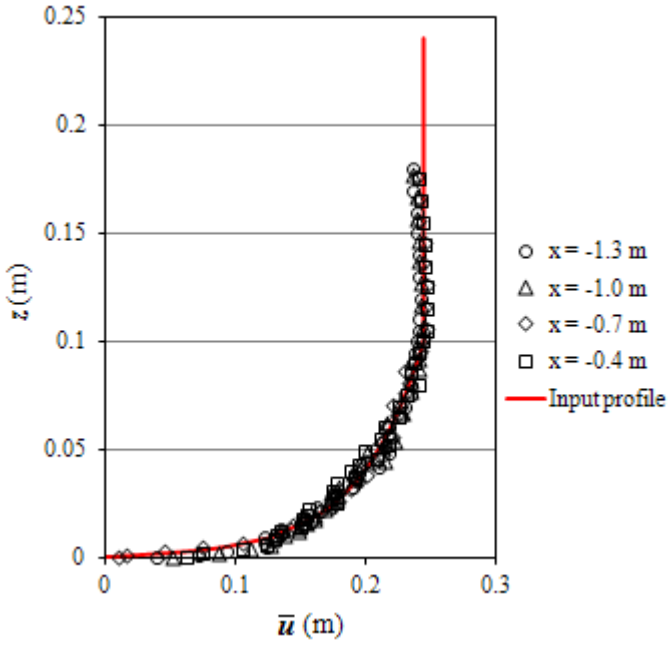

Figure 6.23. Input velocity profile at the inflow boundary

In order to simulate the drag force of VP, a drag coefficient C_d = 1.22 was used for these two cases. The value is slightly greater than the reported value (C_d = 1.13) for the circular cylinder rods but is lower than the reported value (C_d ~ 2.0) for a rectangular plate. According to Nepf *et al.* (2007a), parameter $C_d\alpha\overline{h_d}$ indicates whether the vegetation canopy is dense ($C_d\alpha\overline{h_d}$ > 0.1) or sparse ($C_d\alpha\overline{h_d}$ < 0.1). Hence, Case 1 ($C_d\alpha\overline{h_d} = 0.98$) and Case 2 ($C_d\alpha\overline{h_d} = 0.48$) are all belong to the first category.

6.3.2 Results

6.3.2.1. Results of water surface elevation

Figure 6.24 shows the comparisons between the computed and measured water surface profiles. It is seen that the agreement is acceptable and the simulations faithfully reproduces the water-surface variation from the leading edge to the trailing edge of VP.

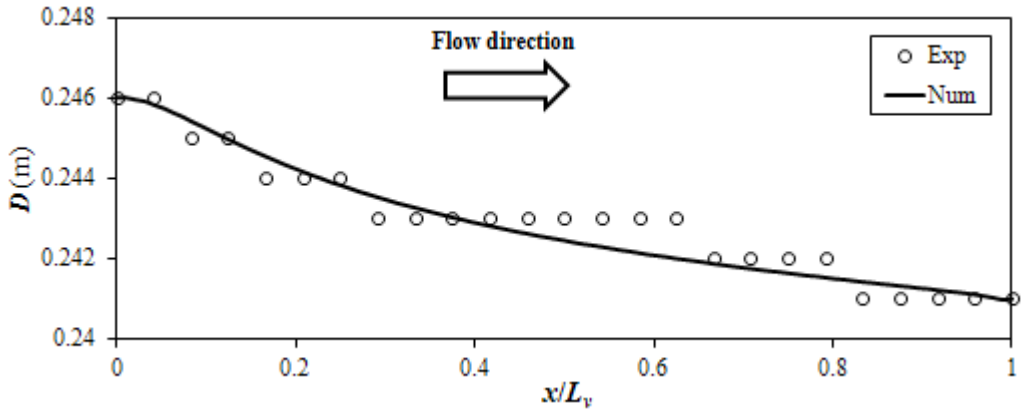

(a) Case 1 in Table 6.1

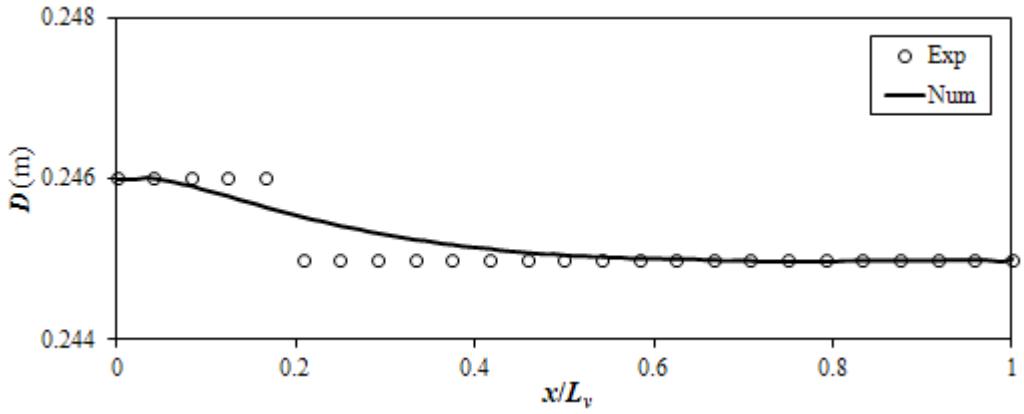

(b) Case 2 in Table 6.1

Figure 6.24. Comparison of water surface profiles along the flow direction

(Solid line – computed, circle - measured)

6.3.2.2. Results of streamwise velocity profiles

Figure 6.25 shows the computed vertical profile of streamwise velocity along the flow direction, together with those from the flume measurements. The dot line denotes the time-averaged deflected height $\overline{h_d}$. It can be seen that the RANS model successfully reproduces most of the flow characteristics of the flow evolution within the VP. A clear inflection point occurred at the deflected height in each computed profiles at different sections along the patch. The computed profiles are in good agreement with the experimental data within the fully-developed region for Case 1 ($x/L_v \geq 0.688$) and Case 2 ($x/L_v \geq 0.829$). Within the adjustment region, slightly lower velocity is computed within the canopy layer comparing to the flume measurements. The reason for the discrepancy is twofold. First, the stem wakes make a major contribution to the TKE and result in the suppression on the drag coefficient C_d within the adjustment region (Nepf 1999). As the wake turbulence cannot be modelled by the RANS model and the drag force method (DFM), the sheltering effect cannot be included in the present simulations. Second, the measurements in the present laboratory experiments were not spatially-averaged, while the velocities are locally varying around the plastic strips with low values behind the strips and high values in the free passage regions (point A as shown in Figure 6.4). The spatial difference is greater within the adjustment region. Since the sampling points were all located in the free passage regions, the values of the mean velocity are expected to be larger than the spatially-averaged values within the adjustment region.

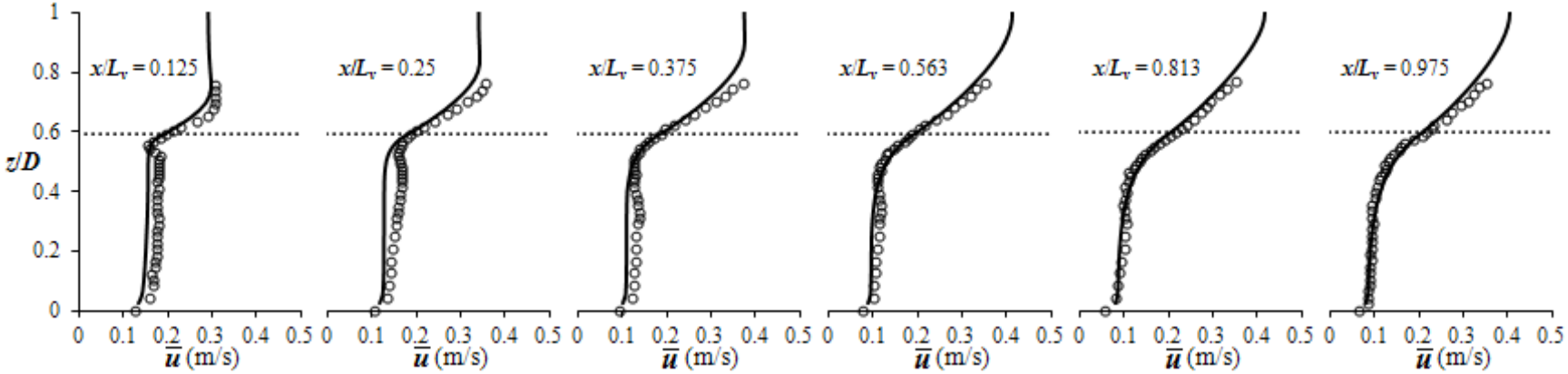

(a) Case 1 in Table 6.1

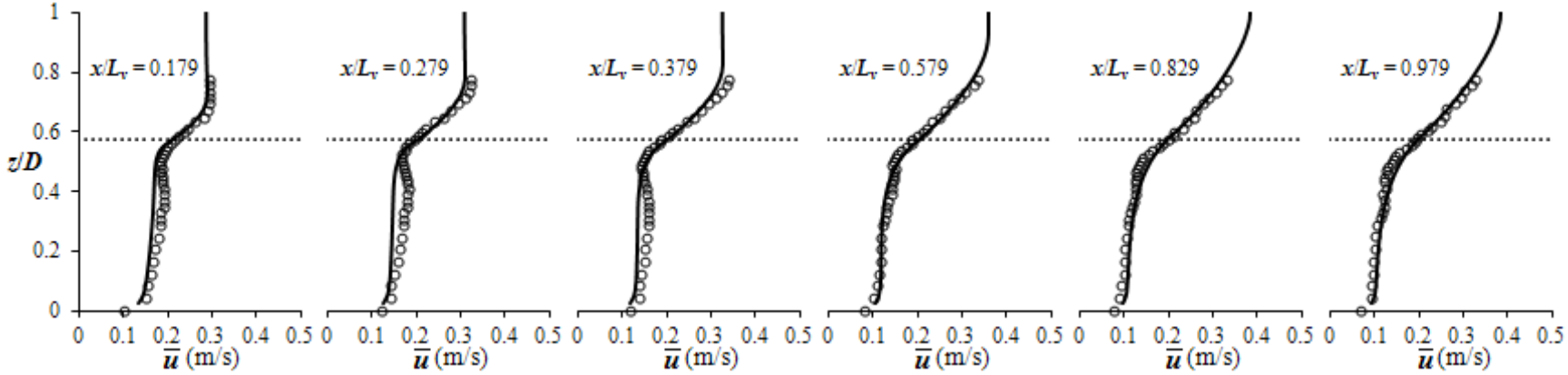

(b) Case 2 in Table 6.1

Figure 6.25. Vertical distributions of streamwise velocity $\bar{u}$ at various locations

6.3.2.3. Results of Reynolds stress profile

Figure 6.26 shows the computed vertical profiles of $-\overline{u'w'}$ along the flow direction, together with those from the flume measurements. The computed profiles show that the peak value occurs at the time-averaged deflected height (denoted by the dot line in Figure 6.26). The computed profiles are also in good agreement with the experimental data within the fully-developed region for Case 1 ($x/L_v \geq 0.688$) and Case 2 ($x/L_v \geq 0.829$). The major differences are found in the vegetation layer within the adjustment region where the wake turbulence takes place. In this region, the measured Reynolds stress is mostly induced by the stem-wake turbulence. Since the wake turbulence cannot be simulated by the RANS model and the DFM, the predicted values are nearly zero within the adjustment region.

Figure 6.27 gives the comparison of the computed and measured Reynolds stress maxima. The agreement is fairly good within the fully-developed region. The numerical model slightly overpredicted the peak values at the time-averaged deflected height within the adjustment region. This can also be attributed to the two reasons mentioned in the previous section.

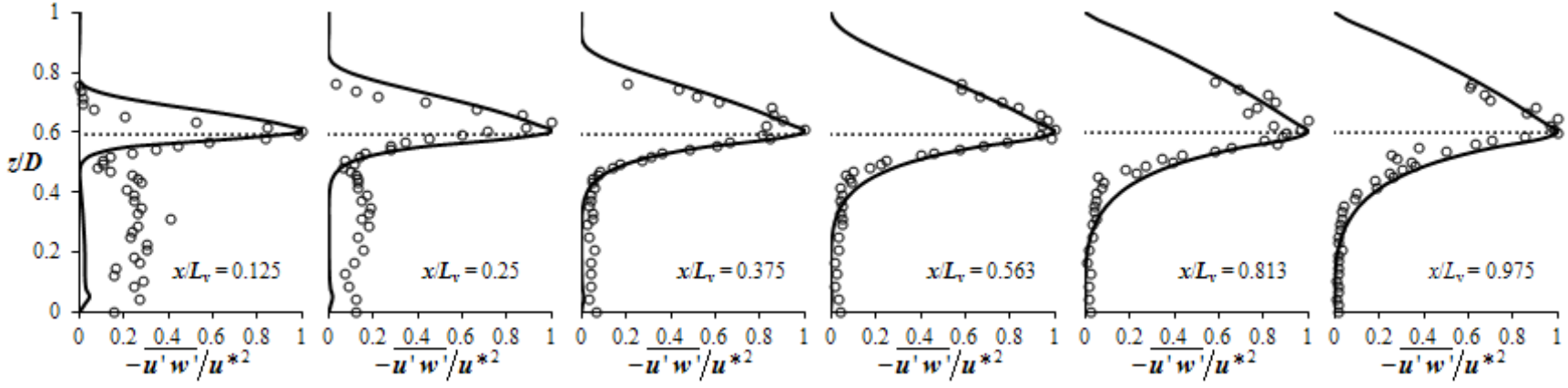

(a) Case 1 in Table 6.1

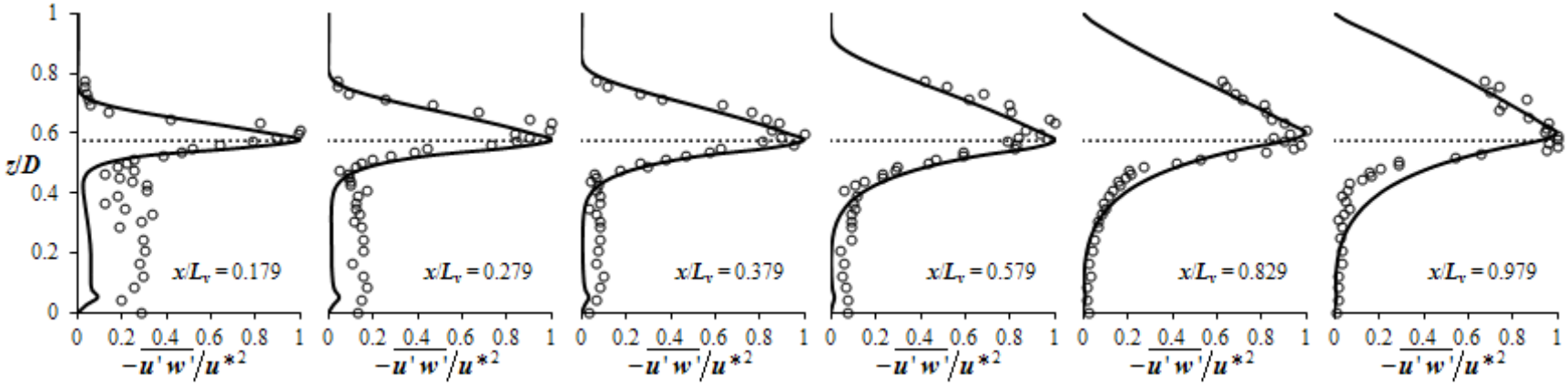

(b) Case 2 in Table 6.1

Figure 6.26. Vertical distribution of Reynolds stress (per unit mass) $-\overline{u'w'}$ at various locations

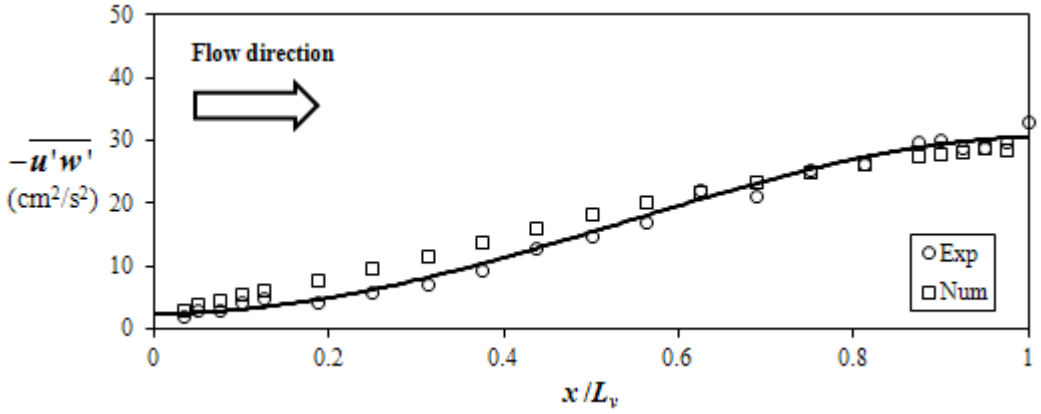

(a) Case 1 in Table 6.1

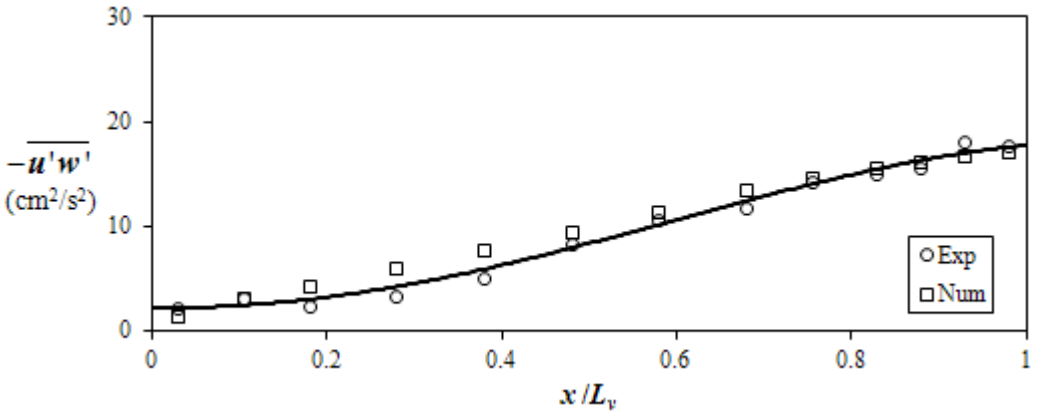

(b) Case 2 in Table 6.1

Figure 6.27. Comparison of the Reynolds stress maxima along the flow direction

6.4. Conclusions

In this chapter, the open-channel flows with finite flexible vegetation patch have been studied experimentally and numerically. The flume measurements complement previous laboratory and field studies by revealing the flow structure, turbulence distribution and the evolution across the leading edge as well as the trailing edge of vegetation canopy. Comparing to the reported cases with rigid VP, the high-level turbulence region is found at a farther downstream distance beyond the leading edge for the case with flexible VP because high frequency vibration of the strips dissipate

part of the TKE. The length of the adjustment region and the turbulence level are dependent on the vegetation density and the upstream Reynolds number. Throughout the flow filed, the minimum and maximum values of the Reynolds stress occur at the top of the leading edge and the trailing edge, respectively.

For the first time, the coherent flow structures were identified using quadrant analysis in canopy flows with finite patch. It was found that the Q_2 events (ejections) and the Q_4 events (sweeps) are dominant in the adjustment region and the wake region, respectively. Within the fully-developed region, the Q_2 events (ejections) and the Q_4 events (sweeps) are dominant in the upper shear layer and the exchange zone, respectively. The existence of the K-H vortices within the shear layer is confirmed by both the flow visualization and the quadrant analysis. Stronger swaying was observed within flows with HD patch.

The 3D RANS model incorporating the drag force method (DFM) and the S-A turbulence closure were used to replicate the flow evolution within the VP. The model faithfully reproduced most of the flow characteristics and reached a good agreement with the experimental data within fully-developed region. Further refinement of the numerical model is needed for more accurate prediction in the adjustment region.

Chapter 7.

Summary, Conclusions and Future Works

7.1. Conclusions

The flow behaviour in association with bed roughness has been a fundamental issue of river hydraulics and fluvial morphodynamics and received considerable attention for decades. The present research deepens the understanding of this issue through detailed flume measurements and numerical modelling of open-channel flow with gravel and vegetation roughnesses. Consistent results were obtained from both laboratory observations and numerical simulations.

7.7.1 Numerical study

The whole numerical study is separated into two parts. A 3D RANS model was refined to model open-channel flows with smooth bed, submerged vegetation canopy as well as the flow evolution within a finite VP. Next a DANS model was developed for depth-limited open-channel flows over gravel bed. The main findings from these two parts are as follows.

1. The 3D RANS model was firstly validated against two well-documented laboratory experiments: open-channel flow with smooth bed

(Nezu and Rodi 1986), and open-channel flow with submerged vegetation canopy (Dunn *et al.* 1996). For the former case, the numerical model successfully replicated the flow conditions with different Reynolds numbers (Re_τ = 439 and 2143). With the development of an appropriate empirical equation, the S-A model accurately reproduced the distribution of the TKE. In the latter case, the DFM is employed to simulate the vegetative resistance. By taking a constant value for drag coefficient (C_d = 1.13), suggested by Dunn *et al*. (1996), the numerical model yielded accurate profiles for open-channel flow with rigid or flexible vegetation canopy. This model was subsequently used to replicate the flow evolution within a finite VP. By comparing to the detailed flume measurements, the numerical model was found to be able to accurately reproduce most of the flow characteristics.

2. A DANS model incorporating the DFM and a modified S-A turbulence closure has been developed for the modelling of depth-limited open-channel flow over gravel-bed. Extensive tests indicate that the numerical model can simulate accurately the velocity profiles in the interfacial sublayer, form-induced sublayer and logarithmic layer. Particularly, the S-shaped velocity profile for sparely distributed large size roughness elements can be reproduced. The modification of the turbulence length scale within the interfacial sublayer increases the viscous force and reduces the drag force in balancing the gravitational force component. The parameter for the turbulence length scale (c_r) was found to be able to control the magnitude of the Reynolds stress within the interfacial sublayer and the value of 0.3 is recommended from the case studies. The modified S-A model is able to generate a quasi-linear

velocity distribution within the interfacial sublayer and also leads to a more consistent parameterization of the bulk drag coefficient (C_dC_s). The DFM is found to be robust and can be easily integrated into the existing numerical models.

7.7.2 Experimental study

For the experimental study, two laboratory experiments were performed for open-channel flows with gravel patch (GP) and VP, respectively.

1. Laboratory experiments were performed to investigate the vertical distribution of the streamwise velocity and turbulence intensity, as well as the friction factor in depth-limited open-channel flow over gravel patch. Two gravel patches were examined: a short patch (SP) with length equal to 3.81 m, and a long patch (LP) with length equal to 7.5 m. A total of 33 experiments were performed with the relative submergence range from 2.68 to 5.94. The measured profiles, which have been double averaged (spatially and temporally), were found to fit well with the log law and defect law with a non-universal Karman constant κ. For LP cases, the values of κ are nearly constant and in the range from 0.2 to 0.3. For SP cases, the κ-values are scattered within a wider range from 0.3 to 0.5. Furthermore, while the *Br*-value remains constant and equals to 8.5 for LP cases, the *Br*-value was found to decrease with the increase of the dimensionless roughness height k_s^+ for SP cases. The streamwise turbulence intensity distributions were found to agree well with the available experimental data in the intermediate region and wall region. Under the relatively small submergence, the measured value of resistance factor c_n (=

$n_b/k_s^{1/6}$) was found to be around 0.04, supporting the results of Sturm (2010) and Henderson (1966). The κ-value decrease to 0.22 for the semilogarithmic flow resistance law (Equation 5-13). The experimental data follow the linear relationship and generally fall within the threshold $\overline{Br}$-values of 3.25 and 6.25.

2. Laboratory experiments were performed to investigate the flow structure, turbulence distribution and the evolution processes within and beyond the VP. Two VPs with different density were examined: a high density (HD) patch with α = 5.56 m^{-1}, and a low density (LD) patch with α = 2.28 m^{-1}. The VP, which decelerated the flow within the canopy and accelerated the overlying flow, appeared to be swaying under different flow rates. Stronger swaying was observed within flows with the HD patch. Comparing to the laboratory observations with rigid VP, the high-level turbulence region within the adjustment region located at a farther downstream distance from the leading edge for the case with flexible VP, as the high frequency vibration of the strips dissipate part of the TKE. The length of the adjustment region and the turbulence level increase with the increase of the vegetation density and the upstream Reynolds number. In the fully-developed region the increasing vegetation density leads to the increasing in the degree of inflection in the mean velocity profile. A quadrant analysis was also carried out, which revealed that the Q_2 events (ejections) and the Q_4 events (sweeps) are dominant in the adjustment region and the wake region, respectively. Within the fully-developed region, the Q_2 events (ejections) and the Q_4 events (sweeps) are dominant in the upper shear layer and the exchange zone, respectively.

7.2. Future work

In this study both the experimental and numerical approaches were employed to investigate the open-channel flows with gravel and vegetation roughnesses. Although some promising results are obtained, there are still rooms for improvement. Future work to be done may focus on the following aspects:

1. The DANS equations have been recognized to have a better basis for hydrodynamic modelling of rough-bed flows comparing to the conventional RANS. However, to the author's knowledge, model equations have not yet been developed to parameterize the form-induced stress terms arising from the DA procedure. In order to parameterize and present these terms in the models, an improved understanding of these stresses is needed, which requires specially designed laboratory or field measurements in the further studies.

2. ADV and UVP were employed in the laboratory experiments. The operations with these two instruments have confirmed that they are accurate and reliable for velocity and turbulence measurements in open-channel flows. The main shortcoming of these two instruments is that their sampling volume is still not small enough for the measurements in the very near-wall region. Furthermore, it was not possible to measure the uppermost 5 cm layer of the water column by using ADV, and the possible faster velocities near the water surface cannot be recorded. Therefore, in the further experimental studies, some advanced measuring instruments, such as LDA, PIV or PTV, should preferably be adopted.

3. For the open-channel flow with finite VP, DA measurements should

be performed within the adjustment region, especially near the leading edge. By comparing to these DA measurements, the numerical simulation can be improved accordingly. Generally speaking, there are two possible methods for the model improvement. First, if a RANS model is still used, a sheltering coefficient can be introduced into the drag force term in the momentum equation within the adjustment region. Second, the large eddy simulation (LES), in which turbulence can be partly resolved, might be able to simulate the wake turbulence occurred in the leading edge region.

References

Aberle, J., Koll, K., and Dittrich, A. (2008). "Form induced stresses over rough gravel-beds." *Acta Geophysica*, 56(3), 584-600.

Aupoix, B., and Spalart, P. R. (2003). "Extensions of the Spalart-Allmaras turbulence model to account for wall roughness." *International Journal of Heat and Fluid Flow*, 24(4), 454-462.

Bathurst, J. C. (1988). "Velocity profile in high-gradient, boulder-bed channels." *Proc., Int. Conf. on Fluvial Hydraulics*, Budapest, Hungary.

Bayazit, M. (1976). "Free surface flow in a channel of large relative roughness." *Journal of Hydraulic Research*, 14(2), 115-126.

Bayazit, M. (1983). "Flow structure and sediment transport mechanics in steep channels." In: *Mechanics of sediment transport - Proceedings of Euromech 156: Mechanics of sediment transport, Istanbul*, B. M. Sumer and A. Müller (eds.), Balkema, Rotterdam, 197-206.

Belcher, S. E., Jerram, N., and Hunt, J. C. R. (2003). "Adjustment of a turbulent boundary layer to a canopy of roughness elements." *Journal of Fluid Mechanics*, 488, 369-398.

Bennett, S. J., and Best, J. L. (1995). "Mean flow and turbulence structure over fixed, two-dimensional dunes: implications for sediment transport and bedform stability." *Sedimentology*, 42(3), 491-513.

Blinco, P. H., and E. Partheniades. (1971). "Turbulence characteristics in free surface flows over smooth and rough boundaries." *Journal of Hydraulic Research*, 9(1), 43-71.

Bouma, T. J., van Duren, L. A., Temmerman, S., Claverie, T., Blanco-Garcia, A., Ysebaert, T., and Herman, P. M. J. (2007). "Spatial flow and sedimentation

patterns within patches of epibenthic structures: Combining field, flume and modelling experiments." *Continental Shelf Research*, 27(8), 1020-1045.

Bray, D. I. (1980). "Evaluation of effective boundary roughness for gravel-bed rivers." *Canadian Journal of Civil Engineering*, 7(2), 392-397.

Bray, D. I. (1982). "Flow resistance in gravel-bed rivers." In: *Gravel-bed rivers*, R. D. Hey (eds.), John Wiley and Sons, Chichester, England, 109-133.

Breuer, M., Jovicic, N., and Mazaev, K. (2003). "Comparison of DES, RANS and LES for the separated flow around a flat plate at high incidence." *International Journal for Numerical Methods in Fluids*, 41(4), 357-388.

Buffin-Belanger, T., Rice, S., Reid, I., and Lancaster, J. (2006). "Spatial heterogeneity of near-bed hydraulics above a patch of river gravel." *Water Resources Research*, 42(4).

Buffin-Belanger, T., and Roy, A. G. (1998). "Effects of a pebble cluster on the turbulent structure of a depth-limited flow in a gravel-bed river." *Geomorphology*, 25(3-4), 249-267.

Cardoso, A. H., Graf, W. H., and Gust, G. (1989). "Uniform flow in a smooth open channel." *Journal of Hydraulic Research*, 27(5), 603-616.

Carling, P. A., Kelsey, A., and Glaister, M. S. (1992). "Effect of bed roughness, particle shape and orientation on initial motion criteria." In: *Dynamics of Gravel-Bed Rivers*, P. Billi, R. D. Hey, C. R. Thorne, and P. Tacconi (eds.), John Wiley and Sons, New York, 23-38.

Carney, S. K., Bledsoe, B. P., and Gessler, D. (2006). "Representing the bed roughness of coarse-grained streams in computational fluid dynamics." *Earth Surface Processes and Landforms*, 31(6), 736-749.

Carollo, F. G., Ferro, V., and Termini, D. (2002). "Flow velocity measurements in vegetated channels." *Journal of Hydraulic Engineering-Asce*, 128(7), 664-673.

Chanson, H., Trevethan, M., and Koch, C. (2007). "Discussion of "Turbulence

measurements with acoustic Doppler velocimeters" by Carlos M. Garcia, Mariano I. Cantero, Yarko Nino, and Marcelo H. Garcia." *Journal of Hydraulic Engineering-Asce*, 133(11), 1283-1286.

Choi, S. U., and Kang, H. (2006). "Numerical investigations of mean flow and turbulence structures of partly-vegetated open-channel flows using the Reynolds stress model." *Journal of Hydraulic Research*, 44(2), 203-217.

Choi, S. U., and Kang, H. S. (2004). "Reynolds stress modeling of vegetated open-channel flows." *Journal of Hydraulic Research*, 42(1), 3-11.

Chow, V. T. (1959). *Open-channel hydraulics*, McGraw-Hill, New York.

Clark, J. A. (1968). "A study of incompressible turbulent boundary layers in channel flow." *Journal of Basic Engineering, ASCE*, 90, 455-468.

Coleman, N. L. (1967). "A theoretical and experimental study of drag and lift forces acting on a sphere resting on a hypothetical streambed." *Proceedings of the 12th Congress, Vol. 3*, Colorado State University, Colo., 185-192.

Cui, J., Patel, V. C., and Lin, C. L. (2003a). "Large-eddy simulation of turbulent flow in a channel with rib roughness." *International Journal of Heat and Fluid Flow*, 24(3), 372-388.

Cui, J., Patel, V. C., and Lin, C. L. (2003b). "Prediction of turbulent flow over rough surfaces using a force field in large eddy simulation." *Journal of Fluids Engineering-Transactions of the Asme*, 125(1), 2-9.

del Alamo, J. C., and Jimenez, J. (2003). "Spectra of the very large anisotropic scales in turbulent channels." *Physics of Fluids*, 15(6), L41-L44.

Dimas, A. A., Fourniotis, N. T., Vouros, A. P., and Demetracopoulos, A. C. (2008). "Effect of bed dunes on spatial development of open-channel flow." *Journal of Hydraulic Research*, 46(6), 802-813.

Dimitris, S., and Panayotis, P. (2011). "Macroscopic Turbulence Models and Their Application in Turbulent Vegetated Flows." *Journal of Hydraulic Engineering*,

137(3), 315-332.

Dittrich, A., and Koll, K. (1997). "Velocity field and resistance of flow over rough surfaces with large and small relative submergence." *International Journal of Sediment Research*, 12(3), 21-33.

Dunn, C., Lopez, F., and Garcia, M. (1996). "*Mean flow and turbulence structure induced by vegetation: Experiments*." Hydraulic Engineering Series No. 51, UILU-ENG 96-2009.

Dupont, S., and Brunet, Y. (2008). "Edge Flow and Canopy Structure: A Large-Eddy Simulation Study." *Boundary-Layer Meteorology*, 126(1), 51-71.

Dupont, S., and Brunet, Y. (2009). "Coherent structures in canopy edge flow: a large-eddy simulation study." *Journal of Fluid Mechanics*, 630, 93-128.

Ferro, V. (1999). "Friction factor for gravel-bed channel with high boulder concentration." *Journal of Hydraulic Engineering-Asce*, 125(7), 771-778.

Ferro, V. (2003). "ADV measurements of velocity distributions in a gravel-bed flume." *Earth Surface Processes and Landforms*, 28(7), 707-722.

Ferro, V., and Baiamonte, G. (1994). "Flow velocity profiles in gravel-bed rivers." *Journal of Hydraulic Engineering-Asce*, 120(1), 60-80.

Ferro, V., and Giordano, G. (1991). "Experimental-study of flow resistance in gravel-bed rivers." *Journal of Hydraulic Engineering-Asce*, 117(10), 1239-1246.

Finnigan, J. (2000). "Turbulence in plant canopies." *Annual Review of Fluid Mechanics*, 32, 519-571.

Finnigan, J. J., Shaw, R. H., and Patton, E. G. (2009). "Turbulence structure above a vegetation canopy." *Journal of Fluid Mechanics*, 637, 387-424.

Fischer-Antze, T., Stoesser, T., Bates, P., and Olsen, N. R. B. (2001). "3D numerical modelling of open-channel flow with submerged vegetation." *Journal of*

Hydraulic Research, 39(3), 303-310.

FLUENT. (2005). *Fluent 6.2 User Guide*, Fluent Inc., Lebanon, NH.

Folkard, A. (2011). "Flow regimes in gaps within stands of flexible vegetation: laboratory flume simulations." *Environmental Fluid Mechanics*, 11(3), 289-306.

Folkard, A. M. (2005). "Hydrodynamics of model Posidonia oceanica patches in shallow water." *Limnology and Oceanography*, 50(5), 1592-1600.

Franca, M. J., and Lemmin, U. (2009). "The simultaneous occurence of logarithmic and S-shaped velocity profiles in gravel-bed river flows." *Archives of Hydro-Engineering and Environmental Mechanics*, 56(1-2), 29-41.

Gaudio, R., Miglio, A., and Dey, S. (2010). "Non-universality of von Karman's kappa in fluvial streams." *Journal of Hydraulic Research*, 48(5), 658-663.

Gessler, J. (1990). "Friction factor of armored river beds." *Journal of Hydraulic Engineering-Asce*, 116(4), 531-543.

Ghisalberti, M., and Nepf, H. (2005). "Mass Transport in Vegetated Shear Flows." *Environmental Fluid Mechanics*, 5(6), 527-551.

Ghisalberti, M., and Nepf, H. (2006). "The structure of the shear layer in flows over rigid and flexible canopies." *Environmental Fluid Mechanics*, 6(3), 277-301.

Ghisalberti, M., and Nepf, H. (2009). "Shallow Flows Over a Permeable Medium: The Hydrodynamics of Submerged Aquatic Canopies." *Transport in Porous Media*, 78(3), 385-402.

Ghisalberti, M., and Nepf, H. M. (2002). "Mixing layers and coherent structures in vegetated aquatic flows." *Journal of Geophysical Research-Oceans*, 107(C2).

Goring, D. G., and Nikora, V. I. (2002). "Despiking acoustic Doppler velocimeter data." *Journal of Hydraulic Engineering-Asce*, 128(1), 117-126.

Graf, W., Armanini, A., and Di Silvio, G. (1991). "Flow resistance over a gravel bed:

Its consequence on initial sediment movement." In: *Fluvial Hydraulics of Mountain Regions*, Springer Berlin / Heidelberg, 15-32.

Graf, W. H. (1984). "Flow resistance for steep, mobile channels." *Proceedings of Workshop 'Idraulica del territorio montano'*, Bressanone, 341-352.

Hager, W. H. (1999). *Wastewater Hydraulics*, Springer-Verlag, Berlin.

Hardy, R. J., Best, J. L., Lane, S. N., and Carbonneau, P. E. (2009). "Coherent flow structures in a depth-limited flow over a gravel surface: The role of near-bed turbulence and influence of Reynolds number." *Journal of Geophysical Research-Earth Surface*, 114.

Hardy, R. J., Best, J. L., Lane, S. N., and Carbonneau, P. E. (2010). "Coherent flow structures in a depth-limited flow over a gravel surface: The influence of surface roughness." *Journal of Geophysical Research-Earth Surface*, 115.

Henderson, F. M. (1966). *Open channel flow*, Macmillan Co., New York.

Hey, R. D. (1979). "Flow resistance in gravel-bed rivers." *Journal of the Hydraulics Division-Asce*, 105(4), 365-379.

Hey, R. D., and Thorne, C. R. (1986). "Stable channels with mobile gravel beds." *Journal of Hydraulic Engineering-Asce*, 112(8), 671-689.

Hoyas, S., and Jimenez, J. (2006). "Scaling of the velocity fluctuations in turbulent channels up to Re-tau=2003." *Physics of Fluids*, 18(1).

Ikeda, S., and Kanazawa, M. (1996). "Three-dimensional organized vortices above flexible water plants." *Journal of Hydraulic Engineering-Asce*, 122(11), 634-640.

Irvine, M. R., Gardiner, B. A., and Hill, M. K. (1997). "The evolution of turbulence across a forest edge." *Boundary-Layer Meteorology*, 84(3), 467-496.

Jackson, P. S. (1981). "On the displacement height in the logarithmic velocity profile." *Journal of Fluid Mechanics*, 111, 15-25.

Jarvela, J. (2002). "Flow resistance of flexible and stiff vegetation: a flume study with natural plants." *Journal of Hydrology*, 269(1-2), 44-54.

Kamphuis, J. W. (1974). "Determination of sand roughness for fixed beds." *Journal of Hydraulic Research*, 12(2), 193-203.

Katul, G., Wiberg, P., Albertson, J., and Hornberger, G. (2002). "A mixing layer theory for flow resistance in shallow streams." *Water Resources Research*, 38(11).

Kemp, J. L., Harper, D. M., and Crosa, G. A. (2000). "The habitat-scale ecohydraulics of rivers." *Ecological Engineering*, 16(1), 17-29.

Keskinkan, O., Goksu, M. Z. L., Basibuyuk, M., and Forster, C. F. (2004). "Heavy metal adsorption properties of a submerged aquatic plant (Ceratophyllum demersum)." *Bioresource Technology*, 92(2), 197-200.

Kirchner, J. W., Dietrich, W. E., Iseya, F., and Ikeda, H. (1990). "The variability of critical shear stress, friction angle, and grain protrusion in water-worked sediments." *Sedimentology*, 37(4), 647-672.

Kirkgoz, M. S. (1989). "Turbulent Velocity Profiles for Smooth and Rough Open Channel Flow." *Journal of Hydraulic Engineering-Asce*, 115(11), 1543-1561.

Kirkgoz, M. S., and Ardiclioglu, M. (1997). "Velocity profiles of developing and developed open channel flow." *Journal of Hydraulic Engineering-Asce*, 123(12), 1099-1105.

Kironoto, B. A., and Graf, W. H. (1994). "Turbulence characteristics in rough uniform open-channel flow." *Proceedings of the Institution of Civil Engineers-Water Maritime and Energy*, 106(4), 333-344.

Kironoto, B. A., and Graf, W. H. (1995). "Turbulence characteristics in rough non-uniform open-channel flow." *Proceedings of the Institution of Civil Engineers-Water Maritime and Energy*, 112(4), 336-348.

Koll, K. (2006). "Parameterisation of the vertical velocity profile in the wall region over rough surfaces." In: *River Flow 2006*, Taylor & Francis.

Kothyari, U. C., Hashimoto, H., and Hayashi, K. (2009). "Effect of tall vegetation on sediment transport by channel flows." *Journal of Hydraulic Research*, 47(6), 700 - 710.

Kouwen, N., and Unny, T. E. (1973). "Flexible roughness in open channels." *Journal of the Hydraulics Division-Asce*, 99(HY5), 713-728.

Lane, S. N., Hardy, R. J., Elliott, L., and Ingham, D. B. (2004). "Numerical modeling of flow processes over gravelly surfaces using structured grids and a numerical porosity treatment." *Water Resour. Res.*, 40(1), W01302.

Lawless, M., and Robert, A. (2001a). "Scales of boundary resistance in coarse-grained channels: turbulent velocity profiles and implications." *Geomorphology*, 39(3-4), 221-238.

Lawless, M., and Robert, A. (2001b). "Three-dimensional flow structure around small-scale bedforms in a simulated gravel-bed environment." *Earth Surface Processes and Landforms*, 26(5), 507-522.

Lee, J., and Paynter, G. C. (1996). "Modified Spalart-Allmaras one-equation turbulence model for rough wall boundary layers." *Journal of Propulsion and Power*, 12(4), 809-812.

Leonard, B. P. (1979). "A stable and accurate convective modelling procedure based on quadratic upstream interpolation." *Computer Methods in Applied Mechanics and Engineering*, 19(1), 59-98.

Li, C. W. (1990). "Advection simulation by mlnimax-characteristics method." *Journal of Hydraulic Engineering-Asce*, 116(9), 1138-1144.

Li, C. W., and Yan, K. (2007). "Numerical investigation of wave-current-vegetation interaction." *Journal of Hydraulic Engineering-Asce*, 133(7), 794-803.

Li, C. W., and Yu, L. H. (2010). "Hybrid LES/RANS modelling of free surface flow through vegetation." *Computers & Fluids*, 39(9), 1722-1732.

Li, C. W., and Zeng, C. (2009). "3D Numerical modelling of flow divisions at open

channel junctions with or without vegetation." *Advances in Water Resources*, 32(1), 49-60.

Lin, P., and Li, C. W. (2002). "A σ-coordinate three-dimensional numerical model for surface wave propagation." *International Journal for Numerical Methods in Fluids*, 38(11), 1045-1068.

Lohrmann, A., Cabrera, R., and Kraus, N. C. (1994). "Acoustic-Doppler velocimeter (ADV) for laboratory use." In: *Fundamentals and Advancements in Hydraulic Measurements and Experimentation*, C. A. Pugh (eds.), 351-365.

Lopez, F., and Garcia, M. (1997). "*Open channel flow through simulated vegetation: Turbulence modelling and sediment transport*."

Lopez, F., and Garcia, M. H. (2001). "Mean flow and turbulence structure of open-channel flow through non-emergent vegetation." *Journal of Hydraulic Engineering-Asce*, 127(5), 392-402.

Lu, S. S., and Willmarth, W. W. (1973). "Measurements of the structure of the Reynolds stress in a turbulent boundary layer." *Journal of Fluid Mechanics*, 60(03), 481-511.

Luchik, T. S., and Tiederman, W. G. (1987). "Timescale and structure of ejections and bursts in turbulent channel flows." *Journal of Fluid Mechanics*, 174, 529-552.

Maltese, A., Cox, E., Folkard, A. M., Ciraolo, G., La Loggia, G., and Lombardo, G. (2007). "Laboratory measurements of flow and turbulence in discontinuous distributions of ligulate seagrass." *Journal of Hydraulic Engineering-Asce*, 133(7), 750-760.

Manes, C., Pokrajac, D., Coceal, O., and McEwan, I. (2008). "On the significance of form-induced stress in rough wall turbulent boundary layers." *Acta Geophysica*, 56(3), 845-861.

Manes, C., Pokrajac, D., and McEwan, I. (2007). "Double-averaged open-channel flows with small relative submergence." *Journal of Hydraulic*

Engineering-Asce, 133(8), 896-904.

Manes, C., Pokrajac, D., McEwan, I., and Nikora, V. (2009). "Turbulence structure of open channel flows over permeable and impermeable beds: A comparative study." *Physics of Fluids*, 21(12).

Marchand, J. P., Jarrett, R. D., and Jones, L. L. (1984). "*Velocity profile, water-surface slope, and bed-material size for selected streams in Colorado*." U.S. Geological Survey Open File Report, 84-733.

Martine, V. (2003). "Hydraulic roughness of armoured gravel beds: the role of grain protrusion," Ph.D. Thesis, University of British Columbia, Kelowna, British Columbia, Canada.

Martino, R., Paterson, A., and Piva, M. (2011). "Double-average mean flow and local turbulence intensity profiles from PIV measurements for an open channel flow with rigid vegetation." *Environmental Fluid Mechanics*, 1-18.

Mignot, E., Barthelemy, E., and Hurther, D. (2008). "Turbulent kinetic energy budget in a gravel-bed channel flow." *Acta Geophysica*, 56(3), 601-613.

Monin, A. S., and Yaglom, A. M. (1971). *Statistical Fluid Mechanics, Volume I: Mechanics of Turbulence*, MIT Press, Boston.

Morris, H. M. (1955). "A new concept of flow in rough conduits." *Transactions of the American Society of Civil Engineers*, 120, 373-398.

Nakagawa, H., Nezu, I., and Ueda, H. (1975). "Turbulence of open channel flow over smooth and rough beds." *Proc. of Japan Soc. Civil Engrs*, 241, 155-168.

Naot, D., and Emrani, S. (1982). "Numerical simulation of the hydrodynamic behavior of fuel rod with longitudinal cooling fins." *Nuclear Engineering and Design*, 73(3), 319-329.

Naot, D., Nezu, I., and Nakagawa, H. (1996a). "Hydrodynamic behavior of partly vegetated open channels." *Journal of Hydraulic Engineering-Asce*, 122(11), 625-633.

Naot, D., Nezu, I., and Nakagawa, H. (1996b). "Unstable patterns in partly vegetated channels." *Journal of Hydraulic Engineering-Asce*, 122(11), 671-673.

Neary, V. S. (2003). "Numerical solution of fully developed flow with vegetative resistance." *Journal of Engineering Mechanics-Asce*, 129(5), 558-563.

Nepf, H., and Ghisalberti, M. (2008). "Flow and transport in channels with submerged vegetation." *Acta Geophysica*, 56(3), 753-777.

Nepf, H., Ghisalberti, M., White, B., and Murphy, E. (2007a). "Retention time and dispersion associated with submerged aquatic canopies." *Water Resources Research*, 43(4).

Nepf, H., White, B., Lightbody, A., and Ghisalberti, M. (2007b). "Transport in aquatic canopies." In: *Flow and Transport Processes with Complex Obstructions*, Springer Netherlands, 221-250.

Nepf, H. M. (1999). "Drag, turbulence, and diffusion in flow through emergent vegetation." *Water Resources Research*, 35(2), 479-489.

Nepf, H. M., and Vivoni, E. R. (2000). "Flow structure in depth-limited, vegetated flow." *Journal of Geophysical Research-Oceans*, 105(C12), 28547-28557.

Neumeier, U. (2007). "Velocity and turbulence variations at the edge of saltmarshes." *Continental Shelf Research*, 27(8), 1046-1059.

Nezu, I. (1977). "Turbulent structure in open channel flows," Ph.D. thesis, Kyoto University, Kyoto, Japan.

Nezu, I., and Nakagawa, H. (1993). *Turbulence in open channel flows, IAHR*, Balkema, Rotterdam, Netherlands.

Nezu, I., and Rodi, W. (1986). "Open-channel flow measurements with a laser Doppler anemometer." *Journal of Hydraulic Engineering-Asce*, 112(5), 335-355.

Nezu, I., and Sanjou, M. (2008). "Turburence structure and coherent motion in vegetated canopy open-channel flows." *Journal of Hydro-Environment*

Research, 2(2), 62-90.

Nicholas, A. P. (2001). "Computational fluid dynamics modelling of boundary roughness in gravel-bed rivers: An investigation of the effects of random variability in bed elevation." *Earth Surface Processes and Landforms*, 26(4), 345-362.

Nicholas, A. P. (2005). "Roughness parameterization in CFD modelling of gravel-bed rivers." In: *Computational Fluid Dynamics: Applications in Environmental Hydraulics*, P. D. Bates, S. Lane, N., and R. I. Ferguson (eds.), John Wiley and Sons, Chichester, England, 329-355.

Nicholas, A. P., and Smith, G. H. S. (1999). "Numerical simulation of three-dimensional flow hydraulics in a braided channel." *Hydrological Processes*, 13(6), 913-929.

Nikora, N., Koll, K., McLean, S., Dittrich, A., and Aberle, J. (2002). "Zero-plane displacement for rough-bed open-channel flows." *Proc., Int. Conf. on Fluvial Hydraulics "River Flow 2002"*, Louvainla-Neuve, Belgium, 83-92.

Nikora, V., Goring, D., McEwan, I., and Griffiths, G. (2001). "Spatially averaged open-channel flow over rough bed." *Journal of Hydraulic Engineering-Asce*, 127(2), 123-133.

Nikora, V., Koll, K., McEwan, I., McLean, S., and Dittrich, A. (2004). "Velocity distribution in the roughness layer of rough-bed flows." *Journal of Hydraulic Engineering-Asce*, 130(10), 1036-1042.

Nikora, V., Lamed, S., Nikora, N., Debnath, K., Cooper, G., and Reid, M. (2008). "Hydraulic resistance due to aquatic vegetation in small streams: Field study." *Journal of Hydraulic Engineering-Asce*, 134(9), 1326-1332.

Nikora, V., McEwan, I., McLean, S., Coleman, S., Pokrajac, D., and Walters, R. (2007a). "Double-averaging concept for rough-bed open-channel and overland flows: Theoretical background." *Journal of Hydraulic Engineering-Asce*, 133(8), 873-883.

Nikora, V., McLean, S., Coleman, S., Pokrajac, D., McEwan, I., Campbell, L., Aberle, J., Clunie, D., and Kol, K. (2007b). "Double-averaging concept for rough-bed open-channel and overland flows: Applications." *Journal of Hydraulic Engineering-Asce*, 133(8), 884-895.

Nikora, V. I., and Goring, D. G. (1998). "ADV measurements of turbulence: Can we improve their interpretation?" *Journal of Hydraulic Engineering-Asce*, 124(6), 630-634.

Nikora, V. I., Goring, D. G., and Biggs, B. J. F. (1998). "On gravel-bed roughness characterization." *Water Resources Research*, 34(3), 517-527.

Nikora, V. I., and Smart, G. M. (1997). "Turbulence characteristics of New Zealand gravel-bed rivers." *Journal of Hydraulic Engineering-Asce*, 123(9), 764-773.

Okamoto, T. A., and Nezu, I. (2009). "Turbulence structure and "Monami" phenomena in flexible vegetated open-channel flows." *Journal of Hydraulic Research*, 47(6), 798-810.

Olsen, N. R. B., and Stokseth, S. (1995). "Three-dimensional numerical modelling of water flow in a river with large bed roughness." *Journal of Hydraulic Research*, 33(4), 571 - 581.

Palmer, M. R., Nepf, H. M., Pettersson, T. J. R., and Ackerman, J. D. (2004). "Observations of particle capture on a cylindrical collector: Implications for particle accumulation and removal in aquatic systems." *Limnology and oceanography*, 49, 76-85.

Patel, V. C. (1998). "Perspective: Flow at high Reynolds number and over rough surfaces - Achilles heel of CFD." *Journal of Fluids Engineering-Transactions of the Asme*, 120(3), 434-444.

Pezzinga, G. (1994). "Velocity distribution in compound channel flows by numerical modeling." *Journal of Hydraulic Engineering-Asce*, 120(10), 1176-1198.

Phillips, N. A. (1957). "A coordinate system having some special advantages for

numerical forecasting." *Journal of Meteorology*, 14(2), 184-185.

Poggi, D., Katul, G. G., and Albertson, J. D. (2004a). "Momentum transfer and turbulent kinetic energy budgets within a dense model canopy." *Boundary-Layer Meteorology*, 111(3), 589-614.

Poggi, D., Porporato, A., Ridolfi, L., Albertson, J. D., and Katul, G. G. (2004b). "The effect of vegetation density on canopy sub-layer turbulence." *Boundary-Layer Meteorology*, 111(3), 565-587.

Pokrajac, D., Campbell, L. J., Nikora, V., Manes, C., and McEwan, I. (2007). "Quadrant analysis of persistent spatial velocity perturbations over square-bar roughness." *Experiments in Fluids*, 42(3), 413-423.

Precht, E., Janssen, F., and Huettel, M. (2006). "Near-bottom performance of the Acoustic Doppler Velocimeter (ADV) - a comparative study." *Aquatic Ecology*, 40(4), 481-492.

Rameshwaran, P., Naden, P. S., and Lawless, M. (2011). "Flow modelling in gravel-bed rivers: rethinking the bottom boundary condition." *Earth Surface Processes and Landforms*, 36(10), 1350-1366.

Rand, W. (1953). "Discussion of "Some effects of suspended sediment on flow characteristics"." *Proc. 5th Hydraulic Conf., Bulletin 34*, State University of Iowa, Iowa City IA.

Raupach, M. R., Antonia, R. A., and Rajagopalan, S. (1991). "Rough-wall turbulent boundary layers." *Applied Mechanics Reviews*, 44(1), 1-25.

Raupach, M. R., Finnigan, J. J., and Brunet, Y. (1996). "Coherent eddies and turbulence in vegetation canopies: The mixing-layer analogy." *Boundary-Layer Meteorology*, 78(3-4), 351-382.

Raupach, M. R., and Shaw, R. H. (1982). "Averaging procedures for flow within vegetation canopies." *Boundary-Layer Meteorology*, 22(1), 79-90.

Reynolds, A. J. (1974). *Turbulent flows in engineering*, Wiley & Sons.

Reynolds, O. (1895). "On the dynamical theory of incompressible viscous fluids and the determination of the criterion." *Philosophical Transactions of the Royal Society of London. A*, 186, 123-164.

Robert, A. (1990). "Boundary roughness in coarse-grained channels." *Progress in Physical Geography*, 14(1), 42-70.

Robert, A., Roy, A. G., and De Serres, B. (1993). "Space-time correlations of velocity measurements at a roughness transition in a gravel-bed river." In: *Turbulence: perspectives on flow and sediment transport*, N. J. Clifford, J. R. French, and J. Hardisty (eds.), Wiley, Chichester, 165-183.

Robert, A., Roy, A. G., and Deserres, B. (1992). "Changes in velocity profiles at roughness transitions in coarse-grained channels." *Sedimentology*, 39(5), 725-735.

Robert, A., Roy, A. G., and DeSerres, B. (1996). "Turbulence at a roughness transition in a depth limited flow over a gravel bed." *Geomorphology*, 16(2), 175-187.

Rodriguez, J. F., and Garcia, M. H. (2008). "Laboratory measurements of 3-D flow patterns and turbulence in straight open channel with rough bed." *Journal of Hydraulic Research*, 46(4), 454-465.

Rung, T., Bunge, U., Schatz, M., and Thiele, F. (2003). "Restatement of the Spalart-Allmaras eddy-viscosity model in strain-adaptive formulation." *Aiaa Journal*, 41(7), 1396-1399.

Shields, F., and Rigby, J. (2005). "River habitat quality from river velocities measured using acoustic doppler current profiler." *Environmental Management*, 36(4), 565-575.

Shimizu, Y., and Tsujimoto, T. (1944). "Numerical analysis of turbulent open-channel flow over a vegetation layer using a k-ε turbulence model." *Journal of hydrosciense and Hydraulic Engineering*, 11(2), 57-67.

Shimizu, Y., and Tsujimoto, T. (1994). "Numerical analysis of turbulent open-channel

flow over a vegetation layer using a k-ε turbulence model." *Journal of hydrosciense and Hydraulic Engineering*, 11(2), 57-67.

Smart, G. M. (1999). "Turbulent velocity profiles and boundary shear in gravel bed rivers." *Journal of Hydraulic Engineering-Asce*, 125(2), 106-116.

Smart, G. M., Duncan, M. J., and Walsh, J. M. (2002). "Relatively rough flow resistance equations." *Journal of Hydraulic Engineering-Asce*, 128(6), 568-578.

Souliotis, D., and Prinos, P. (2011). "Effect of a vegetation patch on turbulent channel flow." *Journal of Hydraulic Research*, 49(2), 157 - 167.

Spalart, P. R., and Allmaras, S. R. (1994). "A one-equation turbulence model for aerodynamic flows." *La Recherche Aerospatiale*, 1(1), 5-21.

Steffler, P. M., Rajaratnam, N., and Peterson, A. W. (1983). "*LDA measurements of mean velocity and turbulence distribution in a smooth rectangular open channel*." Water Resources Engineering, Report 83-4.

Stephan, U., and Gutknecht, D. (2002). "Hydraulic resistance of submerged flexible vegetation." *Journal of Hydrology*, 269(1-2), 27-43.

Sturm, T. W. (2010). *Open Channel Hydraulics*, McGraw-Hill, New York.

Su, X. H., and Li, C. W. (2002). "Large eddy simulation of free surface turbulent flow in partly vegetated open channels." *International Journal for Numerical Methods in Fluids*, 39(10), 919-937.

Takemura, T., and Tanaka, N. (2007). "Flow structures and drag characteristics of a colony-type emergent roughness model mounted on a flat plate in uniform flow." *Fluid Dynamics Research*, 39(9-10), 694-710.

Tsujimoto, T., Shimizu, Y., Kitamura, T., and Okada, T. (1992). "Turbulent open-channel flow over bed covered by rigid vegetation." *Journal of Hydrosciense and Hydraulic Engineering*, 10, 13-25.

Van der Vorst, H. A. (1992). "Bi-Cgstab - a Fast and Smoothly Converging Variant of Bi-Cg for the Solution of Nonsymmetric Linear-Systems." *Siam Journal on Scientific and Statistical Computing*, 13(2), 631-644.

Van der Vorst, H. A., and Sonneveld, P. (1990). "*CGSTAB, a more smoothly converging variant of CGS*." Technical Report 90-50.

Van Rijn, L. C. (1982). "Equivalent roughness of alluvial bed." *Journal of the Hydraulics Division-Asce*, 108(10), 1215-1218.

Voulgaris, G., and Trowbridge, J. H. (1998). "Evaluation of the acoustic Doppler velocimeter (ADV) for turbulence measurements." *Journal of Atmospheric and Oceanic Technology*, 15(1), 272-289.

Wang, J. J., Chen, C. Z., Dong, Z. N., and Xia, Z. H. (1993). "The effects of bed roughness on the distribution of turbulent intensities in open-channel flow." *Journal of Hydraulic Research*, 31(1), 89-98.

Wiberg, P. L., and Smith, J. D. (1991). "Velocity distribution and bed roughness in high-gradient streams." *Water Resources Research*, 27(5), 825-838.

Williams, P. T., and Baker, A. J. (1997). "Numerical simulations of laminar flow over a 3D backward-facing step." *International Journal for Numerical Methods in Fluids*, 24(11), 1159-1183.

Wilson, C., Stoesser, T., Bates, P. D., and Pinzen, A. B. (2003). "Open channel flow through different forms of submerged flexible vegetation." *Journal of Hydraulic Engineering-Asce*, 129(11), 847-853.

Wilson, C., Yagci, O., Rauch, H. P., and Olsen, N. R. B. (2006). "3D numerical modelling of a willow vegetated river/floodplain system." *Journal of Hydrology*, 327(1-2), 13-21.

Wu, F. C., Shen, H. W., and Chou, Y. J. (1999). "Variation of roughness coefficients for unsubmerged and submerged vegetation." *Journal of Hydraulic Engineering-Asce*, 125(9), 934-942.

Wu, W. M. (2004). "Depth-averaged two-dimensional numerical modeling of unsteady flow and nonuniform sediment transport in open channels." *Journal of Hydraulic Engineering-Asce*, 130(10), 1013-1024.

Yang, B., Morse, A., Shaw, R., and Paw U, K. (2006a). "Large-eddy Simulation of Turbulent Flow across a Forest Edge. Part II: Momentum and Turbulent Kinetic Energy Budgets." *Boundary-Layer Meteorology*, 121(3), 433-457.

Yang, B., Raupach, M., Shaw, R., U, K., and Morse, A. (2006b). "Large-eddy Simulation of Turbulent Flow Across a Forest Edge. Part I: Flow Statistics." *Boundary-Layer Meteorology*, 120(3), 377-412.

Yang, W., and Choi, S. U. (2009). "Impact of stem flexibility on mean flow and turbulence structure in depth-limited open channel flows with submerged vegetation." *Journal of Hydraulic Research*, 47(4), 445-454.

Yen, B. C. (1992). "Hydraulic resistance in open channels." In: *Channel flow resistance: centennial of Manning's formula*, B. C. Yen (eds.), Water Resources Publications, Highlands Ranch, Colorado, 1-135.

Zong, L., and Nepf, H. (2011). "Spatial distribution of deposition within a patch of vegetation." *Water Resource Research*, 47(3), W03516.